Conditional Moment Closure for spray combustion and ignition

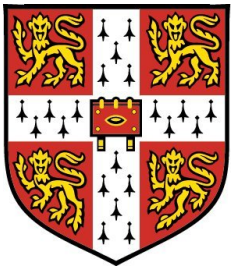

Peter Schroll

Queens' College

Department of Engineering University of Cambridge

A thesis submitted for the degree of

Doctor of Philosophy

21st December 2009

pour Patricia

Declaration

This dissertation is the result of my own work and includes nothing which is the outcome of work done in collaboration except where specifically indicated in the text. No part of this work has been submitted for any other degree or diploma.

Dipl. Ing. Peter Schroll

Cambridge, the 21st December 2009

The results of this thesis are partially covered in:

P. Schroll, A. P. Wandel, R. S. Cant and E. Mastorakos. Direct numerical simulations of autoignition in turbulent two-phase flows. Proceedings of the Combustion Institute, Volume 32, Issue 2, 2009, Pages $2275 - 2282$.

Schroll, P., Mastorakos, E. and Bilger, R. W. (2010). Simulations of spark ignition of a swirling n-heptane spray flame with Conditional Moment Closure. To be presented at the 48th AIAA Aerospace Sciences Meeting, $4 - 7$ January 2010, Orlando, Florida.

Acknowledgements

Foremost, I would like to express my sincere gratitude to my supervisor Dr. E. Mastorakos for his continuous support of my Ph.D study, for his patience, motivation and immense knowledge which helped me in all the time of research and writing of this thesis.

I wish to express my warm and sincere thanks to my advisor, Dr. R. S. Cant for his detailed and constructive comments, and for his important support throughout this work.

I am grateful to all members of Dr. E. Mastorakos' research team for the stimulating and encouraging working environment.

Abstract

In this thesis the development and implementation of the Conditional Moment Closure (CMC) model extended to two-phase flows is presented. For the extended CMC model additional source terms due to the droplet evaporation process in the conditional species and energy equation have to be taken into account. The droplet source terms in the mean and variance of the mixture fraction equation have also to be modelled. In addition three-dimensional direct numerical simulations (DNS) were carried out to investigate the impact of evaporation of droplets on the autoignition process under decaying turbulence, and findings were used for closure assumptions in the extended CMC model.

For the DNS study the focus was to examine the influence of the droplet evaporation process on the location of autoignition. It was found that an increase in the initial droplet size results in an increase in the autoignition time, that highest reaction rates always occur at a specific mixture fraction ξ_{MR}, as in purely gaseous flows, and that changes in the initial droplet size did not affect the value of ξ_{MR}. The conditional correlation coefficient between scalar dissipation rate and reaction rates was only mildly negative, contrary to the strongly negative values for purely gaseous autoigniting flows, possibly due to the continuous generation of mixture fraction by the droplet evaporation process that randomizes both the mixture fraction and the scalar dissipation fields.

Regarding the extended CMC model, first a zero dimensional version of the extended CMC model was validated against the DNS described above. The predictions of the CMC simulations for autoignition times compared

to DNS were in good agreement, showing that the extended CMC model and its closure assumptions are representing well the physics of droplet evaporation.The extended CMC model has been then interfaced with a commercial RANS two-phase flow solver to study the ignition process of an n-heptane spray flame in a flow typical of a liquid-fueled burner. For comparison, simulations without droplet source terms in the CMC equations were also carried out. The flame expansion process following ignition was compared qualitatively with fast-camera images from the experiment and the overall flame shape and speed are captured satisfactorily. Comparisons of conditional temperature at different locations in the flow field gives further insight on how the additional droplet evaporation source terms affect the flow field.

Contents

Nomenclature **xvii**

1 Introduction **1**
1.1 Challenge 1
1.2 Outline of this thesis 2

2 Reacting spray modelling **5**
2.1 Modelling and simulation tools for turbulent combustion 5
2.1.1 Governing equations 5
2.1.2 Direct Numerical Simulation 10
2.1.3 Reynolds Averaged Navier-Stokes 12
2.1.4 Large Eddy Simulations 13
2.1.5 Turbulent reacting flow modelling for RANS 13
2.2 Two-phase flow modelling 15
2.2.1 Physical description 16
2.2.2 Lagrangian approach 29

3 Conditional Moment Closure **33**
3.1 Chapter objective 33
3.2 Conditional Moment Closure 33
3.2.1 Conditional statistics 34
3.2.2 Conditional equations 35
3.2.3 Closure assumptions 37
3.3 Conditional Moment Closure for two-phase flows 39
3.3.1 CMC mass fraction equation 39

3.3.2 CMC energy equation 42
3.3.3 PDF of mixture fraction 46
3.3.4 Summary of closed governing equations 49

4 Direct Numerical Simulations of Autoignition in Turbulent Two-phase Flows 51
4.1 Objective 51
4.2 Spray autoignition 51
4.3 DNS of autoignition of droplets in hot surrounding 53
4.3.1 Setup 53
4.3.2 General evolution 55
4.3.3 Effect of initial droplet size 59
4.3.4 Locations of high $\langle\dot{\omega}|\eta\rangle$ 62
4.3.5 Influence of droplet evaporation on $P(\eta)$ 64
4.3.6 Conclusion 67
4.4 DNS of autoignition of cold saturated spray in hot surrounding 68
4.4.1 Setup 68
4.4.2 General evolution 68
4.4.3 Scatter plot of temperature and reaction rate 74
4.4.4 Conclusion 78

5 Validation of CMC for spray autoignition 80
5.1 Objectives 80
5.2 Numerical approach 80
5.3 Scalar dissipation model 82
5.4 Results 86
5.5 Conclusions 87

6 Simulations of spark ignition of a swirling spray flame with 2D-CMC 94
6.1 Background 94
6.2 CMC simulation setup 95
6.2.1 Flow configuration 95
6.2.2 Numerical approach 97
6.3 Cold flow solution 99
6.4 Spark ignition 105

6.5 Conclusions 125

7 Conclusions **126**

7.1 Direct Numerical Simulations of Autoignition in Turbulent Two-phase Flows 126

7.2 Autoignition of spray flow using 0D-CMC 127

7.3 Simulations of spark ignition of a swirling spray flame with CMC . . 128

7.4 Future work 128

List of Figures

2.1 Schematic of combustion regimes 6
2.2 Group combustion diagram (Chiu [1]) 17
2.3 Combustion regimes of a droplet spray (Chiu [1]) 18
2.4 Schematic of single evaporating droplet (left) and of single droplet combustion (right) in non-convective environment. 19
2.5 Schematic of liquid evaporating from container in to ambiance. 20
2.6 Surface change of evaporating droplet showing the preheating zone and the reduction of diameter following the D^2 law. 24
2.7 Temperature and species mass fraction profiles for single droplet combustion [2]. 26

4.1 Flow arrangement. 54
4.2 Volume averaged temperature against time. Inset shows autoignition times of homogeneous, adiabatic, stagnant mixtures as a function of mixture fraction with initial species mass fractions and temperature determined from inert mixing with $T_O = 0.5$ and $T_F = 0$, which is used to determine τ_{ref}. 56
4.3 Mixture fraction (1), temperature (2), scalar dissipation rate (3) and reaction rate (4) distribution of $CL1$ at $\tau/\tau_{ref} = 1.92$ (a), $\tau/\tau_{ref} = 2.24$ (b). In $(2.b)$ T is scaled by 2.2 and in $(4.b)$ ω by 50.7. The snapshot is at $z/L = 0.5$ and spans $0.3125 < x/L < 0.6250$ and $0.1560 < y/L < 0.4685$. 57
4.4 Scatter plots of temperature against mixture fraction for case $CL1$ at (a) $\tau/\tau_{ref} = 1.2$, (b) $\tau/\tau_{ref} = 1.6$, (c) $\tau/\tau_{ref} = 1.92$, and (d) $\tau/\tau_{ref} = 2.24$. [3] 58

4.5 Scatter plots of reaction rate against mixture fraction for case $CL1$ at (a) $\tau/\tau_{ref} = 1.2$, (b) $\tau/\tau_{ref} = 1.6$, (c) $\tau/\tau_{ref} = 1.92$, and (d) $\tau/\tau_{ref} = 2.24$. [3] 59
4.6 Mean evaporation rate (upper), scalar dissipation (middle) and mixture fraction (lower) at $\tau/\tau_{ref} = 1.6$. [3] 60
4.7 Conditionally-averaged evaporation rate $\langle m|\eta\rangle$, scalar dissipation rate $\langle N|\eta\rangle$ and temperature $\langle T|\eta\rangle$ at $\tau/\tau_{ref} = 1.6$. [3] 62
4.8 Conditional reaction rate $\langle\omega|\eta\rangle$ at $\tau/\tau_{ref} = 0.64$ (•), 1.6 (○) and 1.92 (△). [3] 63
4.9 Doubly-conditional reaction rate $\langle\omega|N,\eta\rangle$ of case $C01$ at $\tau/\tau_{ref} = 1.6$, where $N05$ implies $0 < N < 1$, $N15$: $1 < N < 2$, $N25$: $2 < N < 3$ and $N35$: $3 < N < 4$. [3] 64
4.10 Conditional correlation coefficient between ω and N against η for case $C01$ at $\tau/\tau_{ref} = 1.6$ (•), 1.92 (○) and 2.24 (△). 65
4.11 Probability density functions of mixture fraction for cases $C01$, $C02$ and $C03$ at $\tau/\tau_{ref} = 1.6$. 66
4.12 Probability density function of mixture fraction $P(\eta)$ for case $C01$ at $\tau/\tau_{ref} = 2.4$. 66
4.13 Averaged droplet surface mixture fraction ξ_{sat} conditional on cell mixture fraction η_{cell} for case $C01$ at $\tau/\tau_{ref} = 1.6$ (•), $\tau/\tau_{ref} = 2.24$ (○) and $\tau/\tau_{ref} = 2.4$ (△). 67
4.14 Temperature distribution of $SL1$ at six different time steps ((a) $\tau/\tau_{ref} = 1.92$, (b) $\tau/\tau_{ref} = 2.24$, (c) $\tau/\tau_{ref} = 2.56$, (d) $\tau/\tau_{ref} = 2.88$, (e) $\tau/\tau_{ref} = 3.20$, (f) $\tau/\tau_{ref} = 3.52$). 69
4.15 Mixture fraction distribution of $SL1$ at six different time steps. ((a) $\tau/\tau_{ref} = 1.92$, (b) $\tau/\tau_{ref} = 2.24$, (c) $\tau/\tau_{ref} = 2.56$, (d) $\tau/\tau_{ref} = 2.88$, (e) $\tau/\tau_{ref} = 3.20$, (f) $\tau/\tau_{ref} = 3.52$). 70
4.16 Reaction rates distribution of $SL1$ at six different time steps. ((a) $\tau/\tau_{ref} = 1.92$, (b) $\tau/\tau_{ref} = 2.24$, (c) $\tau/\tau_{ref} = 2.56$, (d) $\tau/\tau_{ref} = 2.88$, (e) $\tau/\tau_{ref} = 3.20$, (f) $\tau/\tau_{ref} = 3.52$). 71
4.17 Mean evaporation rate (left) and mixture fraction (right) at several τ/τ_{ref}. 72
4.18 Mean reaction rate (left) and scalar dissipation rate (right) at several τ/τ_{ref}. 73

4.19 Temperature distribution of $SL1$ at four different time steps after 4.14. ((g) $\tau/\tau_{ref} = 3.68$, (h) $\tau/\tau_{ref} = 3.84$, (i) $\tau/\tau_{ref} = 4.16$ and (j) $\tau/\tau_{ref} = 4.64$.) 73
4.20 Mixture fraction of $SL1$ at four different time steps after 4.14. ((g) $\tau/\tau_{ref} = 3.68$, (h) $\tau/\tau_{ref} = 3.84$, (i) $\tau/\tau_{ref} = 4.16$ and (j) $\tau/\tau_{ref} = 4.64$.) 74
4.21 Reaction rate of $SL1$ at four different time steps after 4.14. ((g) $\tau/\tau_{ref} = 3.68$, (h) $\tau/\tau_{ref} = 3.84$, (i) $\tau/\tau_{ref} = 4.16$ and (j) $\tau/\tau_{ref} = 4.64$.) 75
4.22 Scatter plots of temperature against mixture fraction for case $SL1$ at several τ/τ_{ref}. ((a) $\tau/\tau_{ref} = 0.64$, (b) $\tau/\tau_{ref} = 1.28$, (c) $\tau/\tau_{ref} = 1.92$, (d) $\tau/\tau_{ref} = 2.56$, (e) $\tau/\tau_{ref} = 3.20$, (f) $\tau/\tau_{ref} = 4.64$.) 76
4.23 Scatter plots of reaction rate against mixture fraction for case $SL1$ at several τ/τ_{ref}. ((a) $\tau/\tau_{ref} = 0.64$, (b) $\tau/\tau_{ref} = 1.28$, (c) $\tau/\tau_{ref} = 1.92$, (d) $\tau/\tau_{ref} = 2.56$, (e) $\tau/\tau_{ref} = 3.20$, (f) $\tau/\tau_{ref} = 4.64$.) 77
4.24 Mean conditional temperature (above) and conditional reaction rate (below) for case $SL1$ and $SL2$ at (a) $\tau/\tau_{ref} = 1.92$ and (b) $\tau/\tau_{ref} = 2.56$) 78
4.25 Reaction rate over mixture fraction and scalar dissipation at $\tau/\tau_{ref} = 1.28$ (above) and $\tau/\tau_{ref} = 1.92$ (below). The color code of the graphs does not have a specific meaning but is intended to help visualization. 79

5.1 Setup for 0D-CMC code using DNS data at certain time steps 81
5.2 ξ_i-shell for ξ_i determined by r_1 and r_2. 83
5.3 Top: Scalar dissipation rate N and fuel mass fraction Y_f vs radial distance to droplet r ($r_s/r_{Cell} = 0.05$). Below: Radial distance from droplet r and scalar dissipation rate N vs mixture fraction ξ. $\xi_S = 0.3$ and $\xi_{Cell} = 0.005$. 85
5.4 Top: Scatter plots of scalar dissipation rate in mixture fraction space taken at $\tau/\tau_{ref} = 0.64$. Red points denote DNS grid cells and black points are established from the scalar dissipation model for each droplet. Below: Same data on a logarithmic y-scale. 88

5.5 Top: $\langle N|\eta\rangle$ for DNS grid cells (solid line) and for combination of DNS grids cells and subgrid model cells (dashed line), weighted by factor F of Eq. (5.15) at $\tau/\tau_{ref} = 0.64$. Below: $\langle N|\eta\rangle$ for different time steps of case $C01$. 89
5.6 $\langle\omega|\eta_{MR}\rangle$ vs. time for case $C01$ and $C02$. 89
5.7 $\langle\omega|\eta_{ST}\rangle$ vs. time for case $C01$ and $C02$. 90
5.8 Comparison of reaction rate conditional on mixture fraction $\langle\omega|\eta\rangle$ vs τ/τ_{ref} for case $C02$. Red line denotes the zero dimensional CMC model extended to two-phase flow. Black dotted line denotes the DNS solution. 91
5.9 Comparison of oxidizer mass fraction conditional on mixture fraction $\langle Y_{O2}|\eta\rangle$ vs τ/τ_{ref} for case $C02$. Red line denotes the zero dimensional CMC model extended to two-phase flow. Black dotted line denotes the DNS solution. 92
5.10 Comparison of temperature conditional on mixture fraction $\langle T|\eta\rangle$ vs τ/τ_{ref} for case $C02$. Red line denotes the zero dimensional CMC model extended to two-phase flow. Black dotted line denotes the DNS solution. 93

6.1 Schematic of bluff body burner configuration, including the inner (1) and outer (2) recirculation zones marked by arrows. 95
6.2 Schematic of burner from [4] (left) and block structured axi-symmetric grid (right). 96
6.3 Schematic of the STAR-CD CMC coupling and the droplet evaporation subroutine. The grey underlaid area highlights the FORTRAN subroutines used in the coupling. 98
6.4 Conditional temperature (left) and mass fraction (right) profiles for different N_0 from use of the 1-step n-heptane mechanism [5]. 100
6.5 Contour plot of axial (right) and swirl (left) mean velocity of the cold flow in absence of spray. 101
6.6 Predicted and measured radial profile of mean swirl (top) and axial (bottom) velocity for air flow in absence of spray at the indicated axial positions. Experimental data from Ref. [4]. 102

6.7 Comparison of the experimental (left) and simulation (right) droplet distribution within the cold spray flow. 103
6.8 Contour plot of axial mean velocity of the cold spray flow. 103
6.9 Contour plot of mean temperature for cold spray flow before spark ignition. 104
6.10 Temperature profiles conditional on mixture fraction for different axial and radial locations of the cold spray flow. 104
6.11 Distribution of the Droplet Sauter Mean Diameter (SMD) at different axial distances downstream of the bluff body. 105
6.12 Contour plot of mean mixture fraction (left) and variance of mixture fraction (right) of cold spray flow. The white line in the mean mixture fraction contour plot denotes the stoichiometric line for heptane. . . . 106
6.13 Comparison between contour plots of temperature for case A and high-speed images [4] at different time steps. Initial spark kernel location at $r = 0mm$ and $z = 23mm$ and image domain $70x50$mm. 107
6.14 Contour plots of temperature for case A after spark ignition. Initial spark kernel location at $r = 0mm$ and $z = 23mm$ and image domain $70x50$mm. (a) at $t = 0.3$ms, (b) at $t = 0.7$ms, (c) at $t = 1.9$ms, (d) at $t = 7.1$ms, (e) at $t = 13.5$ms and (f) at $t = 16.5$ms. 108
6.15 Contour plots of mean axial velocity for case A after spark ignition. Initial spark kernel location at $r = 0mm$ and $z = 23mm$ and image domain $70x50$mm. (a) at $t = 0.3$ms, (b) at $t = 0.7$ms, (c) at $t = 1.9$ms, (d) at $t = 7.1$ms, (e) at $t = 13.5$ms and (f) at $t = 16.5$ms. 109
6.16 Contour plots of mean mixture fraction for case A after spark ignition. Initial spark kernel location at $r = 0mm$ and $z = 23mm$ and image domain $70x50$mm. White lines denote the stoichiometric mixture fraction ξ_{St}. (a) at $t = 0.3$ms, (b) at $t = 0.7$ms, (c) at $t = 1.9$ms, (d) at $t = 7.1$ms, (e) at $t = 13.5$ms and (f) at $t = 16.5$ms. 110
6.17 Contour plots of variance of mixture fraction for case A after spark ignition. Initial spark kernel location at $r = 0mm$ and $z = 23mm$ and image domain $70x50$mm. (a) at $t = 0.3$ms, (b) at $t = 0.7$ms, (c) at $t = 1.9$ms, (d) at $t = 7.1$ms, (e) at $t = 13.5$ms and (f) at $t = 16.5$ms. . 111

6.18 Upper: Contour plots of temperature difference $\Delta\widetilde{T}$ between case A ($\widetilde{T}_a$) with and case B ($\widetilde{T}_b$) without extra droplet source terms in the CMC equations. Lower: Contour plots of mean mixture fraction difference $\Delta\widetilde{\xi}$ between case A ($\widetilde{\xi}_a$) with and case B ($\widetilde{\xi}_b$) without extra droplet source terms in the CMC equations. For both $\Delta\widetilde{T}$ and $\Delta\widetilde{\xi}$ contour plots are shown at $t = 0.238$ms and $t = 7.4$ms. 113
6.19 Upper: Contour plots of temperature difference $\Delta\widetilde{T}$ between case A ($\widetilde{T}_a$) with and case B ($\widetilde{T}_b$) without extra droplet source terms in the CMC equations. Lower: Contour plots of mean mixture fraction difference $\Delta\widetilde{\xi}$ between case A ($\widetilde{\xi}_a$) with and case B ($\widetilde{\xi}_b$) without extra droplet source terms in the CMC equations. For both $\Delta\widetilde{T}$ and $\Delta\widetilde{\xi}$ contour plots are shown at $t = 13.8$ms and $t = 15.9$ms. 114
6.20 Mean temperature contour plot of case A, at t=13.5ms. Marked positions are used to show conditional averages in Figs. 6.21, 6.22 and 6.23. 115
6.21 $\langle T|\eta\rangle$ for case A (red dotted) and B (black) at different locations for $t = 0.238ms$. 116
6.22 $\langle T|\eta\rangle$ for case A (red dotted) and B (black) at different locations for $t = 7.4ms$. 117
6.23 $\langle T|\eta\rangle$ for case A (red dotted) and B (black) at different locations for $t = 13.8ms$. 118
6.24 $\langle Y_{O_2}|\eta\rangle$ for case A (red dotted) and B (black) at different locations for $t = 7.4ms$. 119
6.25 $\langle Y_{O_2}|\eta\rangle$ for case A (red dotted) and B (black) at different locations for $t = 13.8ms$. 120
6.26 Contour plots of temperature for case C. The white line in the mean mixture fraction contour plot denotes the stoichiometric line for heptane. 121
6.27 Above: Contour plots of temperature difference ΔT between case C (T_a) with and case D (T_b) without extra droplet source terms in the CMC equations. Below: Contour plots of mean mixture fraction difference $\Delta\widetilde{\xi}$ between case C ($\widetilde{\xi}_a$) with and case D ($\widetilde{\xi}_b$) without extra droplet source terms in the CMC equations. 122

6.28 $\langle T|\eta\rangle$ for case C(red dotted) and D (black) at two different locations near the core spray for four different times after spark ignition. Location 1 is at $r = 11.8mm$ and $z = 18.7m$, location 2 at $r = 5.7mm$ and $z = 25.4mm$. 123
6.29 $\langle T|\eta\rangle$ for case C(red dotted) and D (black) at two different locations near the core spray for four different times after spark ignition. Location 3 is at $r = 8.8mm$ and $z = 40.4m$, location 4 at $r = 21.5mm$ and $z = 49.3mm$. 124

List of Tables

4.1 List of parameters for the DNS. Θ_0 is the initial droplet diameter, τ_{ign} the autoignition time, τ_{turb} the large-eddy turbulent time scale, τ_{ref} the minimum autoignition time for the reference case (Fig.4.2). n is the total number of droplets per unit volume, Re_t is the turbulent Reynolds number and η_K is the non-dimesionalized Kolmogorov length scale. St is the Stokes number calculated by $St = \tau_d/\tau_K$, where $\tau_K = (\nu/\epsilon)^{1/2}$ is the Kolmogorov time scale. For the evaporation time τ_{vap} without combustion, droplets are assumed to be completely evaporated when $\Theta = 0.1\Theta_0$. 55

6.1 Table of cases. 97

Chapter 1

Introduction

1.1 Challenge

Combustion may be one of the first techniques of mankind going along with the invention of the wheel and stone tools. During human evolution the use of combustion in many different ways was the driving force for cultural development leading to a highly technological civilization we see it today. It is not combustion itself which makes it so valuable but its emitting heat which can be converted into other forms of energy. The supply of energy alongside with water and air form the basic needs the civilization is demanding. To provide the energy demanded for domestic heating, power generation or transportation, fossil fuels remain today the main source [6]. Combustion of fossil fuels has not only the power of supplying us with energy but also the power to destroy our natural environment. The production of pollutants as a side product of fossil fuel combustion such as oxides of nitrogen (NO_x), unburnt hydrocarbons (UHC) and soot are causing damage to human health and nature. In addition, even for highly developed combustion systems producing minimum of such pollutants, still unavoidable emissions of CO_2 are created which is believed to be the major contributor to global warming. This leads to the challenge for scientists and engineers today to find a way how to provide the energy demanded while keeping its impact on our environment low.

There could be different ways to solve this problem. On the customer side the energy demand has to be reduced both by increasing the social awareness of the high value of energy and by installing low energy consuming devices. The other way is

to review the way energy is produced. Alternative energy sources such as wind and solar power or nuclear energy have a high potential to substitute the amount of fossil fuel combustion, but for the foreseeable future these energy sources can't be used efficiently enough with today's technology. So industry has to improve combustion devices for fossil fuel in the short term regarding efficiency and emissions, implying the need for a fundamental understanding and mathematical description of all aspects of combustion. This is a quite challenging field, keeping a wide range of scientists busy for more than half a century now [7]. Especially the interaction between turbulence and chemical reaction is of interest since most industrial devices are used under these conditions [8]. With liquid fuel combustion enhancing the complexity, a fascinating and demanding field of tasks is lying in front of the combustion research society.

The use of computational resources over the last couple of decades established a new method to understand combustion. Computational Fluid Dynamics (CFD) developed to a powerful tool in combustion research offering high predictive capabilities and also the chance to get theoretical insight into various aspects of reactive flows. Of course, this tool is limited on one side by the completeness of its physical model and on the other side by its computational demand. Predictive CFD tools for industrial applications like gas turbines or furnaces are still limited [9]. Especially the use of Direct Numerical Simulation (DNS) is restricted to academic use. This implies the need for more powerful computer clusters but also the need for advanced physical models allowing to deal with more complex combustion systems. Incorporations of such advanced physical models for turbulence (Reynolds Average Navier Stokes (RANS), Large Eddy Simulations (LES)) and chemistry (such as PDF, Flamelet and Conditional Moment Closure (CMC)) are showing very encouraging results.

1.2 Outline of this thesis

In this thesis a first order Conditional Moment Closure (CMC) model is developed, which is extended to two-phase flow problems. To support the detailed investigation of the interactions between droplet evaporation, mixing and autoignition, three-dimensional DNS of autoignition in turbulent two-phase flows is carried out to. This

DNS data is used for validation purposes of the proposed CMC model extended to two phase flows. To concentrate better on the validation of the extra droplet source terms, a spatially homogeneous CMC problem is taken which reduced the complexity of the governing CMC equations. The extended CMC model is then interfaced with a commercial RANS two-phase flow solver to study the ignition process of an n-heptane spray flame in a flow typical of a liquid-fueled burner. The aim is to investigate the influence of the additional source terms due to the droplet evaporation process in the conditional species and energy equation.

Chapter 2 gives the reader a basic understanding of the theory involved in reacting spray modelling. Modelling and simulation tools for turbulent combustion and an introduction into two-phase flow modelling is given.

Chapter 3 the Conditional Moment Closure (CMC) equations and closures are presented, including the extended equations for two-phase modelling which will be implemented later in Chapter 5 and 6. As for the derivation of the single phase CMC equations, the decomposition method by Bilger [10] is used for the derivation of the two-phase flow extended CMC equations. For both temperature and mass fraction CMC equations additional source terms appear due to the droplet evaporation process. For the presumed PDF approach the equation for the mean and variance of mixture fraction for two-phase flows is presented using the closure model by Demoulin and Borghi [11] for the closure of the droplet source terms in the mixture fraction variance equation.

Chapter 4 three-dimensional direct numerical simulations (DNS) is carried out for validation purposes of the CMC model for two-phase flows presented in Chapter 3. These calculations offer the possibility to investigate further autoignition under the presence of droplet vaporization. Of interest are the impact of evaporation of droplets on the autoignition process under decaying turbulence. The droplets are taken as point sources and are tracked in a Lagrangian manner. The focus is to examine the influence of the droplet evaporation process on the location of autoignition. Of interest is if an increase in the initial droplet size influences the autoignition time. In addition it will

be investigated if a specific mixture fraction ξ_{MR} can be found where the highest reaction rates always occur, as in purely gaseous flows [12]. The data will provide needed information for the validation of the CMC model presented in Chapter 3.

Chapter 5 zero dimensional CMC simulations are carried out based on DNS case $C01$ and $C02$ (Table 6.1) from Chapter 4. This is done for validating the established CMC equations extended to two-phase flows, as presented in Chapter 3. The advantage of using zero dimensional CMC for validation is that it simplifies both the conditional mass fraction and temperature equation while still keeping all source terms due to droplet evaporation. This makes the zero dimensional version of CMC a perfect starting point for validating the extended CMC model for two-phase flows.

Chapter 6 the CMC model extended to two-phase flow is applied to ignition of a swirling bluff body stabilized n-heptane spray fuelled flame. The predictions of the cold spray flow solution and of the spray flame are compared to experimental data [4]. Comparison of simulations of the CMC model, with and without extension to two-phase flow, for the flame establishment after spark ignition is carried out to examine the differences between the conventional model and the new one. The model presented and partly validated here can be used in a great variety of turbulent spray combustion applications. However, many aspects need further development and these are discussed in Chapter 7.

Chapter 2

Reacting spray modelling

2.1 Modelling and simulation tools for turbulent combustion

In combustion processes fuel and oxidizer are mixed and burned. To achieve this, different methods can be followed. Either mixing occurs first and then burning (premixed) or mixing and burning occurs at the same time (non-premixed). Both processes can further be subdivided in laminar or turbulent flow conditions. This can be seen in Figure 2.1. For most industrial applications combustion in turbulent flow is inevitable. Turbulent premixed flame examples are spark ignited internal combustion and stationary gas turbine engines while turbulent non-premixed combustion can be found in diesel and jet engines. The obvious advantages of turbulence for combustion is the enhanced mixing effect. Mixing increases the reaction rate and thus allows to release more heat. In simple terms, turbulence allows engineers to get more power out of a specific combustion volume compared to a laminar case. In this chapter, spray evaporation and combustion models are discussed.

2.1.1 Governing equations

The basic set of instantaneous balance equations consists of the continuity and momentum (Navier-Stokes), energy and species transport equation. For non-premixed flames

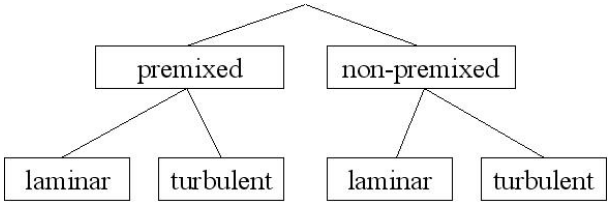

Figure 2.1: Schematic of combustion regimes

the balance equation for mixture fraction is introduced. The equations presented in the following discussion can be found in [13],[2], [14] and [15]. They are essential for the understanding of the CMC modeling method.

Continuity Equation: The continuity equation can be written as

$$\frac{\partial \rho}{\partial t} + \frac{\partial \rho u_j}{\partial x_j} = 0 \tag{2.1}$$

For constant density:

$$\frac{\partial u_j}{\partial x_j} = 0 \tag{2.2}$$

Momentum Equation: The momentum equation in conservative form is

$$\frac{\partial \rho u_i}{\partial t} + \frac{\partial \rho u_j u_i}{\partial x_j} = -\frac{\partial p}{\partial x_i} + \frac{\partial \tau_{ij}}{\partial x_j} + F_i \tag{2.3}$$

The two terms on the left-hand side in Eq. (2.3) represent the local rate of change and the convection of momentum, respectively. On the right hand side the terms, from left to right, represent the pressure gradient, the molecular transport due to viscosity, and the effect of external forces. In practical situations, most fluids are assumed to be Newtonian so that the viscous tensor τ_{ij} is given by the Newton law

$$\tau_{ij} = \mu \left(\frac{\partial u_i}{\partial x_j} + \frac{\partial u_j}{\partial x_i} \right) - \frac{2}{3} \mu \delta_{ij} \left(\frac{\partial u_k}{\partial x_k} \right) \tag{2.4}$$

where the first term on the right hand side comprises the symmetric rate of strain tensor S_{ij}.

Energy Equation: The energy equation can be written in terms of enthalpy or temperature. Starting from the first law of thermodynamics a balance equation for the enthalpy can be derived as

$$\frac{\partial \rho h}{\partial t} + \frac{\partial \rho u_j h}{\partial x_j} = \frac{\partial p}{\partial t} + \frac{\partial u_j p}{\partial x_j} - \frac{\partial J_j^h}{\partial x_j} + \frac{\partial u_i \tau_{ij}}{\partial x_j} + q_R, \tag{2.5}$$

where h is the mass-weighted sum of the specific enthalpy, h_α, of species α. This is given for an ideal gas by

$$h_\alpha = h_{\alpha,ref} + \int_{T_{ref}}^{T} c_{p\alpha}(T) dT \tag{2.6}$$

where $c_{p\alpha}$ is the specific heat capacity of species α at constant pressure. In Eq. (2.5) $u_i \tau_{ij}$ denotes the power due to viscous forces and q_R represents the heat transfer due to radiation. The enthalpy diffusion in the third term on the r.h.s. is described according to the Fourier law [2]

$$J_j^h = -\frac{\mu_l}{Pr} \left[\frac{\partial h}{\partial x_j} + \sum_{\alpha=1}^{N} \left(\frac{Pr}{Sc_\alpha} - 1 \right) h_\alpha \frac{\partial Y_\alpha}{\partial x_j} \right] \tag{2.7}$$

with Pr and Sc_α as the Prandtl and Schmidt number, respectively. The static pressure can be obtained from the thermal equation of state for an ideal gas

$$p = \rho \frac{RT}{W} \tag{2.8}$$

where R is the universal gas constant and W is the mean molecular mass:

$$W = \left(\sum_{\alpha=1}^{n} \frac{Y_\alpha}{W_\alpha} \right)^{-1} \tag{2.9}$$

Another form of the energy equation can be derived in terms of temperature

$$\rho c_p \frac{\partial T}{\partial t} + \rho c_p u_j \frac{\partial T}{\partial x_j} = \frac{\partial p}{\partial t} + \frac{\partial}{\partial x_j}\left(\lambda \frac{\partial T}{\partial x_j}\right) - \sum_{\alpha=1}^{N} c_{p\alpha} J_j^\alpha \frac{\partial T}{\partial x_j} - \sum_{\alpha=1}^{N} h_\alpha \dot{\omega}_\alpha + q_R \quad (2.10)$$

where λ is the thermal diffusivity and J_j^α is the molecular diffusive flux of species α.

Species Equation: For N species ($\alpha = 1, ..., N$), the mass fraction balance equation for species α is

$$\frac{\partial \rho Y_\alpha}{\partial t} + \frac{\partial \rho u_j Y_\alpha}{\partial x_j} = -\frac{\partial J_j^\alpha}{\partial x_j} + \dot{\omega}_\alpha \quad (2.11)$$

where J_j^α is the molecular diffusive flux of species α and $\dot{\omega}_\alpha$ represents the mass reaction rate of species α per unit volume. As stated in [6] the molecular transport processes causing the diffusive fluxes are quite complex. Since in most models of turbulent combustion molecular transport is small compared to the turbulent transport, simple model for J_j^α are usually of sufficient accuracy. Species diffusion under temperature gradients (Soret effect) and molecular transport due to pressure gradients are usually neglected. The most elementary is the binary flux approximation based on Fick's law [2]

$$J_j^\alpha = -\rho D_\alpha \frac{\partial Y_\alpha}{\partial x_j} \quad (2.12)$$

where D_α is the molecular diffusivity of species α. This assumption for J_j^α can cause problems with the conservation of mass in a multicomponent system since a wide range of different D_α are present so that the sum of all N fluxes doesn't vanish. In this thesis we will assume D_α to be the same for all species.

Reaction rate: The reaction rate $\dot{\omega}_\alpha$ is the result of chemical reactions taking place where species α is involved. Considering a reaction system of R reactions for N species, the k-th reaction is represented by

$$\sum_{\alpha=1}^{N} \nu'_{\alpha k} M_\alpha \underset{k_{rk}}{\overset{k_{fk}}{\rightleftharpoons}} \sum_{\alpha=1}^{N} \nu''_{\alpha k} M_\alpha \quad (2.13)$$

where M_α is the chemical symbol for species α. Here $\nu'_{\alpha k}$ and $\nu''_{\alpha k}$ are the stoichiometric coefficients for species α appearing as reactant or product, respectively. k_{fk} and k_{rk} are the "forward" and "backward" reaction rate constants, respectively. The chemical source term for the αth species can be written as the sum over all reaction

$$\dot{\omega}_\alpha = W_\alpha \sum_{k=1}^{R} (\nu''_{\alpha k} - \nu'_{\alpha k}) \dot{\omega}_k \tag{2.14}$$

where

$$\dot{\omega}_k = k_{fk} \prod_{\alpha=1}^{N} \left(\frac{\rho Y_\alpha}{W_\alpha} \right)^{\nu'_{\alpha k}} - k_{bk} \prod_{\alpha=1}^{N} \left(\frac{\rho Y_\alpha}{W_\alpha} \right)^{\nu''_{\alpha k}} \tag{2.15}$$

is the rate of reaction k. As stated in [16], Eq. (2.15) is based on the law of mass action which states that the reaction rate of a chemical product species is proportional to the products of the concentrations of the reacting chemical species, each concentration being raised to a power equal to the corresponding stoichiometric coefficient. The reaction rate constants k_f and k_b are independent of the concentration but depend on temperature. This dependance can be expressed by the Arrhenius equation

$$k = A' T^b exp \left(\frac{-E_a}{RT} \right) \tag{2.16}$$

where A', b and E_a are empirical parameters. AT^b represents the collision frequency while the exponential term is referred to as the Boltzmann factor which specifies the collision fraction exceeding the activation energy E_a. A simplified reaction is used in this thesis with an one-step chemical reaction in form of

$$Fuel + sOxidizer \rightarrow (1+s) Products \tag{2.17}$$

The use of Eq. (2.17) can be justified since for the DNS analysis in Chapter 4 autoignition is investigated with surrounding air of high temperature. This implies that the chemistry behaves in an Arrhenius way and hence the advantages of implementing a detailed scheme (for example, capturing the possibility of negative dependence of ignition time on temperature) are probably not affecting the autoignition process and how it interacts with the turbulence. For revealing these interactions, a one-step model may be sufficient, an approach also followed in Ref. [17].

Mixture Fraction Equation: To describe the internal structure of diffusion flames (non-premixed) usually the extent of mixing between fuel and oxidizer is used. Therefore a conserved scalar (a Shvab-Zeldovich variable) is introduced, combining the mass fraction of fuel and oxidizer

$$\theta(Y_F, Y_O) = Y_F - \frac{Y_O}{s} \tag{2.18}$$

where s is the mass stoichiometric coefficient given by

$$s = \frac{\nu_O W_O}{\nu_F W_F} \tag{2.19}$$

Normalizing ϕ using the values $Y_{O,0}$ and $Y_{F,0}$ in the fuel and oxidizer stream, respectively, the mixture fraction ξ can be defined as

$$\xi = \frac{\phi \frac{Y_F}{Y_{F,0}} - \frac{Y_O}{Y_{O,0}} + 1}{\phi + 1} \tag{2.20}$$

where ϕ is the equivalence ratio given by

$$\phi = \frac{s Y_{F,0}}{Y_{O,0}} \tag{2.21}$$

where ξ can be seen as the fraction of mass originating from the fuel stream compared to the total mass of the mixture. So ξ is unity in the fuel stream and zero in the oxidizer stream. A transport equation for ξ can be derived by combining the species transport Eq. (2.11) for Y_F and Y_O.

$$\frac{\partial \rho \xi}{\partial t} + \frac{\partial \rho u_j \xi}{\partial x_j} = \frac{\partial}{\partial x_j}\left(\rho D_\xi \frac{\partial \xi}{\partial x_j}\right) \tag{2.22}$$

where D_ξ is mean diffusivity of the mixture [10].

2.1.2 Direct Numerical Simulation

Direct Numerical Simulation (DNS) is seen as the most accurate computational tool for simulating turbulent combustion. Its major advantage is that no averaging or filtering procedures are used for solving the Navier-Stokes and species conservation equations,

and so no turbulence model is needed. This allows to fully resolve for the stochastic nature of turbulence with its whole range of spatial and temporal scales.

But DNS applications are limited since the complete resolution of all spatial and temporal scales of turbulence, in combination with a detailed chemistry description, puts a high demand on computational requirements. A complete three dimensional DNS with complex chemistry, multi species transport and realistic thermodynamics is still numerically not feasible [14]. This leads to restrictions of the flow field geometry and conditions, making it less attractive and too expensive for practical engineering problems. An increase in computational power in the future will loosen this restriction. But simplifications on geometry, chemistry and the turbulent structure, leading to great reduction of computational time, showed already useful and meaningful results. At present simplified DNS is used to a great extend for fundamental studies to develop a deeper insight into physical phenomena of turbulent combustion, where other computational tools or experimental work are limited in their resolution.

Over the last decades DNS was used with various simplifications depending on the application problem. The majority of DNS is either limited to two spatial dimensions with detailed chemistry [18; 19; 20; 21] or three dimensions in space with simplified chemistry [22; 23; 24; 25; 26; 27] for gaseous fuels. While the use of simplified chemistry does not account correctly for flammability issues, two-dimensional turbulence does not reflect all phenomena found in three-dimensional turbulence.

To account for spray flows, DNS was extended to two-phase flows to study droplet evaporation effects on the gaseous phase [28; 29; 30; 31; 32], using the common approach to consider the droplets as point sources of mass, energy and momentum. For reactive two-phase flows, the first work is due to Mashayek [33; 34]. Later a two-dimensional study was performed to study the effect of temperature and equivalence ratio on the ignition of a fuel spray in isotropic decaying turbulence with a detailed reaction mechanism [35], while a similar study in 2-D with one-step chemistry [17] focused on the droplet evaporation and its effects on the mixture fraction. The autoignition of droplet-laden transitional jets was also examined [36] where it was found that evaporative cooling and turbulence mixing play important roles in the ignition of

liquid-fuel spray jets. Such DNS, but three-dimensional, are described in Chapter 4 and used to validate a CMC model in Chapter 5.

2.1.3 Reynolds Averaged Navier-Stokes

Since DNS is limited to simple geometries [14], an additional step is introduced by averaging the balance equations to describe only the mean flow field. This is called the Reynolds Averaged Navier-Stokes (RANS) approach. The advantage is that local fluctuations and turbulent structures are integrated in mean quantities, reducing the complexity of the flow. Each quantity Q is represented by

$$Q = \overline{Q} + Q' \tag{2.23}$$

where $\overline{Q}$ and Q' are the mean and the fluctuation of Q, respectively. Averaging the fluctuation results in $\overline{Q'} = 0$. Using this averaging technique to derive the averaged transport equations brings unclosed correlations that are unknown and must be modeled.

In turbulent combustion, fluctuations of density occur due to thermal heat release. In this case, a mass weighted averaging approach (Favre averaging) is more suitable because of strong density fluctuation. Any quantity Q is then decomposed into

$$Q = \widetilde{Q} + Q'' \tag{2.24}$$

where $\widetilde{Q}$ is given by

$$\widetilde{Q} = \frac{\overline{\rho Q}}{\bar{\rho}} \tag{2.25}$$

Favre averaging of equations (2.1),(2.3),(2.5) and (2.11) leads to

$$\frac{\partial \bar{\rho}}{\partial t} + \frac{\partial \bar{\rho}\tilde{u}_j}{\partial x_j} = 0 \tag{2.26}$$

$$\frac{\partial \bar{\rho}\tilde{u}_i}{\partial t} + \frac{\partial \bar{\rho}\tilde{u}_j\tilde{u}_i}{\partial x_j} + \frac{\partial \bar{\rho}\widetilde{u_i'' u_j''}}{\partial x_j} = -\frac{\partial \bar{p}}{\partial x_i} + \frac{\partial \overline{\tau}_{ij}}{\partial x_j} + \bar{F}_i \tag{2.27}$$

$$\frac{\partial \bar{\rho}\tilde{h}}{\partial t} + \frac{\partial \bar{\rho}\tilde{u}_j\tilde{h}}{\partial x_j} + \frac{\partial \bar{\rho}\widetilde{u_j''h''}}{\partial x_j} = \frac{\partial \bar{p}}{\partial t} + \frac{\partial}{\partial x_j}\left(\overline{J_j^h} + \overline{u_i\tau_{ij}}\right) + \overline{u_jF_j} \tag{2.28}$$

$$\frac{\partial \bar{\rho}\tilde{Y}_k}{\partial t} + \frac{\partial \bar{\rho}\tilde{u}_j\tilde{Y}_k}{\partial x_j} + \frac{\partial \bar{\rho}\widetilde{u_j''Y_k''}}{\partial x_j} = -\frac{\partial \overline{J_j^i}}{\partial x_j} + \overline{\dot{\omega}_i} \tag{2.29}$$

The Reynolds stresses $\widetilde{u_i''u_j''}$, in Eq. (2.28) the enthalpy fluxes $\bar{\rho}\widetilde{u_j''h''}$ and in Eq. (2.29) the species fluxes $\bar{\rho}\widetilde{u_j''Y_k''}$ are unknown quantities and have to be modelled. Also, the diffusion fluxes $\overline{J_j^k}$, $\overline{J_j^h}$ and the averaged chemical reaction rate $\overline{\dot{\omega}_k}$ have to be modeled.

2.1.4 Large Eddy Simulations

Large Eddy Simulation (LES) has its origins in meteorological calculations and predictions [37]. The basic idea of LES is to directly simulate the large scales of turbulence while the small scales are modeled. This is based on the energy-cascade hypothesis. The larger and more unstable eddies are breaking down to smaller scales, transferring energy to the smallest eddies, which dissipate their kinetic energy through molecular viscosity [15].

For purely gaseous flows, the CMC model has been incorporated with LES recently and shown promising results [38; 39; 40]. Adapting the CMC model extended to spray flows presented here is an interesting field for future work.

2.1.5 Turbulent reacting flow modelling for RANS

For certain reacting flow problems using solely a function of the local mean temperature and composition, as shown above, to represent the averaged (RANS) reaction rate is not accurate enough [6]. The non-linear form of the expression of the chemical source term in Eq. 2.11 implies that fluctuations in time and space for temperature and concentrations will lead to large errors, if their averages are used. Therefore more sophisticated models are needed. For non-premixed combustion there are two main model groups: infinitely fast chemistry and finite-rate chemistry models, and their choice depends on the Damköhler number Da. The Damköhler number defines the

ratio between the turbulent mixing time scale and the chemical reaction time scale.

For cases with relatively fast chemistry the **Eddy-Break Up (EBU)** model is feasible. The concept is based on the idea that chemical rates are much faster than the mixing by either molecular diffusion [41] or turbulence [42], so only the mixing process is the controlling parameter of combustion. For the EBU model the mean chemical reaction rate of products can be expressed as

$$\overline{\dot{\omega}_p} = \overline{\rho} C_{EBU} \frac{\tilde{\epsilon}}{\tilde{k}} \left(\overline{Y_p''^2} \right)^{1/2} \tag{2.30}$$

where $\overline{Y_p''^2}$ is the variance of the product mass fraction and C_{EBU} the Eddy-Break Up constant. The main idea of this model is to replace the chemical time scale by the turbulent mixing time scale represented by its dissipation $\widetilde{\epsilon}$ and kinetic energy $\widetilde{k}$. The better known **Eddy Dissipation Model** has its origin in the EBU model [43]. The general advantage of EBU models is their simplicity and they are computationally inexpensive [44], but tend to produce errors in flow regions of high strain rates. These regions can be found near walls or downstream of a bluff-body.

More sophisticated models are employed for combustion which comprise finite-rate chemistry. One of the first established models is the **Stationary Laminar Flamelet Model (SLFM)** [45]. The idea is to transform the species conservation equation into the so-called stationary laminar flamelet equation by assuming terms involving transients and those involving gradients parallel to the instantaneous surface of the mixture fraction to be small. This leads to the assumption that flame reaction zones are thin, so that their structure can be treated as in laminar flames. To obtain the quantities (composition, temperature, reaction rate) depending on mixture fraction ξ and scalar dissipation η, pre-calculated libraries are introduced. Similar to the mixing-controlled concept a presumed joint PDF (Probability Density Function) of ξ and η allows mean values to be predicted [46]. This concept gives a simple way to include complex chemistry in a turbulent flame. However this concept has it limitations, especially in the presence of local extinction and ignition [47]. In autoignition, the model is not able to account for the effects of the fluctuations of the scalar dissipation [48].

A more general modeling approach is the **Probability Density Function (PDF) method** [49], [15]. The primary advantages of this approach are that independent turbulent fluctuations of all species can be represented, and that the direct effects of reaction appear in closed form [50]. A model is needed to account for mixing. To establish turbulent combustion simulations with the PDF method a very large number of stochastic realizations are necessary. This makes this approach computationally intensive and expensive.

Another approach, based on experimental results in diffusion flames [51] and reactive mixing layers [52], called **Conditional Moment Closure (CMC)** was introduced [10; 53; 54]. In this method transport equations are derived for conditionally averaged reactive scalars. In non-premixed combustion, the mixture fraction ξ is the key variable for the conditioning. The idea of the concept is that fluctuations in temperature and composition are closely linked to the fluctuations of ξ. So the above presented energy and species equation can be reformulated in terms of conditional averages, conditional on a certain value of ξ. The closure now of the conditional average reaction rates can be done by first-order CMC closure [55; 56] or second-order CMC closure [57; 58]. It has been found [59] that for extinction and ignition phenomena, first-order closure is not accurate enough.

For this project the CMC method is chosen due to its ability to account for the effects of finite-rate chemistry, as well as diffusion and convection in space. This makes it a candidate for successful modeling since the goal of the project is to investigate ignition phenomena of liquid fuel combustion.

2.2 Two-phase flow modelling

Two-phase flow modelling plays a vital role in combustion simulations, since in a wide range of combustion problems fluid or solid fuel is used together with a gaseous oxidizer. Liquid fuels are used in engineering applications such as aircraft or static gas turbines, diesel engines, liquid rockets and industrial furnaces. Since the physics behind two-phase combustion is much more complex than in purely gaseous combustion,

its understanding is less advanced and hence still further investigation is needed. Additional to chemical reactions and molecular transport, which are present in pure gas phase phenomena, various processes inside the liquid phase and on surface between gaseous and liquid phases have to be considered, as well as the droplet break up and atomization process of the liquid after injection into the gaseous bulk flow. This increases the demand on modelling tools for two-phase flows to integrate all physical aspects of the gaseous and fluid phase but also to keep computational costs reasonably low. To reduce computational costs, certain aspects of the physical problem are accounted for with simplified models, like for physics inside the liquid phase or the physical exchange between liquid and gaseous phase. Reference to combustion of liquid fuels can be found in Spalding [60], Williams [61], Faeth [62] and Law [63].

2.2.1 Physical description

As a starting point for a physical description of spray combustion, Figure 2.2 shows the group combustion diagram by Chiu et al. [1], which classifies different flame structures in the presence of a droplet mist.

Depending on a dimensionless number, the group combustion number G, four different classes of spray combustion can be characterized. The group combustion number G can be described, as done in Ref. [1], by the ratio of the droplet evaporation speed and the molecular diffusion speed in the gas phase as:

$$G \approx \frac{5N^{2/3}}{S} \tag{2.31}$$

where N is the number of droplets and S the separation parameter. The separation parameter is a function of the inter-droplet space d, the Prandtl number Pr, droplet Reynolds number Re_d and liquid droplet radius r_d.

$$S = \frac{0.05d}{(1 + 0.276Re^{\frac{1}{2}}Pr^{\frac{1}{3}})r_d} \tag{2.32}$$

Depending on G four different combustion modes can be found. A visualization of the different group combustion regimes can be seen in Figure 2.3.

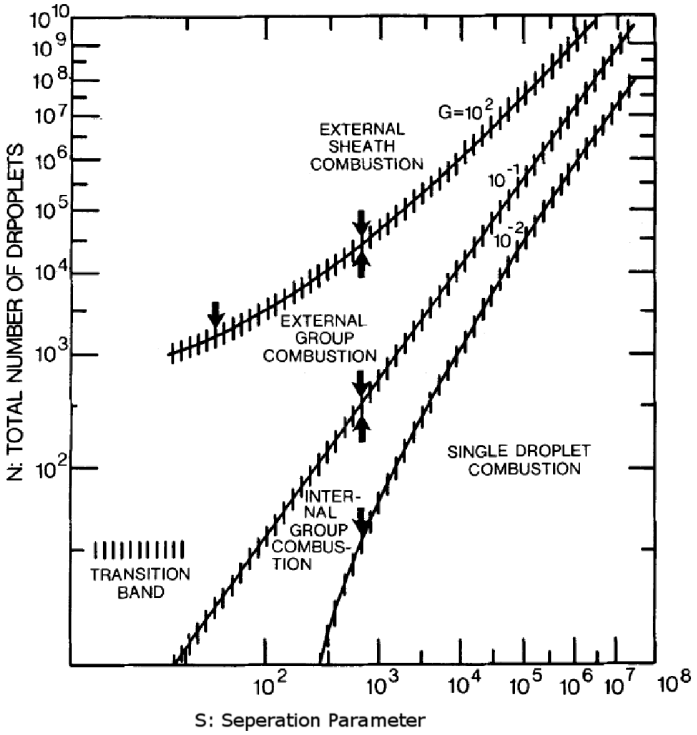

Figure 2.2: Group combustion diagram (Chiu [1])

The region for $G < 10^{-2}$ is denoted as single droplet combustion region. In this region droplets are far away from each other (high separation number S) so that the evaporation and combustion process can take place around a single droplet without interacting with neighboring droplets. For sprays with a high number of droplets, to stay within the single droplet combustion regime, the separation S has to be increased. Sprays within $10^{-2} < G < 10^{-1}$ are in the internal group combustion regime. This regime has two modes, an inner preheating zone where vaporization takes place and an outer combustion zone with individual burning droplets [1]. Between the inner preheating zone and the outer combustion zone a circular diffusion flame is located. The fuel vapor, produced by the evaporation of the droplets in the preheating zone, diffuses outward towards the diffusion flame while oxygen is supplied from the outside. For sprays with a group combustion number G higher than unity, the regime switches from internal to external group combustion until $G < 10^2$. Similar to the internal group combustion regime, in the external a inner preheating zone exists where droplets evap-

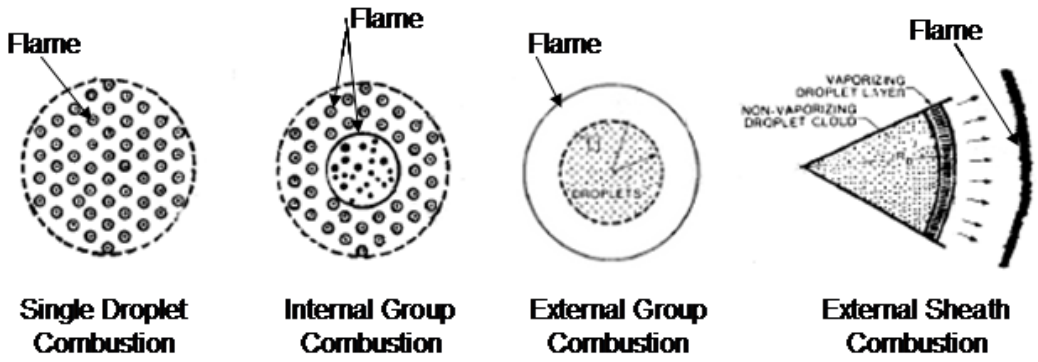

Figure 2.3: Combustion regimes of a droplet spray (Chiu [1])

orate. But there is no single droplet combustion taking place since droplets are too close to each other. This results in a diffusion flame at a certain distance of the evaporating droplet cloud. The region for $G > 10^2$ is called the external sheath combustion. In this regime droplets are so close together to each other that only the outer layer of the droplet cloud is evaporating while the inner droplets are not. The diffusion of fuel from the evaporating droplets establishes a flame at a distance from the droplet cloud.

A physical description of single droplet combustion starts at the physical description of the evaporation process of a single, motionless droplet with temperature T_d surrounded by a stagnant, gravity-free medium with temperature T_a which is not constrained. The understanding of this basic model of an evaporating droplet will be the basis for closure assumptions in Chapter 3 for the droplet evaporation source terms in the extended CMC model. For evaporation to take place T_a has to be higher than T_d and the pressure of the medium p_a has to be much lower than the critical pressure [63]. Figure 2.4 shows a configuration of this process. Since no convection is present around the droplet the evaporation takes place in a spherically symmetric manner.

Due to the higher temperature in the surrounding medium, heat is transferred into the droplet through conduction, heating up the droplet liquid. Part of the heat gasifies the liquid on the droplet surface, creating a fuel vapor. The fuel vapor produced on the droplet surface will then slow down further gasification of liquid when it reaches its

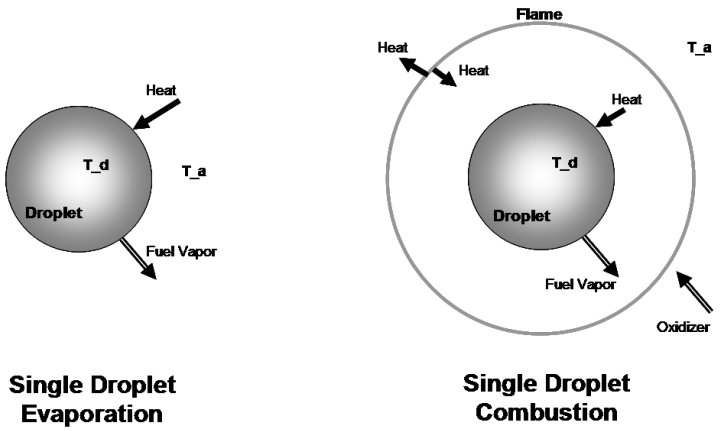

Figure 2.4: Schematic of single evaporating droplet (left) and of single droplet combustion (right) in non-convective environment.

saturation value. But since originally no fuel is available in the surrounding medium the gasified liquid fuel on the droplet surface creates a vapor concentration gradient around the droplet causing the fuel vapor to be transported spherically outward. This slow convective motion is called the Stefan flow [2]. This leads to a process of continuous evaporation of the droplet liquid, with the process rate being controlled by the heat transfer into the droplet and mass diffusion away from it [64].

The physical description of the Stefan flow can be described starting from an open container filled with liquid A, where over the rim of the container a constant air flow of a mixture of gas A and B is applied (Fig. 2.5). The container is of height $x = l$ and is filled with liquid A to the level of $x = 0$. The vapor concentration of A on the liquid surface is $Y_{A,x=0}$.

Due to the constant air flow over the container a constant concentration of the liquid $Y_{A,x=l}$ is established. If the concentration $Y_{A,x=l}$ is less than $Y_{A,x=0}$, liquid vapor will diffuse from the liquid surface towards the open end of the container. Considering that gas B is insoluble into the liquid A, no transport of gas B into the container takes place, producing a stagnant concentration of gas B in the container. Therefore the

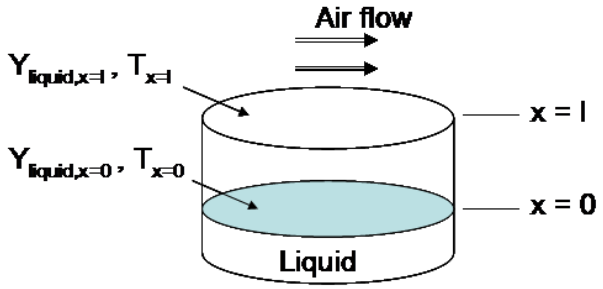

Figure 2.5: Schematic of liquid evaporating from container in to ambiance.

overall conservation of mass can be written as

$$\dot{m} = \dot{m}_A = const. \tag{2.33}$$

Using Fick's Law of Diffusion, for the case of one dimensional binary diffusion for a non-reacting mixture of gas A and B, $\dot{m}_A$ can be written as:

$$\dot{m}_A = Y_A \dot{m}_A - \rho A_C D_{AB} \frac{dY_A}{dx} \tag{2.34}$$

where the first term on the right hand side denotes the mass flow of species A associated with bulk flow and the second term for the mass flow of species A associated with molecular diffusion. A_C is the cross area of the container and D_{AB} the diffusion coefficient. Assuming $\rho A_C D_{AB}$ constant, Eq. (2.34) can be integrated to yield

$$-\frac{\dot{m}_A}{\rho A_C D_{AB}} x = -\ln\left[1 - Y_A\right] + C \tag{2.35}$$

Applying the boundary condition $Y_A(x = 0) = Y_{A,x=0}$ gives $C = \ln\left[1 - Y_{A,x=0}\right]$. Rearrangement of Eq. (2.35) yields the following mass fraction distribution

$$Y_A(x) = 1 - (1 - Y_{A,x=0}) \exp\left[\frac{\dot{m}_A x}{\rho A_C D_{AB}}\right] \tag{2.36}$$

To determine $\dot{m}_A$, $Y_A(x = l) = Y_{A,x=l}$ in Eq. 2.36 gives

$$\dot{m}_A = \frac{\rho A_C D_{AB}}{l} \ln\left[\frac{1 - Y_{A,x=l}}{1 - Y_{A,x=0}}\right] \tag{2.37}$$

It can be seen from Eq. (2.37) that a longer distance l results in a lower mass flux while a higher mass diffusivity D_{AB} produces a larger mass flux. Transforming the Stefan flow problem to spherical coordinates gives a first simple droplet evaporation model, where $\dot{m}$ based on Eq. (2.37) can be written as

$$\dot{m} = 4\pi r_d \rho D_{AB} \ln\left[\frac{1 - Y_{A,\infty}}{1 - Y_{A,s}}\right] \tag{2.38}$$

where r_d is the droplet surface radius and $Y_{A,\infty}$ is the species concentration of A in infinity of the gas phase. The expression in brackets on the right hand side of Eq. (2.37) can be found in the literature as

$$1 + B_Y = \frac{1 - Y_{A,\infty}}{1 - Y_{A,s}} \tag{2.39}$$

where B_Y is commonly called Spalding number or transfer number. The subscript Y indicates that the transfer number is based on mass transfer considerations. A similar expression for the transfer number can be found in terms of the heat transfer rate on the droplet and gas phase interface, which will be presented later in this chapter.

The concentration on the liquid-vapor interface $Y_{A,x=0}$ can be estimated by assuming that liquid and the vapor phase of species A are in equilibrium. Together with the assumption of ideal gases, the partial pressure of species A $p_{A,x=0}$ in the gaseous phase is then equal to the saturation pressure p_{sat} of the liquid fluid. Associating p_{sat} with the liquid temperature T_A gives

$$p_{A,x=0} = p_{sat}(T_A) \tag{2.40}$$

where partial pressure of species A can be related to mole fraction of species A

$$\chi_{A,x=0} = \frac{p_{sat}}{p} \tag{2.41}$$

To estimate p_{sat}/p the Clausius-Clapeyron equation is used:

$$\frac{dp}{p} = \frac{h_{fg}}{R_u/MW_A}\frac{dT}{T^2} \tag{2.42}$$

where h_{fg} is the latent heat of vaporization, defined as the amount of heat needed to completely vaporize a unit mass of liquid at a given temperature and constant pressure. MW_A and R_u are the molecular weight of species A and the universal gas constant, respectively. Integrating Eq. (2.42) with the reference state at $p = 1.013$ bar and the boiling temperature of the liquid T_{boil} gives:

$$\frac{p_{sat}}{p} = \exp\left[-\frac{h_{fg}}{(R_u/MW_A)}\left(\frac{1}{T} - \frac{1}{T_{boil}}\right)\right] \tag{2.43}$$

Substituting Eq. (2.43) into Eq. (2.41) and using $MW_{mix} = \chi_A MW_A + (1 - \chi_{A,x=0})MW_B$, where MW_B is the molecular weight of gas B, gives

$$Y_{A,x=0} = \frac{MW_A}{MW_{mix}} \exp\left[-\frac{h_{fg}}{(R_u/MW_A)}\left(\frac{1}{T} - \frac{1}{T_{boil}}\right)\right] \tag{2.44}$$

Model of Single Droplet Evaporation With the above mentioned equations it is possible now to establish the vapor mass concentration on a liquid surface by knowing the temperature on the interface between liquid and gas phase. With the above state assumptions and the gas phase energy equation the gas phase temperature as a function of radial distance from the droplet can be established which allows to establish the conductive heat transfer into the droplet. With the further assumptions of a single component liquid, a uniform droplet temperature and binary diffusion with a unity Lewis number the gas phase energy equation can be written as

$$\frac{d\left(r^2 \frac{dT}{dr}\right)}{dr} = \frac{\dot{m} c_{pg}}{4\pi k} \frac{dT}{dr} \tag{2.45}$$

where c_{pg} and k are the specific heat in the gas phase and the thermal conductivity, respectively. In Eq. (2.45) it is assumed that no reactions take place in the gas phase. To solve Eq. (2.45) two boundary conditions are required. The temperature on the droplet surface r_d is set to the boiling temperature $T_{A,boil}$ of species A and the temperature seen at infinity r_∞ in the gas phase is T_∞. After double integration the gas phase temperature distribution can be written as:

$$T(r) = \frac{(T_\infty - T_{A,boil}) \exp\left(-\frac{c_{pg}}{4\pi k}\frac{\dot{m}}{r}\right) - T_\infty \exp\left(-\frac{c_{pg}}{4\pi k}\frac{\dot{m}}{r_d}\right) + T_{A,boil}}{1 - \exp\left(-\frac{c_{pg}}{4\pi k}\frac{\dot{m}}{r_d}\right)} \tag{2.46}$$

Since the droplet is assumed to be at the uniform temperature $T_{A,boil}$ all heat which is conducted into droplet $\dot{Q}_{cond}$ at the droplet-gas interface is used for the evaporation process. This gives a connection between $T_{A,boil}$ and mass evaporation rate $\dot{m}$ through the surface energy balance equation

$$\dot{Q}_{cond} = \dot{m}(h_{vap} - h_{liq}) = \dot{m}h_{fg} \tag{2.47}$$

where h_{vap} and h_{liq} are the enthalpy of the vapor and the liquid phase, respectively. Using Fourier's law equation Eq. (2.47) can be rewritten as

$$4\pi k_g r_s^2 \left(\frac{dT}{dr}\right)_{r_d} = \dot{m}h_{fg} \tag{2.48}$$

where $\left(\frac{dT}{dr}\right)_{r_d}$ can be found by differentiating Eq. (2.46). This leads to, solving for $\dot{m}$

$$\dot{m} = \frac{4\pi k r_d}{c_{pg}} \ln\left(\frac{c_{pg}(T_\infty - T_{A,boil})}{h_{fg}} + 1\right) \tag{2.49}$$

which is a similar expression for $\dot{m}$ based on heat transfer, compared to Eq. (2.37) which is based on mass transfer considerations. In the literature, a dimensionless parameter B_q is defined, commonly called the Spalding number or transfer number based on heat transfer:

$$B_q = \frac{c_{pg}(T_\infty - T_{A,boil})}{h_{fg}} \tag{2.50}$$

where 2.50 introduced in Eq. (2.49), it can be seen that the mass evaporation rate is zero for $B_q = 0$. Having the value of $\dot{m}$ allows to establish the droplet history. Based on the assumptions of mass transfer controlled evaporation, the mass balance equation gives the liquid mass rate by which the droplet is decreased:

$$\frac{dm_d}{dt} = -\dot{m} \tag{2.51}$$

where m_d is the mass of the droplet and the negative sign on the right hand side shows that the droplet mass is reduced during the evaporation process. The droplet mass can be expressed as

$$m_d = \frac{4}{3}\rho_l \pi r_d^3 \tag{2.52}$$

Substituting Eq. (2.52) and Eq. (2.49) into Eq. (2.51) and differentiating yields

$$\frac{dr_d}{dt} = -\frac{k_g}{\rho_l c_{pg} r_d} \ln\left(B_q + 1\right) \tag{2.53}$$

In the literature this equation is usually expressed by the square of the droplet diameter $D = 2r_d$:

$$\frac{dD^2}{dt} = -\frac{8k_g}{\rho_l c_{pg}} \ln\left(B_q + 1\right) \tag{2.54}$$

In Eq. (2.54) all parameters on the right hand side are constant hence D^2 changes linearly in time. The right hand side of Eq. (2.54) is the evaporation constant K which visualizes the slope of the square droplet diameter $D^2(t)$ over time:

$$K = \frac{8k_g}{\rho_l c_{pg}} \ln\left(B_q + 1\right) \tag{2.55}$$

Integrating Eq. (2.54), starting from the initial droplet diameter d_0 leads to

$$D^2(t) = D_0^2 - Kt \tag{2.56}$$

which is the D^2law for droplet evaporation. Its linear characteristic can be seen in Figure (2.6), where a cool droplet is placed in a hot and quiescent environment. In the

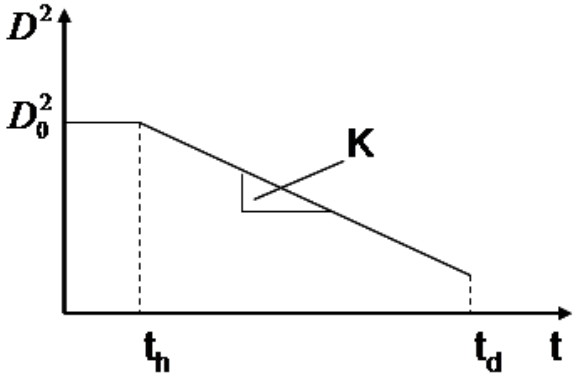

Figure 2.6: Surface change of evaporating droplet showing the preheating zone and the reduction of diameter following the D^2 law.

early droplet life the droplet diameter is almost constant over time. In this phase all the

heat transferred from the gas phase into the liquid phase is used to heat up the droplet and hence almost no evaporation takes place. After time t_h the droplet is heated up sufficiently and evaporation starts which is denoted by the reduction of droplet diameter.

Model of Single Droplet Combustion To extend the single droplet evaporation model to a single burning droplet model, spherically around the evaporating droplet a diffusion flame is placed which surrounds the droplet (Figure 2.3), following [62]. The model presented here is used later in Chapter 4. It is assumed that the flame is in a uniform pressure field and no interactions with other droplets takes place. In addition it is assumed that in the gas phase between the droplet and the diffusion flame only fuel vapor from the droplet and products, while the outer gas phase consists of oxidizer and products. Regarding the flame front, it is assumed that the flame is an infinitesimally thin sheet where reaction takes place infinitely fast in stoichiometric proportions. Finally a Lewis number $Le = k_g/\rho c_{pg} D$ of unity is assumed. Under these assumptions the temperature and mass fraction profiles of a single burning droplet can be seen in Figure 2.7. In the inner region between droplet surface and flame sheet, the temperature rises from the droplet surface temperature T_s to the temperature T_f in the flame. The fuel mass fraction is at $Y_{F,s}$ on the droplet surface and is consumed to zero in the flame sheet. In the outer region the temperature falls from T_f at the flame sheet down to the gas phase temperature T_∞. Oxygen is supplied from the surroundings and completely consumed in the flame sheet. The combustion product mass fraction Y_P has its maximum in the flame sheet and is diffused inwards to the droplet surface and outwards. Since no product can dissolve into the liquid droplet, the product mass fraction in the inner region is stagnant. Thus similar to the Stefan flow problem the species conservation in the inner region between droplet surface and flame sheet can be described by Fick's law:

$$\dot{m}_F = -4\pi r_d^2 \frac{\rho D}{1 - Y_F} \frac{dY_F}{dr} \tag{2.57}$$

To solve Eq. (2.57) it is assumed that on the droplet surface liquid-vapor equilibrium is established, giving $Y_F(r_d) = Y_{F,s}(T_s)$, and that in the flame sheet all fuel vapor is

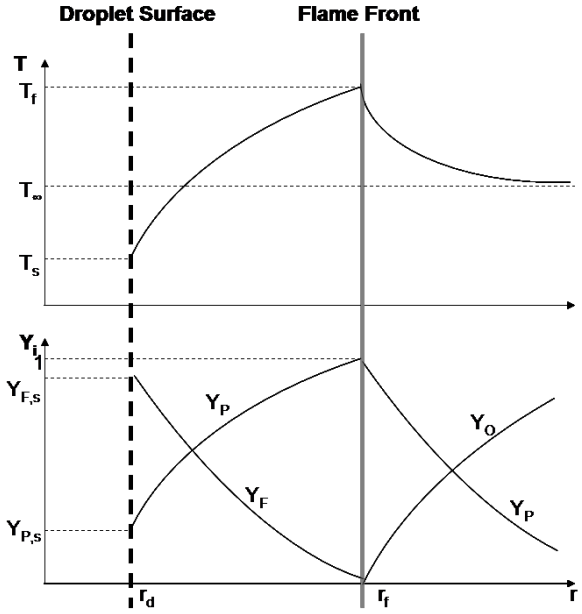

Figure 2.7: Temperature and species mass fraction profiles for single droplet combustion [2].

consumed, so that $Y_F(r_f) = 0$. This gives

$$Y_F(r) = 1 - \frac{(1 - Y_{F,s}) \exp\left(-\frac{1}{4\pi\rho D}\frac{\dot{m}_F}{r}\right)}{\exp\left(-\frac{1}{4\pi\rho D}\frac{\dot{m}_F}{r_d}\right)} \tag{2.58}$$

Since only fuel vapor and products are present in the inner region, Y_P can then be written as

$$Y_P(r) = 1 - Y_F(r) \tag{2.59}$$

In the outer region oxidizer is diffusing radially towards the flame while products are transported away. With the assumption of stoichiometric conditions within the flame sheet, $\dot{m}_O$ can be written as

$$\dot{m}_O = \nu \dot{m}_F \tag{2.60}$$

where ν is the stoichiometric mass ratio. Using Fick's Law as before yields

$$\frac{\dot{m}_O}{\nu} = \dot{m}_F = 4\pi r^2 \frac{\rho D}{\nu Y_O}\frac{dY_O}{dr} \tag{2.61}$$

Integration of Eq. (2.61), assuming that all oxidizer is consumed in the flame sheet ($Y_O(r_f)$) and that $Y_O(r_\infty)$ is unity far from of the droplet, leads to

$$Y_O(r) = \nu \left[\frac{\exp\left(-\frac{1}{4\pi\rho D}\frac{\dot{m}_F}{r}\right)}{\exp\left(-\frac{1}{4\pi\rho D}\frac{\dot{m}_F}{r_f}\right)} - 1 \right] \tag{2.62}$$

As before since in the outer region only oxidizer and products exists, it follows that

$$Y_P(r) = 1 - Y_O(r) \tag{2.63}$$

To derive $T(r)$ for the inner and outer region, Eq. 2.46 is the starting point. With the temperature boundary conditions shown in Figure 2.7, it leads to

$$\begin{aligned} T(r) = \frac{(T_s - T_f)\exp\left(-(1/4\pi k_g)(\dot{m}_F/r)\right) + T_f \exp\left(-(1/4\pi k_g)(\dot{m}_F/r_d)\right)}{\exp\left(-(1/4\pi k_g)(\dot{m}_F/r_d)\right) - \exp\left(-(1/4\pi k_g)(\dot{m}_F/r_f)\right)} \\ - \frac{T_s \exp\left(-(1/4\pi k_g)(\dot{m}_F/r_f)\right)}{\exp\left(-(1/4\pi k_g)(\dot{m}_F/r_d)\right) - \exp\left(-(1/4\pi k_g)(\dot{m}_F/r_f)\right)} \end{aligned} \tag{2.64}$$

for the inner region, while for the outer region

$$T(r) = \frac{(T_f - T_\infty)\exp\left(-(1/4\pi k_g)(\dot{m}_F/r)\right) + \exp\left(-(1/4\pi k_g)(\dot{m}_F/r_f)\right)T_\infty - T_f}{\exp\left(-(1/4\pi k_g)(\dot{m}_F/r_f)\right) - 1} \tag{2.65}$$

To resolve the unknowns T_s and T_f the energy balance on the droplet surface and the flame sheet needs to be established. Regarding the droplet surface, heat is conducted from the flame through the inner region to the droplet surface, where it is assumed that the droplet is immediately heated up and all energy is used for evaporation. With Eq. (2.48) and using Eq. (2.64) leads to

$$\frac{c_{pg}(T_f - T_s)}{h_{fg}} \frac{\exp\left(-1/(4\pi k_g)\dot{m}_F/r_d\right)}{\exp\left(-1/(4\pi k_g)\dot{m}_F/r_d\right) - \exp\left(-1/(4\pi k_g)\dot{m}_F/r_f\right)} + 1 = 0 \tag{2.66}$$

The energy balance at the flame sheet can be written as

$$\dot{m}_F h_F + \dot{m}_O h_O - \dot{m}_P h_P = \dot{Q}_{f,-} + \dot{Q}_{f,+} \tag{2.67}$$

where $\dot{Q}_{f,-}$ and $\dot{Q}_{f,+}$ is the heat flux inwards and outwards from the flame sheet, respectively. h_F, h_O and h_P are the enthalpies for fuel, oxidizer and products, respectively. The left hand side of Eq. (2.67) can be substituted by $\dot{m}_F \Delta h_c$, which is the rate at which chemical energy is converted to thermal energy in the flame sheet. Using Fourier's law as before the right hand side of Eq. (2.67) can be rewritten and leads with Eq. (2.64) to

$$\frac{c_{pg}}{\Delta h_c} \frac{(T_s - T_f)\exp\left(-1/(4\pi k_g)\dot{m}_F/r_f\right)}{\exp\left(-1/(4\pi k_g)\dot{m}_F/r_d\right) - \exp\left(-1/(4\pi k_g)\dot{m}_F/r_f\right)} - \frac{(T_\infty - T_f)\exp\left(-1/(4\pi k_g)\dot{m}_F/r_f\right)}{1 - \exp\left(-1/(4\pi k_g)\dot{m}_F/r_f\right)} - 1 = 0 \tag{2.68}$$

With equations Eq.(2.58), Eq. (2.64), Eq. (2.65), Eq. (2.66) and Eq. (2.68), the burning rate $\dot{m}_F$ can be described as

$$\dot{m}_F = \frac{4\pi k_g r_d}{c_{pg}} \ln\left(1 + B_{b,q}\right) \tag{2.69}$$

with

$$B_{b,q} = \frac{\Delta h_c/\nu + c_{pg}(T_\infty - T_s)}{h_{fg}} \tag{2.70}$$

The flame temperature T_f and radius r_f as

$$T_f = \frac{h_{fg}}{c_{pg}(1+\nu)}[\nu B_{b,q} - 1] + T_s \tag{2.71}$$

$$r_f = r_d \frac{\ln\left(1 + B_{b,q}\right)}{\ln\left[(\nu+1)/\nu\right]} \tag{2.72}$$

On the droplet surface, the fuel vapor mass fraction can be described as

$$Y_{F,s} = \frac{B_{b,q} - 1/\nu}{B_{b,q} + 1} \tag{2.73}$$

Convection: Until now, for both the single droplet evaporation and the burning model, the environment of the droplet was assumed to be stagnant leading to a spherically symmetric evaporation and subsequent burning. But in most two-phase flow problems this is not the case and so approaches to incorporate convection into the model give

a more realistic reflection of the problem. The presence of convection enhances the transport rates of fuel vapor away of the droplet surface and hence increases the evaporation rate. Several approaches are available in the literature [62; 63; 65]. A simple approach, called the 'film theory', moves the boundary conditions for heat and mass transfer used at infinity of the droplet more inwards at a special radial distance of the droplet, for species mass transfer at the film radius δ_M and for heat transfer at the film radius δ_T. Since the previous boundary conditions at infinity are now nearer to the droplet surface, the resulting species concentration and temperature gradients are steepened and hence the mass- and heat transfer at the droplet surface is increased. Both the film radius for mass transfer and defined in terms of the Nusselt number Nu and Sherwood number Sh, respectively:

$$\frac{\delta_M}{r_d} = \frac{Sh}{Sh - 2} \tag{2.74}$$

$$\frac{\delta_T}{r_d} = \frac{Nu}{Nu - 2} \tag{2.75}$$

With the assumption of unity Lewis number it follows $Sh = Nu$, the following correlation for a burning droplet under convection to establish Sh and Nu can be found in [62]

$$Nu = Sh = 2 + \frac{0.555 R^{1/2} Pr^{1/2}}{[1 + 1.232/(RePr^{4/3})]^{1/2}} \tag{2.76}$$

where Re is the Reynolds number based on r_d and the relative velocity droplet and gas phase. The burning rate $\dot{m}_F$ incorporating forced convection can be written

$$\dot{m}_F = \frac{2\pi k_g r_d Nu}{c_{pg}} \ln\left(1 + B_{b,q}\right) \tag{2.77}$$

For a stagnant gas phase the Nusselt number is $Nu = 2$ and Eq. (2.77) is equal to Eq. (2.69).

2.2.2 Lagrangian approach

In the Lagrangian approach for two-phase flows the liquid phase is assumed to be local source of fuel, whose properties are calculated in a Lagrangian context. The equations

presented here are used in the DNS study in Chapter 4. First presented here is the traditional approach where a constant gaseous specific heat capacity C_{pg} is assumed, as well as constant transport properties and unity Lewis number. The two-way coupling between the phases is represented by additional source terms. Several assumptions, as described above, are used to create a simple model. Flow circulation and temperature non-uniformities inside the droplets and droplet interactions are neglected. Since the liquid droplets have a much larger density than that of the surrounding ambient gas the momentum exchange with the carrier gas is assumed to be only a function of the drag force [65].

The position $\boldsymbol{X}_k$ and velocity $\boldsymbol{V}_k$ of the $k-$th droplet are given by [24]:

$$\frac{d\boldsymbol{X}_k}{dt} = \boldsymbol{V}_k \tag{2.78}$$

$$\frac{d\boldsymbol{V}_k}{dt} = \frac{1}{\tau_{d,k}}(\boldsymbol{U}(\boldsymbol{X}_k) - \boldsymbol{V}_k) \tag{2.79}$$

where $\boldsymbol{U}$ is the gas velocity and $\tau_{d,k}$ is the droplet relaxation time

$$\tau_{d,k} = \frac{\rho_l \Theta_k^2}{18 C_{D,k} \mu} \tag{2.80}$$

where Θ_k is the $k-$th droplet diameter, μ the viscosity of the gas and ρ_l the liquid density. $C_{D,k}$ is the drag coefficient correction for finite Re_k [66] which can be described by

$$C_{D,k} = 1 + \frac{Re_k^{2/3}}{6} \tag{2.81}$$

with the droplet Reynolds number

$$Re_k = \frac{\rho}{\mu}|\boldsymbol{U}(\boldsymbol{X}_{k,t}) - \boldsymbol{V}_k|\Theta_k \tag{2.82}$$

The droplet temperature T_k and droplet diameter Θ_k are obtained by solving the mass and heat balance equations at the droplet surface for $Le = 1$ [16]

$$\frac{\Theta_k^2}{dt} = -\frac{\Theta_k^2}{\tau_{k,v}} \tag{2.83}$$

$$\frac{T_k}{dt} = \frac{T(\boldsymbol{X}_k, t) - T_k - (B_k L_{vap})/C_{pg}}{\tau_{k,T}} \tag{2.84}$$

where

$$\tau_{k,v} = \frac{Sc\rho_l\Theta_k^2}{4Sh\mu\ln(1+B_q)} \tag{2.85}$$

$$\tau_{k,T} = \frac{Pr}{6Nu}\frac{C_{pl}}{C_{pg}}\frac{\rho_l\Theta_k^2}{\mu}\frac{B_q}{\ln(1+B_q)} \tag{2.86}$$

where C_{pl} is the heat capacity of the liquid, L_{vap} the latent heat of evaporation and $Pr = Sh = 0.7$. The convective Sherwood and Nusselt number are described by Eq. 2.76.

In Chapter 4, the gas phase will be treated as a compressible Newtonian fluid following the equation of state for a perfect gas. The mass, momentum and energy balance equation for the gas phase can be written as [24]

$$\frac{\partial\rho}{\partial t} + \frac{\partial\rho U_j}{\partial x_j} = \dot{m} \tag{2.87}$$

$$\frac{\partial\rho U_i}{\partial t} + \frac{\partial\rho U_i U_j}{\partial x_j} = -\frac{\partial P}{\partial x_i} + \frac{\partial\sigma_{ij}}{\partial x_j} + \dot{v}_i \tag{2.88}$$

$$\frac{\partial\rho E}{\partial t} + \frac{\partial(\rho E + \rho RT)}{\partial x_j} = \frac{\partial}{\partial x_j}\left(\lambda\frac{\partial T}{\partial x_j}\right) + \frac{\partial\sigma_{ij}U_j}{\partial x_i} + \rho\dot{\omega} + \dot{e} \tag{2.89}$$

with

$$\sigma_{ij} = \mu\left(\frac{\partial U_i}{\partial x_j} + \frac{\partial U_j}{\partial x_i}\right) - \frac{2}{3}\mu\frac{\partial U_k}{\partial x_k}\delta_{ij} \tag{2.90}$$

where δ_{ij} is the Kroneker symbol. The mass fraction balance equations for the fuel Y_F and oxidizer Y_O can be written as

$$\frac{\partial\rho Y_F}{\partial t} + \frac{\partial(\rho U_j Y_F)}{\partial x_j} = \frac{\partial}{\partial x_j}\left(\rho D\frac{\partial Y_F}{\partial x_j}\right) + \rho\dot{\omega}_F + \dot{m} \tag{2.91}$$

$$\frac{\partial\rho Y_O}{\partial t} + \frac{\partial(\rho U_j Y_O)}{\partial x_j} = \frac{\partial}{\partial x_j}\left(\rho D\frac{\partial Y_O}{\partial x_j}\right) + \rho\dot{\omega}_O \tag{2.92}$$

In Eq. 2.87, Eq. 2.88, Eq. 2.89 and Eq. 2.91, $\dot{m}$, $\dot{v}_k$ and $\dot{e}_k$ are the additional source

terms occurring from the droplet evaporation. For the summation of all droplets located in a specific cell of the Eulerian mesh with volume V, the mass source term $\dot{m}$ is

$$\dot{m} = \rho_l \frac{\pi}{4} \frac{1}{V} \sum_k \frac{\Theta_k^3}{\tau_{k,v}} \tag{2.93}$$

Similar for all droplets in a specific cell the momentum and energy source terms can be written as

$$\dot{v}_i = \frac{1}{V} \sum_k -\frac{dm_k \boldsymbol{V}_{k,i}}{dt} \tag{2.94}$$

$$\dot{e} = -\frac{1}{V} \sum_k -\frac{dm_k C_{pl} T_k}{dt} \tag{2.95}$$

where m_k is the mass of the $k-$th droplet.

A more sophisticated model for the Lagrangian phase [67] uses a spherically symmetric formulation with finite conductivity in the liquid. Inside the droplet an axisymmetric circulation model is assumed for droplet Reynolds numbers much larger than unity. But this model is restricted to simulations with few droplets since otherwise the computational expense of resolving the droplet interior would be too large [68]. More sophisticated models are available in literature to establish the relationship of the evaporation rate and the droplet diameter [29; 69].

Chapter 3

Conditional Moment Closure

3.1 Chapter objective

In this chapter the Conditional Moment Closure (CMC) equations and closures are presented, including the extended equations for two-phase modelling which will be implemented later in Chapter 5 and 6. As for the derivation of the single phase CMC equations, the decomposition method by Bilger [10] is used for the derivation of the two-phase flow extended CMC equations. For both temperature and mass fraction CMC equations additional source terms appear due to the droplet evaporation process. For the presumed PDF approach the equation for the mean and variance of mixture fraction for two-phase flows is presented using the closure model by Demoulin and Borghi [11] for the closure of the droplet source terms in the mixture fraction variance equation.

3.2 Conditional Moment Closure

In Conditional Moment Closure (CMC) methods, the underlying hypothesis is that most of the fluctuations in the scalar quantities of interest can be associated with the fluctuation of only one key quantity [54]. For non-premixed combustion, this is the mixture fraction. The resulting equations for the conditionally-averaged reactive scalars are then dependent on time, on the three spatial dimensions and additionally on mixture fraction. An advantage of the conditioning is that conditional fluctuations of

the reactive components are significantly smaller than the unconditional fluctuations and can often be neglected, when calculating the value of the chemical source term (first-order CMC). But for large conditional fluctuations of reactive components, second moments should be used for the closure of the chemical source term (second-order CMC) [54].

3.2.1 Conditional statistics

For the better understanding of the CMC model it is helpful to revisit the statistical description of turbulent flows, which can be found in [6; 15]. In turbulent flows for a random variable $y(\boldsymbol{x}, t)$, the probability p of $y(\boldsymbol{x}, t)$ being within a given range dZ can be established with the help of its probability density function (PDF) $P(Z; \boldsymbol{x}, t)$ as:

$$P(Z; \boldsymbol{x}, t) = \frac{dp(Z < y(\boldsymbol{x}, t) < Z + dZ)}{dZ} \tag{3.1}$$

where $P(Z; \boldsymbol{x}, t)$ is the probability density in Z-space depending on location ($\boldsymbol{x}$) and time (t). Integrating $y(\boldsymbol{x}, t)$ over whole range of dZ gives:

$$\int_{-\infty}^{+\infty} P(Z) dZ = 1 \tag{3.2}$$

For a given $P(Z; \boldsymbol{x}, t)$ the n-th moment of Z can be defined as:

$$\overline{Z(\boldsymbol{x}, t)^n} = \int_{-\infty}^{+\infty} Z^n P(Z; \boldsymbol{x}, t) dZ \tag{3.3}$$

where for $n = 1$, $\overline{Z(\boldsymbol{x}, t)^n}$ is the mean of Z. Central moments are defined by:

$$\overline{[Z(\boldsymbol{x}, t) - \overline{Z(\boldsymbol{x}, t)}]^n} = \int_{-\infty}^{+\infty} (Z - \overline{Z})^n P(Z; \boldsymbol{x}, t) dZ \tag{3.4}$$

where for $n = 2$, $\overline{[Z(\boldsymbol{x}, t) - \overline{Z(\boldsymbol{x}, t)}]^n}$ is the variance of Z.

To establish conditional PDFs and expectations, a certain selected range of realizations of the flow is taken into account out of the ensemble of all realizations, specified

by a condition. For two random variables y_1 and y_2, the joint PDF can be decomposed, using Bayes theorem as:

$$P(Z_1, Z_2) = P(Z_1|y_2 = Z_2)P(Z_2) \tag{3.5}$$

where $P(Z_1|y_2 = Z_2)$ is the conditional PDF. The conditional mean of y_1, for the condition $y_2 = Z_2$, is then defined as:

$$\langle y_1|y_2 = Z_2\rangle = \int_{-\infty}^{+\infty} Z_1 P(Z_1|y_2 = Z_2)dZ_1 = \frac{\int_{-\infty}^{+\infty} Z_1 P(Z_1, Z_2)dZ_1}{P(Z_2)} \tag{3.6}$$

In the following, to simplify the notation, $\langle y_1|y_2 = Z_2\rangle$ will be written as $\langle y_1|Z_2\rangle$. The expression $\langle f|a = b\rangle$ denotes an ensemble averaging over all cases that fulfill the condition on the right hand side (r.h.s.) of the vertical bar. The conventional unconditional mean value is obtained by:

$$\overline{y_1} = \int_{-\infty}^{+\infty} \langle y_1|Z_2\rangle P(Z_2)dZ_2 \tag{3.7}$$

Only if y_1 and y_2 are statistically independent from each other, $\overline{y_1}$ equals $\langle y_1|Z_2\rangle$.

3.2.2 Conditional equations

The conditional mean of the mass fraction Y_α of species α and the temperature T, are defined by

$$Q_\alpha(\eta, x_j, t) = \langle Y_\alpha(x_j, t)|\xi(x_j, t) = \eta\rangle \tag{3.8}$$

$$Q_T(\eta, x_j, t) = \langle T(x_j, t)|\xi(x_j, t) = \eta\rangle \tag{3.9}$$

where η is the sample space variable for the conserved scalar, here the mixture fraction ξ. The instantaneous value of Y_α and T can be then decomposed as

$$Y_\alpha(\eta, x_j, t) = Q_\alpha(x_j, t) + Y''_\alpha \tag{3.10}$$

$$T(\eta, x_j, t) = Q_T(x_j, t) + T'' \tag{3.11}$$

where Y''_α and T'' are the conditional fluctuations around the conditional mean mass fraction of species α and conditional mean temperature, respectively. Differentiating Eq. (3.10) and (3.11) with respect to time gives

$$\frac{\partial Y_\alpha}{\partial t} = \frac{\partial Q_\alpha}{\partial t} + \frac{\partial Q_\alpha}{\partial \eta}\frac{\partial \xi}{\partial t} + \frac{\partial Y''_\alpha}{\partial t} \tag{3.12}$$

$$\frac{\partial T}{\partial t} = \frac{\partial Q_T}{\partial t} + \frac{\partial Q_T}{\partial \eta}\frac{\partial \xi}{\partial t} + \frac{\partial T''}{\partial t} \tag{3.13}$$

and the gradient operator to Eq. (3.10) and Eq. (3.11) gives

$$\nabla Y_\alpha = \nabla Q_\alpha + \frac{\partial Q_\alpha}{\partial \eta}\nabla \xi + \nabla Y''_\alpha \tag{3.14}$$

$$\nabla T = \nabla Q_T + \frac{\partial Q_T}{\partial \eta}\nabla \xi + \nabla T'' \tag{3.15}$$

Conditional mass fraction equation: Following [70] the starting point of the derivation of the CMC equation are the continuity equation Eq. (2.1), mass species transport equation Eq. (2.11) and mixture fraction equation Eq. (2.22), described in Chapter 2. Substituting Eq. (3.14) in the divergence of the diffusional flux in Eq. (2.11) leads to

$$\begin{aligned}\nabla \cdot [\rho D \nabla Y(x,t)] = \nabla \cdot [\rho D \nabla Q(\xi)] + \frac{\partial Q(\xi)}{\partial \eta}\nabla \cdot (\rho D \nabla \xi) \\ + \rho D \nabla \xi \cdot \nabla \xi Q''(\xi) + \rho D \nabla \xi \cdot \nabla Q'(\xi)\end{aligned} \tag{3.16}$$

Substituting Eq. (3.12), Eq. (3.14) and Eq. (3.16) in Eq. (2.11), and using Eq. (2.22), yields

$$\begin{aligned}\dot{\omega} = \rho \dot{Q}(\xi) + \rho u \cdot \nabla Q(\xi) - \rho D \nabla \xi \cdot \nabla \xi Q''(\xi) \\ -\nabla \cdot (\rho D \nabla Q) - \rho D \nabla \xi \cdot \nabla Q - \frac{\partial Q(\xi)}{\partial \eta}\nabla \cdot [\rho (D - D^*) \nabla \xi] + \rho \frac{\partial y}{\partial t} \\ \rho u \cdot \nabla y - \nabla \cdot (\rho D \nabla y)\end{aligned} \tag{3.17}$$

where D^* is the conserved scalar molecular diffusivity [70]. Taking the conditional expectation of Eq. (3.17), conditional on $\xi = \eta$, yields for constant property flow

$$\begin{aligned} \rho\dot{Q} + \rho\langle u|\eta\rangle \cdot \nabla Q = \langle\dot{\omega}|\eta\rangle \\ +\rho D\langle\nabla\xi \cdot \nabla\xi|\eta\rangle Q'' + e_Q + e_y \end{aligned} \tag{3.18}$$

with

$$\begin{aligned} e_Q = \nabla \cdot \left(\rho D \frac{\partial Q}{\partial \eta}\right) \\ +\langle\left(\rho D\nabla\xi \cdot \frac{\partial}{\partial\eta}\nabla\xi + \frac{\partial Q}{\partial\eta}\nabla \cdot [\rho(D - D^*)\nabla\xi]\right)|\eta\rangle \end{aligned} \tag{3.19}$$

$$e_y = -\langle\left(\rho\frac{\partial y}{\partial t} + \rho u \cdot \nabla y - \nabla \cdot (\rho D\nabla y)\right)|\eta\rangle \tag{3.20}$$

Following [54] e_Q can be neglected in the further derivation and using the closure hypothesis for e_y

$$e_y = -\frac{\nabla \cdot [\langle u''y''|\eta\rangle\rho P(\eta)]}{P(\eta)} \tag{3.21}$$

Equation (3.18) can be written as

$$\begin{aligned} \frac{\partial Q}{\partial t} + \langle u|\eta\rangle \bullet \nabla Q + \frac{\nabla \cdot [\langle u''y''|\eta\rangle\rho P(\eta)]}{\bar{\rho}P(\eta)} \\ = \langle\dot{\omega}|\eta\rangle + \langle N|\eta\rangle\frac{\partial^2 Q}{\partial\eta^2} \end{aligned} \tag{3.22}$$

3.2.3 Closure assumptions

Reaction rate: In equation (3.22), the conditional chemical source terms need to be closed. Using mixture fraction as the conditioning variable, the conditional fluctuations of the reactive scalars can be low. For first-order closure this involves expressing the conditional expectation of the chemical source term as a function of the conditional mean mass fraction, temperature and pressure, disregarding the conditional fluctuations [9]

$$\langle\dot{\omega}_\alpha|\eta\rangle = \dot{\omega}_\alpha(Q_\alpha, Q_T, p) \tag{3.23}$$

$$\langle \dot{\omega}_H | \eta \rangle = \sum_{\alpha=1}^{N} h_\alpha \langle \dot{\omega}_\alpha | \eta \rangle \tag{3.24}$$

For larger conditional fluctuations of the reactive scalars, alternative closures such as second-order closure [71] or double conditioned closure [72] has to be used.

Conditional Scalar dissipation: The scalar dissipation rate $\langle N|\eta\rangle$ can be described by the Amplitude Mapping Closure (AMC) model [73] by

$$\begin{aligned} \langle N|\eta\rangle &= N_0 G(\eta) \\ G(\eta) &= \exp\left(-2[\mathrm{erf}^{-1}(2\eta-1)]^2\right) \\ N_0 &= \frac{\tilde{\chi}}{2\int_0^1 G(\eta)\tilde{P}(\eta)d\eta} \end{aligned} \tag{3.25}$$

where the mean scalar dissipation rate $\tilde{\chi}$ is computed from the mean turbulence quantities of the flow field.

Conditional velocity: The conditional expectation of the velocity can be closed by a linear approximation [54]

$$\langle u_j|\eta\rangle = \tilde{u}_j + \frac{\widetilde{u_j''\xi''}}{\widetilde{\xi''^2}}(\eta - \tilde{\xi}) \tag{3.26}$$

and the unconditional covariance

$$\widetilde{u_j''\xi''} = -D_t \frac{\partial \tilde{\xi}}{\partial x_j} \tag{3.27}$$

Conditional turbulent flux: Closure for the conditional turbulent flux can be found by analogy with the diffusion approximation used for the unconditional scalar flux

$$\langle u_j'' y''|\eta\rangle = -D_t \frac{\partial Q}{\partial x_j} \tag{3.28}$$

$$\langle u_j'' T'' | \eta \rangle = -D_t \frac{\partial Q_T}{\partial x_j} \tag{3.29}$$

$$\langle u_j'' h'' | \eta \rangle = -D_t \frac{\partial Q_h}{\partial x_j} \tag{3.30}$$

however its validity is not fully investigated. Especially Counter-gradient fluxes have been observed [9].

3.3 Conditional Moment Closure for two-phase flows

There are several applications of the CMC method to spray combustion in literature. For Diesel engine spray combustion the CMC method was used [74] with the approach of neglecting all source terms due to evaporation except in the mean mixture fraction equation. In the attempt to account for all droplet source terms, various studies derived the conditional species and temperature equations [56; 75; 76], but leading to different versions inconsistent with one another. For the droplet source terms in the mixture fraction variance equation different closure models are available in literature [11; 17; 30; 77]. For this study, all these approaches are reviewed and a set of conditional moment closure equations extended to two-phase flows and closure models for the droplet source terms are proposed.

3.3.1 CMC mass fraction equation

Discussions presented here for two-phase flows are done regarding the evaporation of droplets. The derivation can be done following Klimenko's approach [54] or by the decomposition method presented by Bilger [10]. For both derivations the starting point are the continuity equation:

$$\frac{\partial \rho}{\partial t} + \frac{\partial \rho u_j}{\partial x_j} = \rho S \tag{3.31}$$

the instantaneous mass fraction transport equation in conserved form [76]

$$\frac{\partial \rho Y_\alpha}{\partial t} + \frac{\partial \rho u_j Y_\alpha}{\partial x_j} = \frac{\partial}{\partial x_j}\left(\rho D \frac{\partial Y_\alpha}{\partial x_j}\right) + \rho \dot{\omega}_\alpha + \rho S_\alpha \tag{3.32}$$

and the mixture fraction equation, for the gas phase only, in unconserved form:

$$\rho \frac{\partial \xi}{\partial t} + \rho u_j \frac{\partial \xi}{\partial x_j} = \frac{\partial}{\partial x_j}\left(\rho D_\xi \frac{\partial \xi}{\partial x_j}\right) + \rho S - \rho S \xi \tag{3.33}$$

where in (3.32) Y_α is the mass fraction of species α, W_α and S_α are the chemical source term and the evaporation source term of species α, respectively. In Eq. (3.31) and Eq. (3.33) ρS is the evaporation source term. In Eq. (3.33) the last source term on the r.h.s. can be seen as a dilution term in the instantaneous mixture fraction equation occurring from the continuity Eq. (3.31). In the usual context of a single-component liquid fuel and a finite-volume CFD approach for fuel sprays, the evaporation term applies only to the fuel species and can be described as

$$\rho S = \frac{1}{V} \sum_{i=1}^{N} \dot{m}_i \tag{3.34}$$

where V is the volume of the cell, N the number of droplets in the cell, and $\dot{m}_i$ the evaporation rate of the i-th droplet. In Eq. (3.32) we have assumed that all species have equal diffusivities.

Decomposition Method: We follow Bilger's decomposition method and consider a generic mass fraction Y without the subscript α for simplicity. Following the derivation for gaseous CMC presented previously, we can then write

$$Y(x,t) = Q\left[\xi(x,t) = \eta(x,t)\right] + y''(x,t) \tag{3.35}$$

where the reactive scalar is decomposed into a conditional mean and a fluctuation quantity. Implementing Eq. (3.35) in Eq. (3.32), and using

$$\frac{\partial Y}{\partial t} = \frac{\partial Q(\xi)}{\partial t} + \frac{\partial Q(\xi)}{\partial \eta}\frac{\partial \xi}{\partial t} + \frac{\partial y''}{\partial t} \tag{3.36}$$

$$\frac{\partial Y}{\partial x_j} = \frac{\partial Q(\xi)}{\partial x_j} + \frac{\partial Q(\xi)}{\partial \eta}\frac{\partial \xi}{\partial x_j} + \frac{\partial y''}{\partial x_j} \tag{3.37}$$

leads to

$$\begin{aligned}
&\rho\frac{\partial Q}{\partial t} + \frac{\partial Q}{\partial \eta}\rho\frac{\partial \xi}{\partial t} + \rho\frac{\partial y''}{\partial t} + \rho u_j\left(\frac{\partial Q}{\partial x_j} + \frac{\partial Q}{\partial \eta}\frac{\partial \xi}{\partial x_j} + \frac{\partial y''}{\partial x_j}\right)\\
&= \frac{\partial}{\partial x_j}\left(\rho D\frac{\partial Q}{\partial x_j}\right) + \frac{\partial Q}{\partial \eta}\frac{\partial}{\partial x_j}\left(\rho D\frac{\partial \xi}{\partial x_j}\right) + \rho D\frac{\partial \xi}{\partial x_j}\frac{\partial \xi}{\partial x_j}\frac{\partial^2 Q}{\partial \eta^2}\\
&\quad + \rho D\frac{\partial \xi}{\partial x_j}\frac{\partial}{\partial \eta}\left(\frac{\partial Q}{\partial x_j}\right) + \frac{\partial}{\partial x_j}\left(\rho D\frac{\partial y''}{\partial x_j}\right)\\
&\quad + \rho\dot{\omega} + \rho\left(1 - (Q + y'')\right)S
\end{aligned} \tag{3.38}$$

Here term $y''S$ in equation (3.38) is assumed to be small and is neglected as in [76] while in [78] this term is kept. Substituting Eq. (3.33) into Eq. (3.38) and taking the conditional expectations leads to

$$\begin{aligned}
&\bar{\rho}\frac{\partial Q}{\partial t} + \bar{\rho}\langle u_j|\eta\rangle\frac{\partial Q}{\partial x_j} - \bar{\rho}\,\langle N|\eta\rangle\,\frac{\partial^2 Q}{\partial \eta^2} - \frac{\partial}{\partial x_j}\left(\bar{\rho}D\frac{\partial Q}{\partial x_j}\right)\\
&- \left\langle\left(\bar{\rho}D\frac{\partial \xi}{\partial x_j}\frac{\partial}{\partial \eta}\left(\frac{\partial Q}{\partial x_j}\right) + \frac{\partial Q}{\partial \eta}\frac{\partial}{\partial x_j}\left(\bar{\rho}(D - D_\xi)\frac{\partial \xi}{\partial x_j}\right)\right)|\eta\right\rangle\\
&\quad + \left\langle\left(\bar{\rho}\frac{\partial y''}{\partial t} + \bar{\rho}u_j\frac{\partial y''}{\partial x_j} - \frac{\partial}{\partial x_j}\left(\bar{\rho}D\frac{\partial y''}{\partial x_j}\right)\right)|\eta\right\rangle\\
&\quad = \bar{\rho}\langle\dot{\omega}|\eta\rangle + \bar{\rho}\left(\langle S|\eta\rangle - \langle S|\eta\rangle Q - (1-\eta)\langle S|\eta\rangle\frac{\partial Q}{\partial \eta}\right)
\end{aligned} \tag{3.39}$$

Following [10] we can assume

$$\begin{aligned}
&\left\langle\left(\bar{\rho}D\frac{\partial \xi}{\partial x_j}\frac{\partial}{\partial \eta}\left(\frac{\partial Q}{\partial x_j}\right) + \frac{\partial Q}{\partial \eta}\frac{\partial}{\partial x_j}\left(\bar{\rho}(D - D_\xi)\frac{\partial \xi}{\partial x_j}\right)\right)|\eta\right\rangle\\
&\quad + \frac{\partial}{\partial x_j}\left(\bar{\rho}D\frac{\partial Q}{\partial x_j}\right) = 0
\end{aligned} \tag{3.40}$$

$$\left\langle \left(\bar{\rho}\frac{\partial y''}{\partial t} + \bar{\rho}u_j\frac{\partial y''}{\partial x_j} - \frac{\partial}{\partial x_j}\left(\bar{\rho}D\frac{\partial y''}{\partial x_j}\right)\right)|\eta \right\rangle = \frac{\frac{\partial}{\partial x_j}\left[\langle u_j'' y''|\eta\rangle \bar{\rho}\widetilde{P}(\eta)\right]}{\widetilde{P}(\eta)} \tag{3.41}$$

Substitution of Eq. (3.40) and Eq. (3.41) into Eq. (3.39) yields the final version of the conditional mean mass fraction equation

$$\begin{aligned}\frac{\partial Q}{\partial t} + \langle u_j|\eta\rangle\frac{\partial Q}{\partial x_j} = &-\frac{1}{\bar{\rho}\widetilde{P}(\eta)}\frac{\partial}{\partial x_j}\left[\bar{\rho}\widetilde{P}(\eta)\langle u_j'' y''|\eta\rangle\right] \\ &+\langle N|\eta\rangle\frac{\partial^2 Q}{\partial \eta^2} + \langle\dot{\omega}|\eta\rangle \\ &+\langle S|\eta\rangle - \langle S|\eta\rangle Q - (1-\eta)\langle S|\eta\rangle\frac{\partial Q}{\partial \eta}\end{aligned} \tag{3.42}$$

where the last three terms on the r.h.s. are due to droplet evaporation. The conditional droplet source term can be described by:

$$\langle S|\eta\rangle = \left\langle \left(\frac{1}{\rho V}\sum_{i=1}^{N}\dot{m}_i\right)|\eta\right\rangle \tag{3.43}$$

To conclude, the first droplet source term occurs from the instantaneous mass fraction equation and the second from the continuity equation. The last one has its origins in the mixture fraction and also continuity equation. Equation (3.42) can also be derived with Klimenko's approach as shown in [54]. Mortensen and Bilger [78], by starting from Kataoka's two-fluid formulation, derived a similar equation which includes the volume fraction of the liquid phase. In the limit of a dilute spray, as in most regions of a gas turbine combustor, the resulting equation is identical to equation (3.42).

3.3.2 CMC energy equation

The conditional energy equation in terms of temperature can be derived in a similar manner, assuming equal diffusivity and $Le = 1$ so that $\lambda = c_p D\rho$ where λ is the

thermal conductivity. Starting with the instantaneous temperature equation

$$c_p\frac{\partial \rho T}{\partial t}+c_p\frac{\partial \rho u_j T}{\partial x_j}=\frac{\partial p}{\partial t}+\frac{\partial}{\partial x_j}\left(\lambda\frac{\partial T}{\partial x_j}\right)-\rho\dot{\omega}_R \\ -\rho D\frac{\partial T}{\partial x_j}\sum_{\alpha=1}^{n}c_{p,\alpha}\frac{\partial Y_\alpha}{\partial x_j}-\rho\dot{\omega}_H+S_E \tag{3.44}$$

where $c_{p,\alpha}$ is the specific heat capacity of species α, ω_H and ω_R are the chemical reaction term of enthalpy and a radiation loss, respectively. S_E is an additional sink term due to the droplet evaporation described by

$$S_E=-\rho S h_{fg} \tag{3.45}$$

where h_{fg} is the latent heat of evaporation. Following Bilger's decomposition method

$$T(x,t)=Q_T\left[\xi(x,t)=\eta(x,t)\right]+T''(x,t) \tag{3.46}$$

and using Eq. (3.36) and Eq. (3.37) into Eq. (3.44) gives

$$\rho c_p\frac{\partial Q_T}{\partial t}+\rho c_p\frac{\partial T''}{\partial t}+\rho c_p u_j\frac{\partial Q_T}{\partial x_j}+\rho c_p u_j\frac{\partial T''}{\partial x_j} \\ -\frac{\partial}{\partial x_j}\left(\lambda\frac{\partial Q_T}{\partial x_j}\right)-\lambda\left(\frac{\partial \xi}{\partial x_j}\right)^2\frac{\partial^2 Q_T}{\partial \eta^2}-\lambda\frac{\partial \xi}{\partial x_j}\frac{\partial}{\partial x_j}\left(\frac{\partial Q_T}{\partial \eta}\right)-\frac{\partial}{\partial x_j}\left(\lambda\frac{\partial T''}{\partial x_j}\right) \\ +\frac{\partial Q_T}{\partial \eta}\left(\rho c_p\frac{\partial \xi}{\partial t}+\rho c_p u_j\frac{\partial \xi}{\partial x_j}-\frac{\partial}{\partial x_j}\left(\lambda\frac{\partial \xi}{\partial x_j}\right)\right) \\ =\frac{\partial p}{\partial t}-\rho\dot{\omega}_H-\rho\dot{\omega}_R-\rho S h_{fg}-\rho c_p S(Q_T+T'') \\ -\sum_{\alpha=1}^{n}\rho c_{p,\alpha}D\left(\frac{\partial Q_\alpha}{\partial x_j}+\frac{\partial Q_\alpha}{\partial \eta}\frac{\partial \xi}{\partial x_j}+\frac{\partial y''_\alpha}{\partial x_j}\right)\cdot\left(\frac{\partial Q_T}{\partial x_j}+\frac{\partial Q_T}{\partial \eta}\frac{\partial \xi}{\partial x_j}+\frac{\partial T''}{\partial x_j}\right) \tag{3.47}$$

The term ST'' in Eq. (3.47) is assumed to be very small and hence neglected. Since $Le=1$ and assuming equal diffusivities we can say

$$\frac{\partial}{\partial x_j}\left(\lambda\frac{\partial \xi}{\partial x_j}\right)=\frac{\partial}{\partial x_j}\left(\rho c_p D\frac{\partial \xi}{\partial x_j}\right)=c_p\frac{\partial}{\partial x_j}\left(\rho D\frac{\partial \xi}{\partial x_j}\right)+\rho D\frac{\partial \xi}{\partial x_j}\frac{\partial c_p}{\partial x_j} \tag{3.48}$$

and using the decomposition method on c_p and using Eq. (3.58) with taking the conditional expectation of Eq. (3.47) conditional on $\xi(x,t) = \eta$ gives

$$\begin{aligned}
&c_{p_\eta}\frac{\partial Q_T}{\partial t} + c_{p_\eta}\langle u_j|\eta\rangle\frac{\partial Q_T}{\partial x_j} - c_{p_\eta}\langle N|\eta\rangle\frac{\partial^2 Q_T}{\partial \eta^2} \\
&-\langle N|\eta\rangle\left(\frac{\partial c_p}{\partial \eta}\frac{\partial Q_T}{\partial \eta} + \sum_{\alpha=1}^{n} c_{p,\alpha_\eta}\frac{\partial Q_\alpha}{\partial \eta}\frac{\partial Q_T}{\partial \eta}\right) \\
&= \left\langle \frac{1}{\rho}\frac{\partial p}{\partial t}|\eta \right\rangle - \langle \omega_H|\eta\rangle - \langle \omega_R|\eta\rangle + e_{Q_T} + e_T + e_{c_p} \\
&-h_{fg}\langle S|\eta\rangle - c_{p_\eta}Q_T\langle S|\eta\rangle - c_{p_\eta}\langle S|\eta\rangle\,(1-\eta)\,\frac{\partial Q_T}{\partial \eta}
\end{aligned} \tag{3.49}$$

where $c_{p_\eta} = \langle c_p|\eta\rangle$ and

$$e_{Q_T} = \left\langle \frac{\partial}{\partial x_j}\left(c_p D\frac{\partial Q_T}{\partial x_j}\right) + c_p D\frac{\partial \xi}{\partial x_j}\frac{\partial}{\partial x_j}\left(\frac{\partial Q_T}{\partial \eta}\right)|\eta \right\rangle \tag{3.50}$$

$$e_T = -\left\langle c_p\frac{\partial T''}{\partial t} + c_p u_j\frac{\partial T''}{\partial x_j} - \frac{\partial}{\partial x_j}\left(c_p D\frac{\partial T''}{\partial x_j}\right)|\eta \right\rangle \tag{3.51}$$

$$\begin{aligned}
e_{c_p} = \langle N''\sum_{\alpha=1}^{n} c''_{p,\alpha}\frac{\partial Q_\alpha}{\partial \eta}\frac{\partial Q_T}{\partial \eta} + \frac{\partial Q_T}{\partial \eta}D\frac{\partial \xi}{\partial x_j}\left(\frac{\partial c_{p_\eta}}{\partial x_j} + \frac{\partial c''_p}{\partial x_j}\right) \\
+D\sum_{\alpha=1}^{n} c_{p,\alpha}\left(\frac{\partial Q_\alpha}{\partial x_j} + \frac{\partial y''_\alpha}{\partial x_j}\right)\frac{\partial \xi}{\partial x_j}\frac{\partial Q_T}{\partial \eta} \\
+D\sum_{\alpha=1}^{n} c_{p,\alpha}\frac{\partial Q_\alpha}{\partial \eta}\frac{\partial \xi}{\partial x_j}\left(\frac{\partial Q_T}{\partial x_j} + \frac{\partial T''}{\partial x_j}\right) \\
+D\sum_{\alpha=1}^{n} c_{p,\alpha}\left(\frac{\partial Q_\alpha}{\partial x_j} + \frac{\partial y''_\alpha}{\partial x_j}\right)\left(\frac{\partial Q_T}{\partial x_j} + \frac{\partial T''}{\partial x_j}\right)|\eta\rangle
\end{aligned} \tag{3.52}$$

In Eq. (3.49) the last three terms on the r.h.s. are due to evaporation, where the first term appears directly out of the instantaneous temperature equation Eq. (3.44), the second and third from Eq. (3.33) and Eq. (3.31). Assuming high Reynolds number, the term e_{Q_T} can be neglected. With the assumption that c''_p can be neglected the term

e_T can be closed as

$$e_T = -\frac{c_{p_\eta}}{\bar{\rho}\tilde{P}(\eta)}\frac{\partial}{\partial x_j}\left(\bar{\rho}\tilde{P}(\eta)\langle u_j''T''|\eta\rangle\right) \tag{3.53}$$

Here term e_{c_p} is neglected, however following the the rescaling arguments proposed in [54] this term should not be neglected for high Reynolds number. Since the error of setting $e_{c_p} = 0$ is not known further analysis is necessary [79]. Using all assumptions, the final form of the conditional energy equation is:

$$\begin{aligned}\frac{\partial Q_T}{\partial t} + \langle u_j|\eta\rangle\frac{\partial Q_T}{\partial x_j} &= -\frac{1}{\bar{\rho}\tilde{P}(\eta)}\frac{\partial}{\partial x_j}\left[\bar{\rho}\tilde{P}(\eta)\langle u_j''T''|\eta\rangle\right] \\ +\langle N|\eta\rangle\left[\frac{1}{c_{p_\eta}}\left(\frac{\partial c_{p_\eta}}{\partial\eta} + \sum_{\alpha=1}^{n} c_{p,\alpha_\eta}\frac{\partial Q_\alpha}{\partial\eta}\right)\frac{\partial Q_T}{\partial\eta} + \frac{\partial^2 Q_T}{\partial\eta^2}\right] \\ +\frac{1}{c_{p_\eta}}\left\langle\frac{1}{\rho}\frac{\partial p}{\partial t}|\eta\right\rangle - \frac{1}{c_{p_\eta}}\langle\dot{\omega}_H|\eta\rangle - \frac{1}{c_{p_\eta}}\langle\dot{\omega}_R|\eta\rangle \\ -\frac{h_{fg}}{c_{p_\eta}}\langle S|\eta\rangle - Q_T\langle S|\eta\rangle - \langle S|\eta\rangle\,(1-\eta)\,\frac{\partial Q_T}{\partial\eta}\end{aligned} \tag{3.54}$$

Alternatively the CMC energy equation for two-phase flows can be similarly derived as above, starting from the instantaneous enthalpy equation

$$\frac{\partial\rho h}{\partial t} + \frac{\partial\rho u_j h}{\partial x_j} = \frac{\partial p}{\partial t} + \frac{\partial}{\partial x_j}\left(\rho D\frac{\partial h}{\partial x_j}\right) - \rho\omega_R + S_E \tag{3.55}$$

Applying the derivations steps as before leads to

$$\begin{aligned}\frac{\partial Q_h}{\partial t} + \langle u_j|\eta\rangle\frac{\partial Q_h}{\partial x_j} &= -\frac{1}{\bar{\rho}\tilde{P}(\eta)}\frac{\partial}{\partial x_j}\left[\bar{\rho}\tilde{P}(\eta)\langle u_j''h''|\eta\rangle\right] \\ &+\left\langle\frac{1}{\rho}\frac{\partial p}{\partial t}|\eta\right\rangle + \langle N|\eta\rangle\frac{\partial^2 Q_h}{\partial\eta^2} - \langle\omega_R|\eta\rangle \\ &-h_{fg}\langle S|\eta\rangle - \langle S|\eta\rangle Q_h - (1-\eta)\langle S|\eta\rangle\frac{\partial Q_h}{\partial\eta}\end{aligned} \tag{3.56}$$

3.3.3 PDF of mixture fraction

In Eq. (3.54) and Eq. (3.56) $P(\eta)$ is the probability density function of η. By using the conserved form of Eq. (3.33) and following the method developed by [80], an equation for the PDF of η [76] can be established

$$\frac{\partial\langle\rho|\eta\rangle P(\eta)}{\partial t}+\frac{\partial\langle\rho|\eta\rangle\langle u_j|\eta\rangle P(\eta)}{\partial x_j}=-\frac{\partial^2}{\partial\eta^2}\left(\langle\rho|\eta\rangle\langle N|\eta\rangle P(\eta)\right) \\ -\frac{\partial}{\partial\eta}\left[\langle\rho|\eta\rangle\langle(1-\eta)S|\eta\rangle P(\eta)\right]+\langle\rho|\eta\rangle\langle S|\eta\rangle P(\eta) \tag{3.57}$$

Equation (3.57) contains the usual gaseous terms plus two new terms induced by droplet vaporization. To solve this equation a Monte Carlo method can be used, leading to moderate computational costs since no chemistry is to consider. A more practical way forward is to presume the shape of $P(\eta)$.

For the presumed pdf approach the mean and the variance of mixture fraction has to be solved. Both variables are influenced by the evaporation of the droplets in two-phase flows. The mean mixture fraction transport equation based on Eq. (3.33) can be written as

$$\frac{\partial\bar{\rho}\widetilde{\xi}}{\partial t}+\frac{\partial\bar{\rho}\widetilde{u}_j\widetilde{\xi}}{\partial x_j}=\frac{\partial}{\partial x_j}\left(\bar{\rho}D\frac{\partial\widetilde{\xi}}{\partial x_j}\right)-\frac{\partial}{\partial x_j}\left(\bar{\rho}(\widetilde{u_j\xi}-\widetilde{u}_j\widetilde{\xi})\right)+\bar{\rho}\widetilde{S} \tag{3.58}$$

The derivation of the variance of the mixture fraction $\widetilde{\xi''^2}$ can be found in [11; 30; 81]. A transport equation for $\widetilde{\xi}^2$ and $\widetilde{\xi}^2$ is derived to fulfill:

$$\frac{\partial\bar{\rho}\widetilde{\xi''^2}}{\partial t}=\frac{\partial\bar{\rho}\widetilde{\xi}^2}{\partial t}-\frac{\partial\bar{\rho}\tilde{\xi}^2}{\partial t} \tag{3.59}$$

To get $\tilde{\xi}^2$ we start with (3.58)$*2\tilde{\xi}$ and get

$$2\tilde{\xi}^2\frac{\partial\bar{\rho}}{\partial t}+2\tilde{\xi}\bar{\rho}\frac{\partial\tilde{\xi}}{\partial t}+2\tilde{\xi}^2\frac{\partial\bar{\rho}\widetilde{u}_j}{\partial x_j}+2\tilde{\xi}\bar{\rho}\widetilde{u}_j\frac{\partial\tilde{\xi}}{\partial x_j}=2\tilde{\xi}\frac{\partial}{\partial x_j}\left(\bar{\rho}D\frac{\partial\tilde{\xi}}{\partial x_j}\right) \\ -2\tilde{\xi}\frac{\partial}{\partial x_j}\left(\bar{\rho}\widetilde{u_j\xi}-\bar{\rho}\widetilde{u}_j\tilde{\xi}\right)+2\tilde{\xi}\bar{\rho}\widetilde{S} \tag{3.60}$$

then substituting the Favre averaged version of Eq. (3.58) in conserved form in the left hand side of Eq. (3.60) leads to

$$\frac{\partial\bar{\rho}\tilde{\xi}^2}{\partial t}+\frac{\partial\bar{\rho}\widetilde{u}_j\tilde{\xi}^2}{\partial x_j}+\tilde{\xi}^2\bar{\rho}\widetilde{S}=\frac{\partial}{\partial x_j}\left(\bar{\rho}D\frac{\partial\tilde{\xi}^2}{\partial x_j}\right)-2\bar{\rho}D\frac{\partial\tilde{\xi}}{\partial x_j}\frac{\partial\tilde{\xi}}{\partial x_j}$$
$$-2\frac{\partial\tilde{\xi}}{\partial x_j}\left(\bar{\rho}\widetilde{u_j\xi}-\bar{\rho}\widetilde{u}_j\tilde{\xi}\right)+2\tilde{\xi}\bar{\rho}\widetilde{S} \tag{3.61}$$

On the left hand side of (3.61) an additional droplet source term emerges from the continuity Eq. (3.31). For the derivation of $\widetilde{\xi^2}$ we start with Eq. (3.33)$*2\xi$ which leads to

$$2\xi\rho\frac{\partial\xi}{\partial t}+2\xi^2\frac{\partial\rho}{\partial t}+2\xi^2\frac{\partial u_j}{\partial x_j}+2\xi\rho u_j\frac{\partial\xi}{\partial x_j}=2\xi\frac{\partial}{\partial x_j}\left(\rho D\frac{\partial\xi}{\partial x_j}\right)+2\xi\rho S \tag{3.62}$$

again substituting Eq. (3.31) into the left hand side of Eq. (3.62) and then Favre averaging yields

$$\frac{\partial\bar{\rho}\widetilde{\xi^2}}{\partial t}+\frac{\partial\bar{\rho}\widetilde{u}_j\widetilde{\xi^2}}{\partial x_j}+\bar{\rho}\widetilde{S\xi^2}=\frac{\partial}{\partial x_j}\left(\bar{\rho}D\frac{\partial\widetilde{\xi^2}}{\partial x_j}\right)-2\bar{\rho}D\widetilde{\frac{\partial\xi}{\partial x_j}\frac{\partial\xi}{\partial x_j}}+2\bar{\rho}\widetilde{\xi S} \tag{3.63}$$

As before an additional droplet source term occurs on the left hand side originating from the continuity equation. Substituting both (3.61) and (3.63) into (3.59) leads to a transport equation for $\widetilde{\xi''^2}$

$$\frac{\partial\bar{\rho}\widetilde{\xi''^2}}{\partial t}+\frac{\partial\bar{\rho}\widetilde{u}_j\widetilde{\xi''^2}}{\partial x_j}=\frac{\partial}{\partial x_j}\left[\bar{\rho}(D+D_t)\frac{\partial\widetilde{\xi''^2}}{\partial x_j}\right]-\bar{\rho}\widetilde{\chi}$$
$$+2D_t\frac{\partial\widetilde{\xi}}{\partial x_j}\frac{\partial\widetilde{\xi}}{\partial x_j}+\bar{\rho}S_\xi \tag{3.64}$$

where term S_ξ is due to droplet evaporation

$$S_\xi=2\left(\widetilde{\xi S}-\widetilde{\xi}\widetilde{S}\right)-\left(\widetilde{\xi^2 S}-\tilde{\xi}^2\widetilde{S}\right) \tag{3.65}$$

and

$$\bar{\rho}\tilde{\chi}=2\bar{\rho}D\widetilde{\frac{\partial\xi}{\partial x_j}\frac{\partial\xi}{\partial x_j}} \tag{3.66}$$

Saturation mixture fraction ξ_s: Since in the physical picture of the process, evaporation occurs at the droplet surface that has a concentration corresponding to the saturation value, the mixture fraction at the droplet surface will be ξ_s, where the subscript s denotes saturation. It is conceivable that every droplet in volume V will have a different ξ_s. The correlations between ξ and S in Eq. (3.65) can hence be expressed as [11; 81]

$$\widetilde{\xi S} = \widetilde{\xi_s S} \tag{3.67}$$

$$\widetilde{\xi^2 S} = \widetilde{\xi_s^2 S} \tag{3.68}$$

which in the usual context of the spray trajectory approach become:

$$\bar{\rho}\widetilde{\xi_s S} = \frac{1}{V}\sum_{i=1}^{N} \xi_{s,i}\dot{m}_i \tag{3.69}$$

$$\bar{\rho}\widetilde{\xi_s^2 S} = \frac{1}{V}\sum_{i=1}^{N} \xi_{s,i}^2\dot{m}_i \tag{3.70}$$

If ξ_s is constant, S_ξ can be written as [78]

$$S_\xi = 2\left(\xi_s - \widetilde{\xi}\right)\left(1 - \widetilde{\xi}\right)\widetilde{S} - \left(\xi_s - \widetilde{\xi}\right)^2 \widetilde{S} \tag{3.71}$$

S can still depend weakly on ξ through $\dot{m}$ in Eq. (3.69), since the rate of evaporation will depend on how much vapor is existing around the droplet. To avoid the difficulty of having to consider ξ_s of every droplet, in [11] an equation for $\overline{\xi_s}$ is derived, by using the gradient diffusion hypothesis and neglecting molecular transport

$$\frac{\partial \bar{\rho}\widetilde{\xi}\widetilde{\xi_s}}{\partial t} + \frac{\partial \bar{\rho}\widetilde{u}_j\widetilde{\xi}\widetilde{\xi_s}}{\partial x_j} = \frac{\partial}{\partial x_j}\left(\bar{\rho}D_t\frac{\partial \widetilde{\xi}\widetilde{\xi_s}}{\partial x_j}\right) + \bar{\rho}\overline{\xi_s S} \tag{3.72}$$

where the last term can come from the model of Eq. (3.69).
$\widetilde{S}$ in Eq. (3.65) is

$$\widetilde{S} = \frac{1}{\bar{\rho}V}\sum_{i=1}^{N} \dot{m}_i \tag{3.73}$$

With the introduction of the saturation mixture fraction ξ_s above the conditional droplet evaporation source term $\langle S|\eta\rangle$ defined in Eq. (3.43) is now

$$\langle S|\eta\rangle = \langle S|\xi_s\rangle\delta(\eta-\xi_S) = \frac{\tilde{S}}{P(\xi_s)} \tag{3.74}$$

3.3.4 Summary of closed governing equations

The final equations, which will be used in Chapter 6, are presented here in this section to give an compact overview.

The conditional mass fraction equation for two-phase flows using the closure assumptions presented previously:

$$\begin{aligned}\frac{\partial Q}{\partial t}+\left(\tilde{u}_j-\frac{D_t(\eta-\tilde{\xi})}{\widetilde{\xi''^2}}\frac{\partial\tilde{\xi}}{\partial x_j}\right)\frac{\partial Q}{\partial x_j} &= \frac{1}{\bar{\rho}\widetilde{P}(\eta)}\frac{\partial}{\partial x_j}\left[\bar{\rho}\widetilde{P}(\eta)D_t\frac{\partial Q}{\partial x_j}\right]\\ &\quad+\langle N|\eta\rangle\frac{\partial^2 Q}{\partial\eta^2}+\langle\dot{\omega}|\eta\rangle\\ &\quad+\langle S|\eta\rangle-Q\langle S|\eta\rangle-(1-\eta)\langle S|\eta\rangle\frac{\partial Q}{\partial\eta}\end{aligned} \tag{3.75}$$

The conditional temperature equation for two-phase flows:

$$\begin{aligned}\frac{\partial Q_T}{\partial t}+\left(\tilde{u}_j-\frac{D_t(\eta-\tilde{\xi})}{\widetilde{\xi''^2}}\frac{\partial\tilde{\xi}}{\partial x_j}\right)\frac{\partial Q_T}{\partial x_j} &= \frac{1}{\bar{\rho}\tilde{P}(\eta)}\frac{\partial}{\partial x_j}\left[\bar{\rho}\tilde{P}(\eta)D_t\frac{\partial Q_T}{\partial x_j}\right]\\ &\quad+\langle N|\eta\rangle\left[\frac{1}{c_{p_\eta}}\left(\frac{\partial c_{p_\eta}}{\partial\eta}+\sum_{\alpha=1}^{n}c_{p,\alpha_\eta}\frac{\partial Q_\alpha}{\partial\eta}\right)\frac{\partial Q_T}{\partial\eta}+\frac{\partial^2 Q_T}{\partial\eta^2}\right]\\ &\quad+\frac{1}{c_{p_\eta}}\left\langle\frac{1}{\rho}\frac{\partial p}{\partial t}|\eta\right\rangle-\frac{1}{c_{p_\eta}}\sum_{\alpha=1}^{n}h_\alpha\langle\dot{\omega}_\alpha|\eta\rangle-\frac{\langle\dot{\omega}_R|\eta\rangle}{c_{p_\eta}}\\ &\quad-\frac{h_{fg}}{c_{p_\eta}}\langle S|\eta\rangle-Q_T\langle S|\eta\rangle-(1-\eta)\langle S|\eta\rangle\frac{\partial Q_T}{\partial\eta}\end{aligned} \tag{3.76}$$

The PDF of mixture fraction is solved by a presumed PDF approach as presented above, using the mean and variance of mixture fraction:

$$\frac{\partial \bar{\rho}\widetilde{\xi}}{\partial t} + \frac{\partial \bar{\rho}\widetilde{u}_j\widetilde{\xi}}{\partial t} = \frac{\partial}{\partial x_i}\left(\bar{\rho}(D+D_t)\frac{\partial \widetilde{\xi}}{\partial x_i}\right) + \bar{\rho}\widetilde{S} \tag{3.77}$$

$$\frac{\partial \bar{\rho}\widetilde{\xi''^2}}{\partial t} + \frac{\partial \bar{\rho}\widetilde{u}_j\widetilde{\xi''^2}}{\partial x_j} = \frac{\partial}{\partial x_j}\left[\bar{\rho}(D+D_t)\frac{\partial \widetilde{\xi''^2}}{\partial x_j}\right] - \bar{\rho}\widetilde{\chi} + 2D_t\frac{\partial \widetilde{\xi}}{\partial x_j}\frac{\partial \widetilde{\xi}}{\partial x_j} + \bar{\rho}S_\xi \tag{3.78}$$

where the droplet source term $\bar{\rho}S_\xi$ is closed by introducing the saturation mixture fraction on the droplet surface ξ_s, so that

$$\bar{\rho}S_\xi = 2\left(\xi_s - \widetilde{\xi}\right)\left(1-\widetilde{\xi}\right)\bar{\rho}\widetilde{S} - \left(\xi_s - \widetilde{\xi}\right)^2\bar{\rho}\widetilde{S} \tag{3.79}$$

$\tilde{S}$ can be found from

$$\widetilde{S} = \frac{1}{\bar{\rho}V}\sum_{i=1}^{N}\dot{m}_i \tag{3.80}$$

With the introduction of the saturation mixture fraction ξ_s above the conditional droplet evaporation source term $\langle S|\eta\rangle$ defined in Eq. (3.43) is now

$$\langle S|\eta\rangle = \langle S|\xi_s\rangle\delta(\eta-\xi_s) = \frac{\tilde{S}}{P(\xi_s)} \tag{3.81}$$

Chapter 4

Direct Numerical Simulations of Autoignition in Turbulent Two-phase Flows

4.1 Objective

Three-dimensional direct numerical simulations (DNS) were carried out for validation purposes of the CMC model for two-phase flows presented in Chapter 3. These calculations offer the possibility to investigate further autoignition under the presence of droplet vaporization. Of interest are the impact of evaporation of droplets on the autoignition process under decaying turbulence. The droplets were taken as point sources and were tracked in a Lagrangian manner. In addition it will be investigated if a specific mixture fraction ξ_{MR} can be found where the highest reaction rates always occur, as in purely gaseous flows [12]. The data will provide needed information for the validation of the CMC model presented in Chapter 3.

4.2 Spray autoignition

Autoignition describes an non-stationary process of a combustible mixture undergoing chemical reactions which leads to a rapid release of heat which subsequently es-

tablishes a flame kernel [82]. This process, also called in the literature *spontaneous ignition* or *self-ignition* [48], differs from forced ignition by the lack of any external energy source such as a spark or a flame. Homogeneous autoignition is found in combustion devices where fuel and air are premixed and can occur as a desired process or an undesired side effect. The best known combustion device which uses the autoignition process is the diesel engine, where autoignition takes place after fuel and oxidizer are partially premixed in the cylinder and compressed by an upwards moving piston. Inhomogeneous autoignition occurs when fuel and oxidizer are initially separated and then mix and react simultaneously. Spray autoignition investigated in this chapter is an inhomogeneous autoignition system since the fuel is initially injected in liquid form into the gaseous oxidizer. The liquid fuel starts to evaporate and provides gaseous fuel to mix with the oxidizer.

Understanding the influence of the evaporation process on autoignition of turbulent fuel sprays is relevant to the development of a range of combustion devices. Direct numerical simulations (DNS) allow detailed insight into the interactions between droplet evaporation, mixing and autoignition and are pursued in this paper to identify some details of autoignition sites in sprays. Following the common approach to consider the droplets as point sources of mass, energy and momentum [30; 83], Wang and Rutland [35] performed two-dimensional DNS to study the effect of temperature and equivalence ratio on the ignition of a fuel spray in isotropic decaying turbulence with a detailed reaction mechanism, while a similar study in 2-D with one-step chemistry [17] focused on the droplet evaporation and its effects on the mixture fraction. The autoignition of droplet-laden transitional jets was also examined [36]. In these studies, the location of autoignition was not discussed in depth, although it was evident that some structure in mixture fraction space exists.

In the current study, 3-D DNS are performed to address several aspects of autoignition that were found in previous studies for purely gaseous flows. 2-D DNS with one-step chemistry [12] showed the existence of a specific value of mixture fraction ξ_{MR}, called "most reactive" mixture fraction, where autoignition is most likely to occur. This finding was confirmed and extended using 3-D DNS [23] or detailed kinetics [18; 19]. The present study investigates whether similar concepts stand under

the influence of evaporation. Since the existence of a preferred mixture fraction for autoignition is not a strong function of the chemistry (although its value may be), and especially since the previous droplet autoignition DNS have only been performed in 2-D, this work is limited to simplified chemistry but emphasizes a proper turbulent flow. Note that despite the use of detailed chemistry in Refs. [35; 36], high air temperatures were used that implies that the chemistry behaved in an Arrhenius way and hence the advantages of implementing a detailed scheme (for example, capturing the possibility of negative dependence of ignition time on temperature) have probably not affected the autoignition process and how it interacts with the turbulence. For revealing these interactions, a one-step model may be sufficient, an approach also followed in Ref. [17].

Examining the evolution of temperature in mixture fraction space in autoigniting two-phase systems can provide valuable information for validating models such as the Conditional Moment Closure or flamelet models that are used for diesel engines [74; 79]. In such models, additional closures for the mixture fraction variance equation and for the mean scalar dissipation rate are needed [11; 17; 30; 77], which, in principle, cannot be validated using the point-source approach followed in the above DNS (and in this thesis) due to lack of resolution in the immediate neighbourhood of each droplet [78]. Hence, the DNS shown here may be thought of as implementing a sub-grid averaging, which renders some of the extracted quantities prone to uncertainty.

4.3 DNS of autoignition of droplets in hot surrounding

4.3.1 Setup

The gas phase equations correspond to a fully-compressible formulation and assume a constant gaseous specific heat capacity $C_{p,g}$ and transport properties and uses unity Lewis number Le. All governing equations can be found in Section 2.2.2. The SENGA DNS code is used [84], extended to two-phase flows. A single-step reaction with the stoichiometry of n-heptane, giving a stoichiometric mixture fraction $\xi_{st} = 0.062$, was used. The fuel consumption rate is calculated by an Arrhenius-type expression similar to [25]. A uniform 128^3 grid was used to discretize a cube of length L.

Droplets were randomly distributed in a rectangular layer between $(x/L)_{left} = 0.25$ and $(x/L)_{right} = 0.75$, as shown in Fig. 4.1. An initial turbulent velocity field was generated within the whole cube, which was then decaying in time.

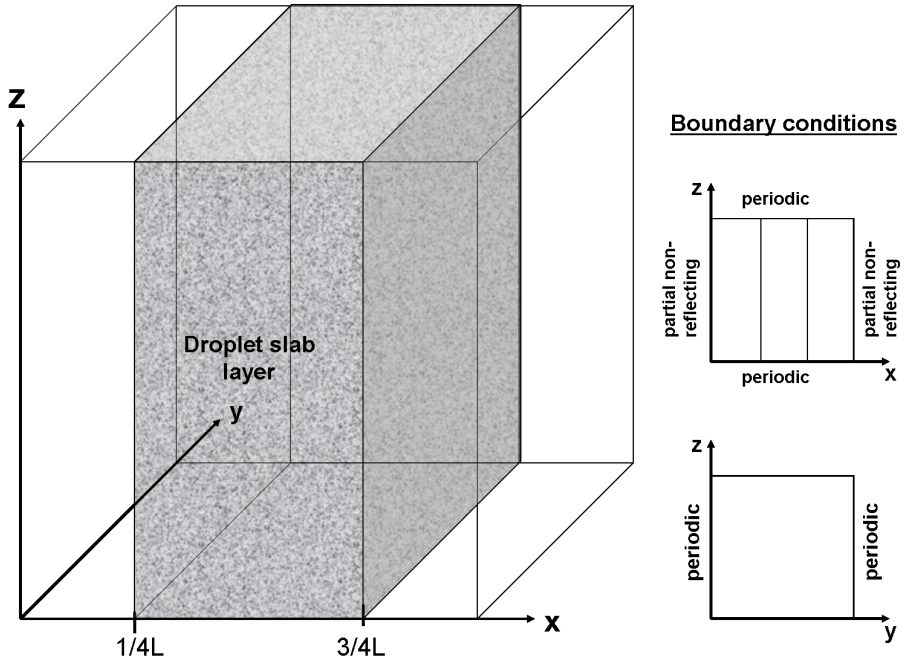

Figure 4.1: Flow arrangement.

The initial integral length scale $L_{turb} = 0.14L$. Table 6.1 shows the parameters used. Three initial droplet diameters Θ_0 were simulated. The total number of droplets was selected to give a global equivalence ratio of $\phi = 2.0$ in the droplet-laden layer, with initially all fuel in liquid form. Outside the droplet layer there is only air. The initial non-dimensional temperature for the gas phase was $T_O = 0.5$ and for the fuel droplets $T_F = 0$.

Non-dimensional temperatures are calculated by $T = (\hat{T} - T_0)/(T_{ad} - T_0)$ where $\hat{T}$ is the dimensional temperature in $[K]$, T_0 the dimensional temperature at $292K$ and T_{ad} is the adiabatic flame temperature at stoichiometry of n-heptane.

For reference purposes, autoignition of stagnant adiabatic homogeneous mixtures

Table 4.1: List of parameters for the DNS. Θ_0 is the initial droplet diameter, τ_{ign} the autoignition time, τ_{turb} the large-eddy turbulent time scale, τ_{ref} the minimum autoignition time for the reference case (Fig.4.2). n is the total number of droplets per unit volume, Re_t is the turbulent Reynolds number and η_K is the non-dimesionalized Kolmogorov length scale. St is the Stokes number calculated by $St = \tau_d/\tau_K$, where $\tau_K = (\nu/\epsilon)^{1/2}$ is the Kolmogorov time scale. For the evaporation time τ_{vap} without combustion, droplets are assumed to be completely evaporated when $\Theta = 0.1\Theta_0$.

Case	Θ_0 $[\mu m]$	n	Re_t	$\frac{n^{-1/3}}{\eta_K}$	St	$\frac{\tau_{turb}}{\tau_{ref}}$	$\frac{\tau_{vap}}{\tau_{ref}}$	$\frac{\tau_{turb}}{\tau_{vap}}$	$\frac{\tau_{ign}}{\tau_{ref}}$
$CL1$	20	25592	33.6	2.23	0.0070	12.88	11.52	1.12	2.156
$C01$	20	25592	106.2	4.22	0.0095	4.076	11.52	0.35	2.208
$C02$	25	13103	106.2	5.28	0.0150	4.076	18.68	0.22	2.430
$C03$	30	7583	106.2	6.33	0.0210	4.076	29.69	0.14	2.668

without droplets was examined. In these simulations, the initial temperature and mass fractions were given by inert mixing and were hence linear functions of the mixture fraction. Autoignition times are presented in the inset of Fig. 4.2. Similar to [12], the shortest autoignition time in mixture fraction space is used to define the reference autoignition time τ_{ref}, which can be understood as the characteristic timescale of an autoigniting inhomogeneous system. The "most reactive" mixture fraction, ξ_{MR} can also be defined from this graph as about 0.10. Our aim is to examine whether evaporation and subsequent mixing differentiates the autoignition time from τ_{ref} and the ignition mixture fraction from ξ_{MR}.

4.3.2 General evolution

The volume-averaged temperature is shown in Fig. 4.2 *vs.* time. A mild temperature depression is evident at early times due to evaporation, which is largest for the smallest diameter case. At some point, the temperature rises quickly, which is associated with autoignition of the evaporated fuel. Some more details of the flow are visualised by contour plots in the droplet-containing region of the instantaneous temperature T, reaction rate ω, mixture fraction ξ, and scalar dissipation rate N (Fig. 4.3), across planes normal to the z-axis, obtained before and after autoignition for case $CL1$, taken

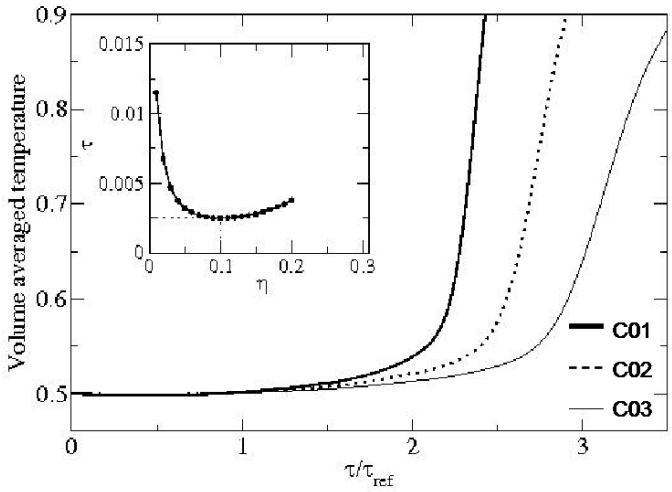

Figure 4.2: Volume averaged temperature against time. Inset shows autoignition times of homogeneous, adiabatic, stagnant mixtures as a function of mixture fraction with initial species mass fractions and temperature determined from inert mixing with $T_O = 0.5$ and $T_F = 0$, which is used to determine τ_{ref}.

as characteristic for all Θ_0. At early times, the evaporation becomes noticeable in developing $\xi > 0$ and temperature spots below the initial value. The mixture fraction fluctuations here seem to occur at the scale of the inter-droplet spacing. As evaporation proceeds, ξ increases and its structure is affected by mixing and the turbulent motions. Later, several independent ignition kernels (high temperature spots) occur, corresponding to approximately $\xi = 0.09$.

After autoignition, the reaction zones surround the high-temperature regions with the reaction rate in the middle of the spot decaying to zero, since one of the reactants (the oxidiser, since the ignition ξ is higher than ξ_{st}) in the initial spots has been consumed. The mixture fraction in the ignited region keeps increasing due to the enhanced evaporation at the high combustion temperatures.

Figure 4.4 shows scatter plots of T against the cell mixture fraction (η denotes the sample-space variable corresponding to ξ), using data from the whole domain. Before autoignition, a mild temperature increment over the inert (mixing) line is evident, with noticeable scatter of the data at the same η. The evaporation has become evident by

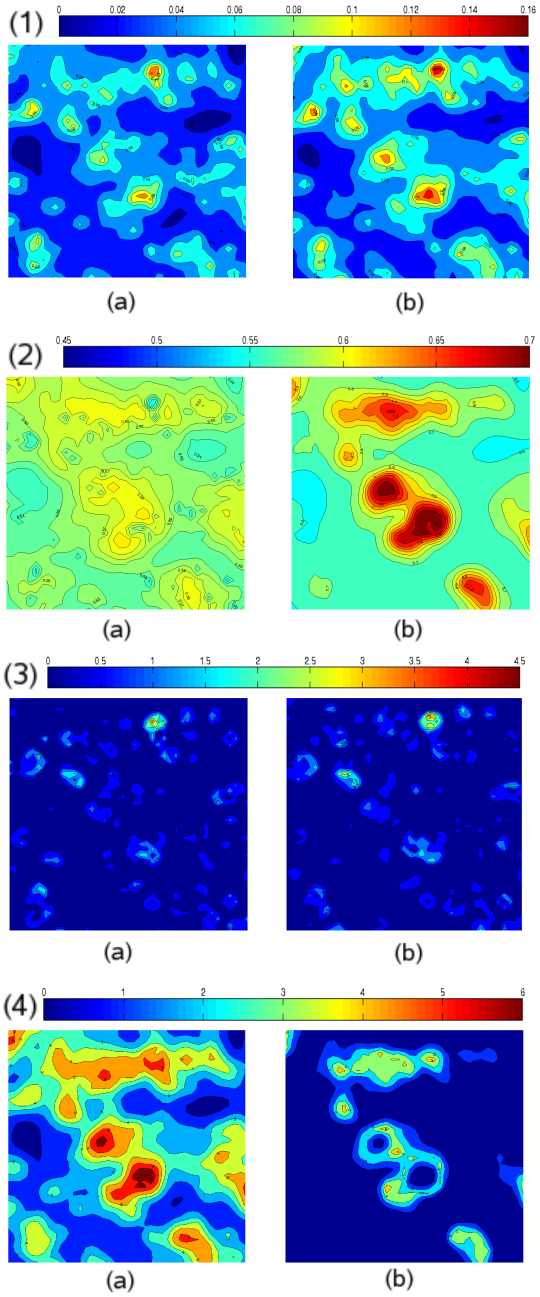

Figure 4.3: Mixture fraction (1), temperature (2), scalar dissipation rate (3) and reaction rate (4) distribution of $CL1$ at $\tau/\tau_{ref} = 1.92$ (a), $\tau/\tau_{ref} = 2.24$ (b). In $(2.b)$ T is scaled by 2.2 and in $(4.b)$ ω by 50.7. The snapshot is at $z/L = 0.5$ and spans $0.3125 < x/L < 0.6250$ and $0.1560 < y/L < 0.4685$.

the slow progression of the maximum mixture fraction, ξ_{max}: from about $\xi_{max} \approx 0.12$ to 0.16 between the times of Figs. 4.4a and 4.4b. Just before autoignition (Fig. 4.4c), the maximum T can be found around $\eta = 0.09$, while after localized autoignition (Fig. 4.4d), which occurs at about this mixture fraction, we observe a very large scatter for all η. In addition, ξ_{max} keeps increasing due to the enhanced evaporation. At later times (not shown), the temperature scatter *vs.* η assumes the expected shape from non-premixed combustion. The main qualitative features of autoignition revealed here are fully consistent with results from gaseous autoignition DNS [12; 23], but the conditional scatter seems to be much larger.

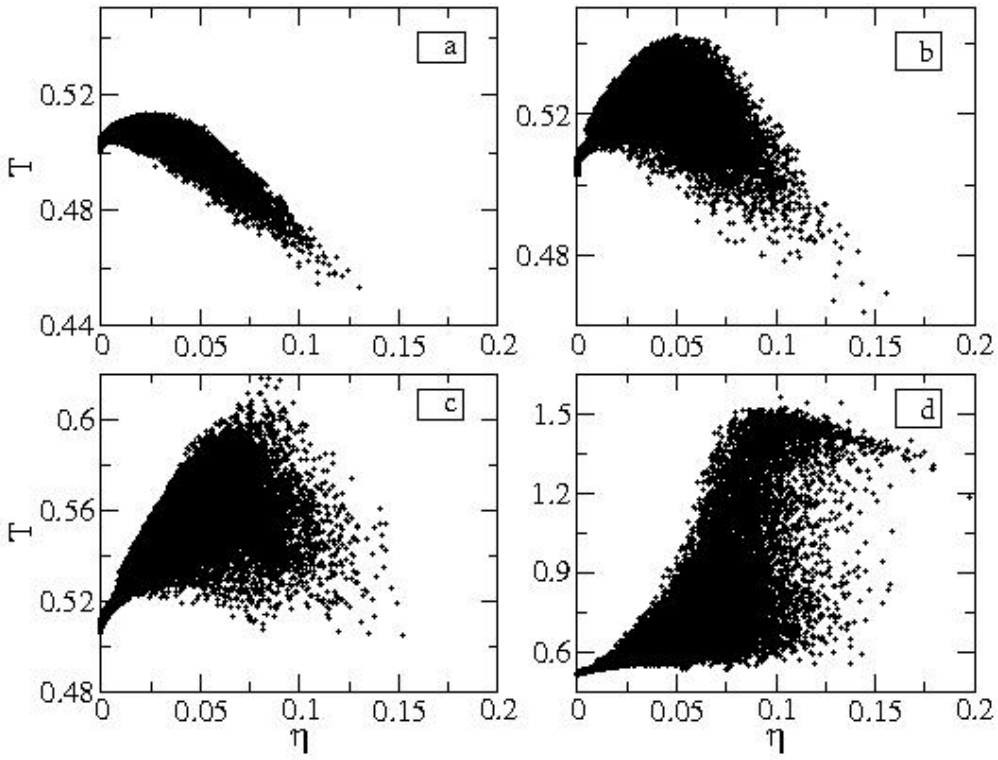

Figure 4.4: Scatter plots of temperature against mixture fraction for case $CL1$ at (a) $\tau/\tau_{ref} = 1.2$, (b) $\tau/\tau_{ref} = 1.6$, (c) $\tau/\tau_{ref} = 1.92$, and (d) $\tau/\tau_{ref} = 2.24$. [3]

Figure 4.5 shows scatter plots of reaction rate against the cell mixture fraction η at the same time steps as in Figure 4.4, using data from the whole domain. The red dotted line denotes the mean reaction rate. It can be seen for all τ/τ_{ref} that the reaction

rate increases conditional with mixture fraction initially and then follows a maximum and decreases afterwards for the highest values of mixture fraction. The spread of the reaction rate scatter is wider around its mean maximum. For $\tau/\tau_{ref} = 1.2$ and $\tau/\tau_{ref} = 1.6$ the most reactive mixture fraction region is around $\xi = 0.075$. This region shifts slightly to $\xi = 0.1$ for later time steps, similar to observation in purely gaseous cases [12].

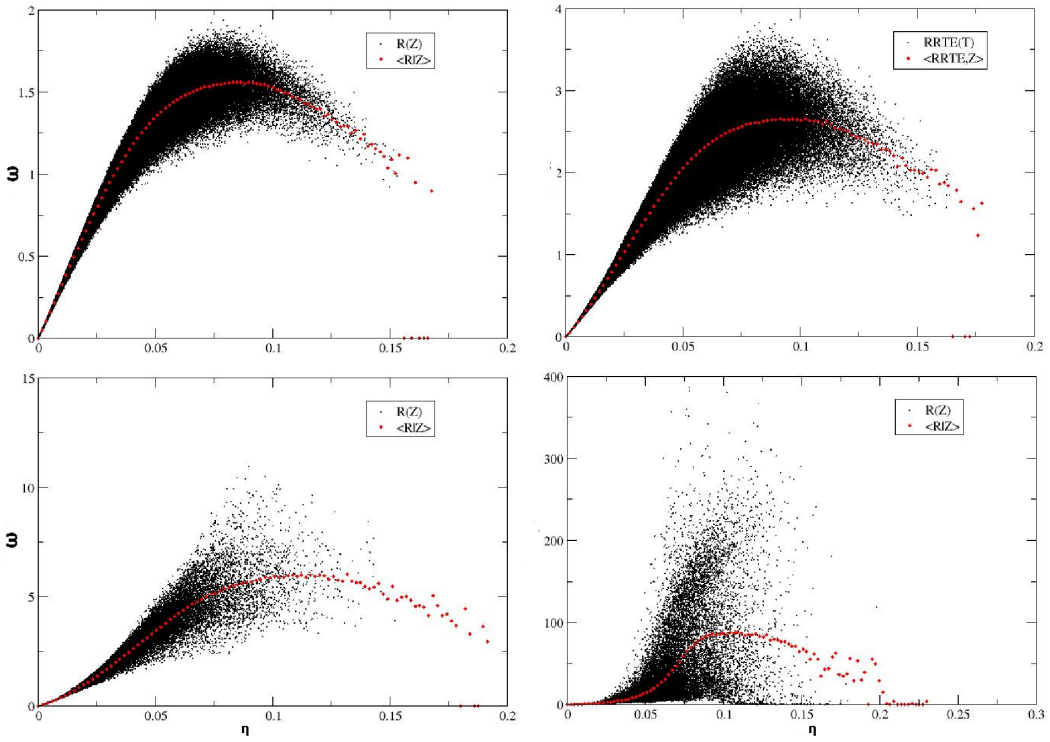

Figure 4.5: Scatter plots of reaction rate against mixture fraction for case $CL1$ at (a) $\tau/\tau_{ref} = 1.2$, (b) $\tau/\tau_{ref} = 1.6$, (c) $\tau/\tau_{ref} = 1.92$, and (d) $\tau/\tau_{ref} = 2.24$. [3]

4.3.3 Effect of initial droplet size

The unconditionally-averaged (over $y - z$ planes) ξ, N and evaporation rate m are shown in Fig. 4.6 at the same time (before autoignition) for the three simulations. It is evident that the droplet-laden region is uniform (in the mean) and that the turbulence

causes a broadening of the mixing region. The higher m associated with the small Θ_0 causes a higher mean mixture fraction and a higher mean scalar dissipation, since the small-scale structure of the ξ field contains higher local values and hence steeper local gradients. Note that complete evaporation implies $\langle\xi\rangle \approx 0.12$, so Fig. 4.6 implies that evaporation for the smallest Θ_0 at the time shown has progressed by about 30%.

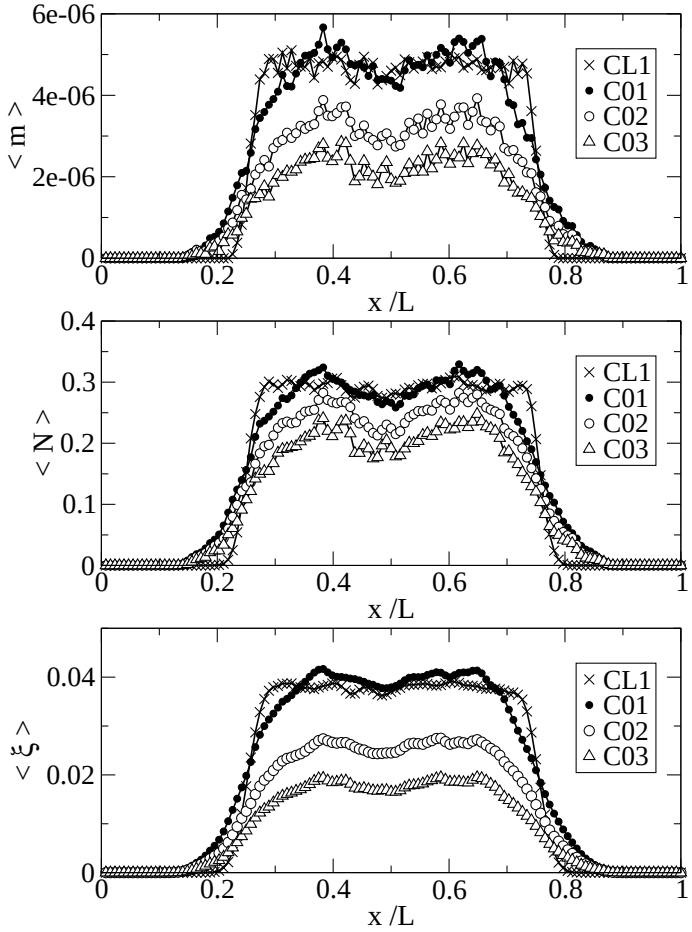

Figure 4.6: Mean evaporation rate (upper), scalar dissipation (middle) and mixture fraction (lower) at $\tau/\tau_{ref} = 1.6$. [3]

The mean mixture fraction field shows an increasing value of the mixture fraction with time and a broadening in the inhomogeneous direction due to droplet dispersion and turbulent mixing of the vapour already produced (Fig. 4.6). The low turbulence case shows a smaller broadening, but the mean ξ in the central part of the droplet-laden layer

seems to be affected little by the turbulence intensity due to the fact that the droplets are very small and the Sherwood number is only mildly different from 2. The wider extent of the region with finite evaporation rate in Fig. 4.6 is due to the higher velocity fluctuations in the high turbulence case that disperse the droplets more.

Figure 4.7 shows the corresponding conditional averages using data from the whole domain. The trends with Θ_0 are now reversed: the conditional evaporation rate $\langle m|\eta\rangle$ and the conditional scalar dissipation $\langle N|\eta\rangle$ are both increasing with Θ_0. This can be understood by the higher content at $\eta > 0$ of the pdf of mixture fraction $P(\eta)$ as the droplet diameter decreases (see, for example, Fig. 4.11 discussed later), since

$$\langle N\rangle = \int_0^1 \langle N|\eta\rangle P(\eta) d(\eta) \tag{4.1}$$

The present data are consistent with the 2-D simulations of Ref. [17] and with Réveillon and Demoulin [85], who suggested that the droplet segregation for droplets with a Stokes number ($St = \tau_d/\tau_K$, with τ_K the Kolmogorov timescale) smaller than unity is controlled by micro mixing. For cases with larger Θ_0 with an increase in St towards unity, the segregation is increasing, leading to a less homogeneous mixture, with a corresponding higher conditional scalar dissipation. $\langle N|\eta\rangle$ increases with η at first, but for $\eta > 0.07$ seems to change little with η; however, a peak is evident for the largest droplet case. The conditionally-averaged temperature $\langle T|\eta\rangle$ is highest for the smallest droplet case for all η.

The volume-averaged temperature *vs.* time normalised by τ_{ref} (Fig. 4.2) shows that autoignition occurs earliest for the smallest diameter. It is also clear that ignition occurs later than τ_{ref}. Retardation of autoignition over τ_{ref} in gaseous fuels is associated with increased $\langle N|\eta\rangle$ [12] and the present data are consistent with this concept, since the earliest autoignition (case C01) is associated with lowest conditional scalar dissipation (Fig. 4.7). Note that using the *unconditionally*-averaged N (Fig. 4.6) rather than the conditionally-averaged (Fig. 4.7) would give the wrong trend of autoignition time with Θ_0. The earlier ignition in the small droplet case is also consistent with the earlier generation of the most reactive mixture fraction due to the quicker evaporation.

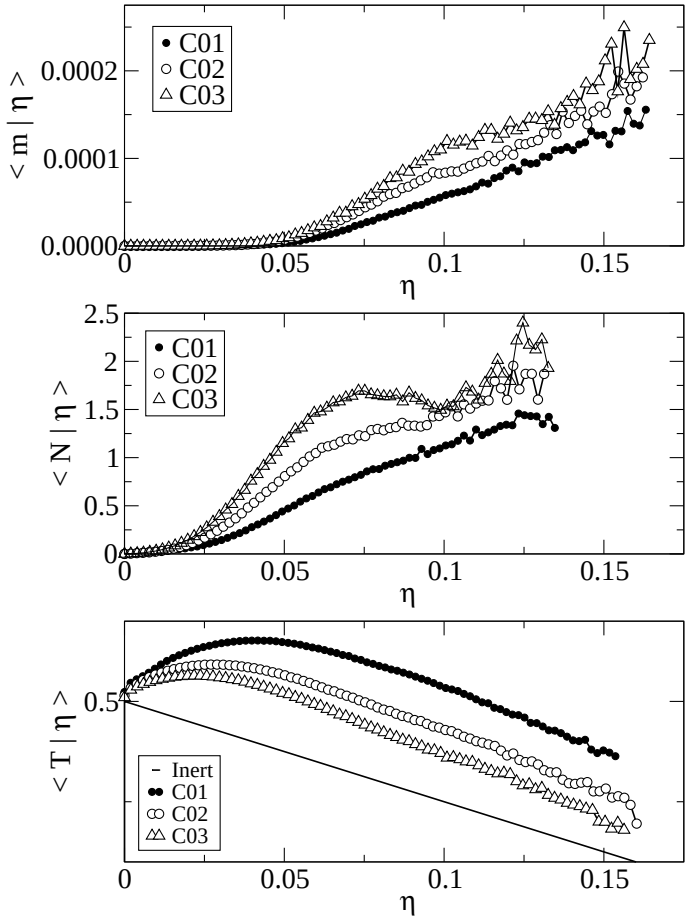

Figure 4.7: Conditionally-averaged evaporation rate $\langle m|\eta\rangle$, scalar dissipation rate $\langle N|\eta\rangle$ and temperature $\langle T|\eta\rangle$ at $\tau/\tau_{ref} = 1.6$. [3]

4.3.4 Locations of high $\langle\dot{\omega}|\eta\rangle$

Figure 4.8 shows $\langle\dot{\omega}|\eta\rangle$ at various times before autoignition. For all Θ_0, $\langle\omega|\eta\rangle$ shows the same characteristic curve with a broad maximum of the reaction rate around $\eta = 0.09$, which is very close to the mixture fraction of minimum autoignition time of gaseous homogeneous mixtures (Fig. 4.2). Hence, the most reactive mixture fraction ξ_{MR} does not seem to depend much on whether it is defined from Fig. 4.4, 4.8 or 4.2. The initial droplet size Θ_0 does not have an impact on ξ_{MR}.

In an effort to understand better the autoignition location, Fig. 4.9 shows the reaction rate $\langle\omega|N,\eta\rangle$ doubly-conditionally averaged on N and η. For all levels of N, $\langle\omega|N,\eta\rangle$

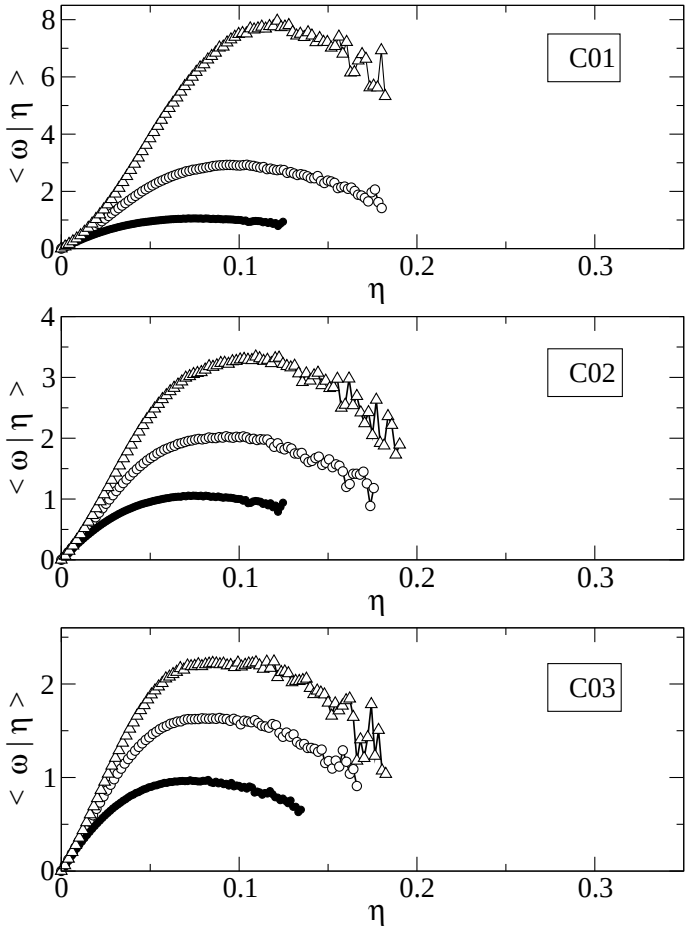

Figure 4.8: Conditional reaction rate $\langle\omega|\eta\rangle$ at $\tau/\tau_{ref} = 0.64$ (•), 1.6 (○) and 1.92 (△). [3]

shows a maximum around $\eta = \xi_{MR}$ and it is evident that high values of ω are found at low N. Therefore, as for gaseous fuels, locations of autoignition are found in regions with low scalar dissipation and a certain value of mixture fraction.

Figure 4.10 shows the conditional correlation coefficient between $\langle\omega|\eta\rangle$ and $\langle N|\eta\rangle$ as a function of mixture fraction. This type of correlation is similar to basic cross-validation between two variables, but in addition the correlation is conditional on a third variable. The purpose is to find the unique variance between the reaction rate and scalar dissipation rate while eliminating the variance from mixture fraction. The shape is similar to the correlation coefficient of a purely gaseous case (e.g. Fig. 11 in

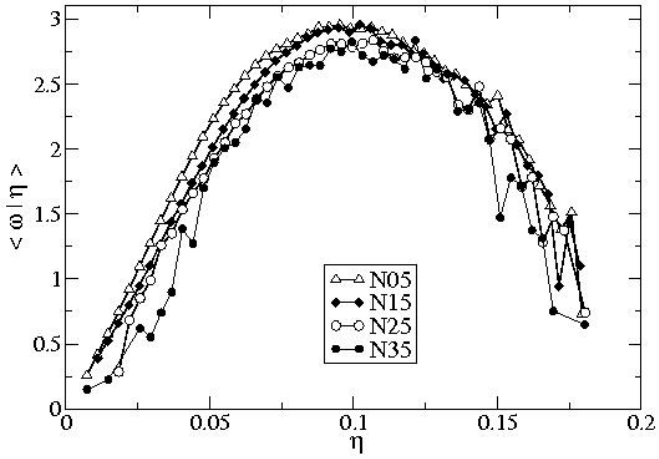

Figure 4.9: Doubly-conditional reaction rate $\langle\omega|N,\eta\rangle$ of case $C01$ at $\tau/\tau_{ref} = 1.6$, where $N05$ implies $0 < N < 1$, $N15$: $1 < N < 2$, $N25$: $2 < N < 3$ and $N35$: $3 < N < 4$. [3]

[12]), but tends to be much less negative. A distinctive difference is the occurrence of a local increase of the correlation coefficient around $\eta = 0.09$ at the moment of ignition ($\tau/\tau_{ref} = 2.24$) that originates from the enhanced evaporation (and hence higher N) as the temperature increases, which implies a positive correlation between N and T when combustion begins. The fact that the strong negative correlation between the temperature and scalar dissipation has been broken by the droplet evaporation (e.g. a correlation coefficient of about -0.3 before autoignition in Fig. 4.10 *vs.* -0.9 [12]) and the large conditional scatter have a bearing on second-order CMC models for diesel autoignition [79].

4.3.5 Influence of droplet evaporation on $P(\eta)$

Figure 4.11 shows $P(\eta)$, constructed using the samples from the whole DNS domain (i.e. including the air-only regions outside the droplet-laden slab) at the same time for the three simulations. It should be stated that both in Fig. 4.11 and 4.12 $P(\eta)$ has not been normalised. The PDF is wider and its peak occurs at larger mixture fractions with decreasing Θ_0. The shapes observed here are consistent with Refs. [17; 83].

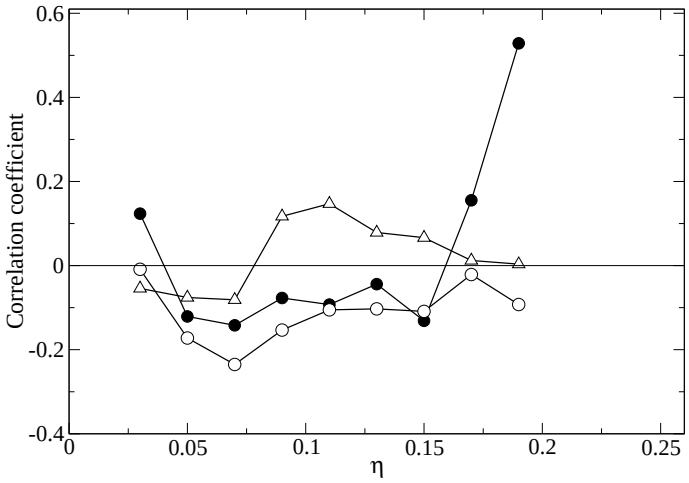

Figure 4.10: Conditional correlation coefficient between ω and N against η for case $C01$ at $\tau/\tau_{ref} = 1.6$ (•), 1.92 (○) and 2.24 (△).

The $P(\eta)$ is also shown in Fig. 4.12 for a time just after autoignition. $P(\eta)$ is plotted in a conventional way (i.e. using the value of the mixture fraction at each cell of the domain), and also using only cells with liquid droplets (denoted as $P_{cell}(\eta)$). Additional to the peak at $\eta = 0$ corresponding to the clean air part of the domain, a local maximum around $\eta = 0.05$ exists, which increases with time. The shape of P_{cell} is similar to P but without the peak at $\eta = 0$, which suggests that the second peak originates from the droplet evaporation [81].

Figure 4.12 also includes the PDF, $P(\eta_{sat})$, of the saturation fuel mass fraction for each droplet. The width of $P(\eta_{sat})$ increases in time since the droplet temperature spectrum becomes larger, especially after autoignition. For DNS with full resolution, where the region around the droplets is properly resolved, the resultant mixture fraction PDF would be a composite between $P(\eta)$ and $P(\eta_{sat})$. It is evident that further work is needed on this topic, since the evaporation and localised autoignition can cause large variations of both these PDF's.

Finally, the saturation vapour mass fraction, ξ_{sat}, conditionally-averaged over the local value of the mixture fraction in the computational cell (Fig. 4.13) is virtually independent from the mixture fraction of the cell, but depends on time.
The change of $\langle \xi_{sat} | \eta_{cell} \rangle$ originates from the increase in T which determines ξ_{sat}

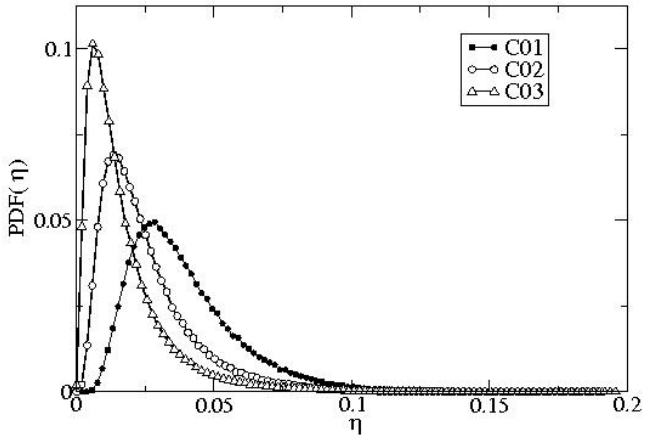

Figure 4.11: Probability density functions of mixture fraction for cases $C01$, $C02$ and $C03$ at $\tau/\tau_{ref} = 1.6$.

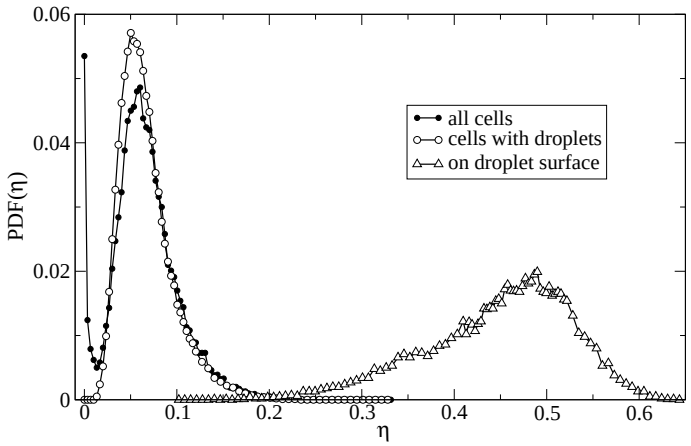

Figure 4.12: Probability density function of mixture fraction $P(\eta)$ for case $C01$ at $\tau/\tau_{ref} = 2.4$.

through the Clausius-Clayperon equation. This finding supports the conclusion by Mortensen and Bilger [78], that a given value of ξ can not directly imply a corresponding evaporation rate. Previous work [17; 30; 75] suggested a conditional source $\langle m|\eta\rangle$ proportional to the value of η (i.e. ξ_{cell}). This was related to the volume averaging process [78], where a larger value of ξ_{cell} means that more droplets are found in the cell resulting in a higher ξ generation rate. This is also confirmed in Fig. 4.6, showing higher values of the evaporation rate for cases with larger Θ_0. Interpreting $\langle m|\eta\rangle$ as having a causal dependence on the computational cell mixture fraction is contrary to

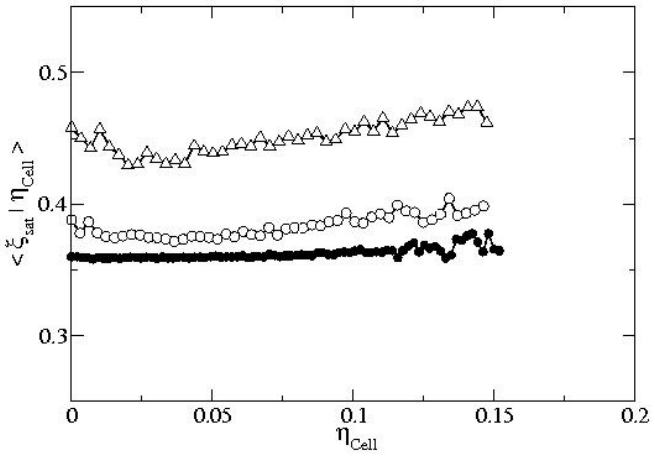

Figure 4.13: Averaged droplet surface mixture fraction ξ_{sat} conditional on cell mixture fraction η_{cell} for case $C01$ at $\tau/\tau_{ref} = 1.6$ (•), $\tau/\tau_{ref} = 2.24$ (○) and $\tau/\tau_{ref} = 2.4$ (△).

the assumption of Ref. [11] that evaporation occurs at ξ_{sat} (the physical picture implied here as well), and hence it is not clear whether the modelled $\langle m|\eta\rangle$ has general validity. The proper validation of mixture-fraction based approaches for spray combustion therefore necessitate fully-resolved DNS. Data such as those in Fig. 4.13 can assist validation of the transport equation for $\langle\xi_{sat}\rangle$ proposed previously [11].

4.3.6 Conclusion

The present simulations demonstrate the impact of droplet evaporation on autoignition of n-heptane fuel droplets in hot ambient air incorporating three-dimensional isotropic decaying turbulence. The main findings are:

• Autoignition is delayed when increasing the initial droplet size, possibly related to the higher conditional scalar dissipation rates in areas with droplet evaporation when the droplets are large and to the slower generation of fuel vapour.

• The highest reaction rates originate at locations where the mixture fraction is around the most reactive mixture fraction, whose value was independent from the droplet size and which can be determined independently from a series of homogeneous

calculations. Autoignition locations are also associated with low scalar dissipation rate. However, the correlation between scalar dissipation rates and reaction rates around the most reactive mixture fraction is weaker than for purely gaseous autoignition.

• Extra care is needed when discussing the mixture fraction PDF and the conditional evaporation rate due to the fact that the steep gradients in the proximity of the droplet surface are not resolved and hence the resolved (i.e. cell) mixture fraction is not related to the value at which evaporation occurs.

4.4 DNS of autoignition of cold saturated spray in hot surrounding

4.4.1 Setup

The setup is identical to the setup presented in section 4.3, expect the following: droplets were randomly distributed in a thin rectangular gas-fuel vapor layer between $(x/L)_{left} = 0.35$ and $(x/L)_{right} = 0.65$ where the surrounding gas-fuel vapor temperature is in equilibrium with the non-dimensional droplet temperature $T_d = -0.018$. The gas-fuel vapor mixture is initialized at the saturation mixture fraction $\xi_S = 0.02$ on the droplet surface, which can be established from the Clausius Clayperon equation for T_d. Since the droplets are in a fuel vapour saturated surrounding no initial evaporation is taking place. The non-dimensional gas temperature in the layers on both sides of the gas-fuel vapor is at $T = 0.8$. Two cases $SL1$ and $SL2$ are investigated with initial droplet diameters of $\Theta = 20\mu m$ and $\Theta = 40\mu m$, respectively. The interface between the layers is done by an error function distribution for mixture fraction and gas temperature in x-direction. The motivation behind this setup is the fact that droplets will have to move into the hot air stream to start evaporating and hence the effect of mixing on autoignition may be different.

4.4.2 General evolution

The general evolution of the flow is visualized by contour plots of the instantaneous temperature T (Fig. 4.14), across planes normal to the z-axis, obtained short after au-

toignition and at later stages for case $SL1$.

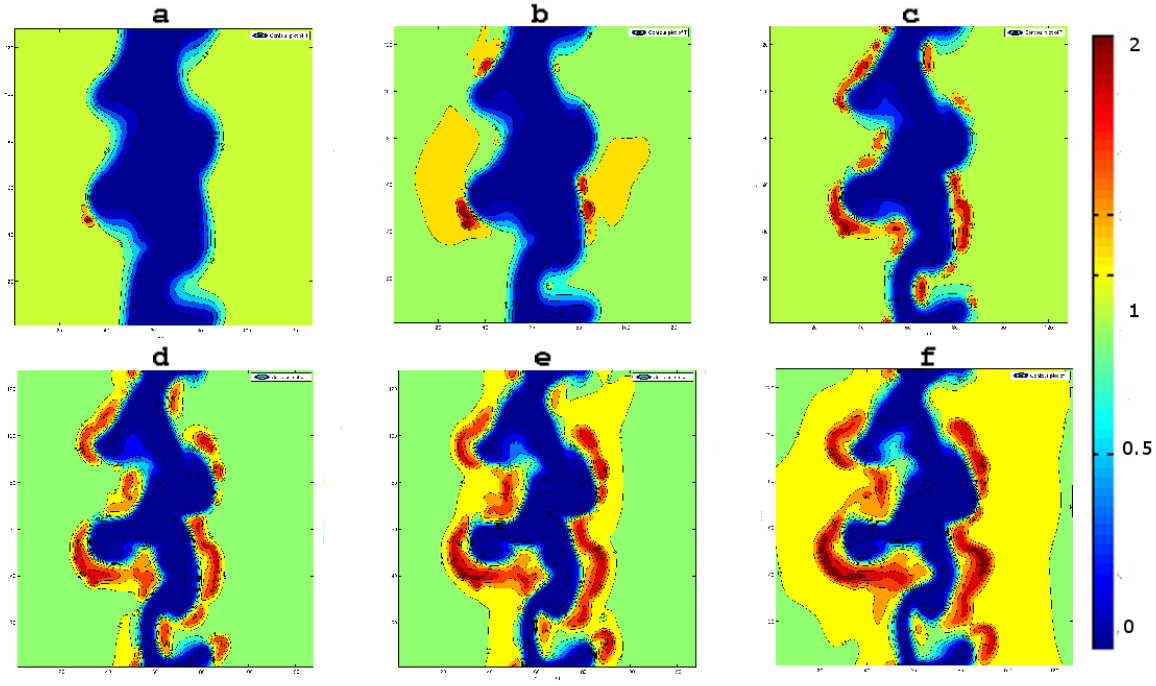

Figure 4.14: Temperature distribution of $SL1$ at six different time steps ((a) $\tau/\tau_{ref} = 1.92$, (b) $\tau/\tau_{ref} = 2.24$, (c) $\tau/\tau_{ref} = 2.56$, (d) $\tau/\tau_{ref} = 2.88$, (e) $\tau/\tau_{ref} = 3.20$, (f) $\tau/\tau_{ref} = 3.52$).

Already in the early stage ($\tau/\tau_{ref} = 0.64$ (a)) the turbulence has wrinkled the two interfaces between hot gas and gas-fuel vapor layer. In the first temperature contour plot a single autoignition region can be seen on the left interface between hot gas phase and cold gas-fuel vapor phase. At $\tau/\tau_{ref} = 0.64$ (a) several other autoignition spots are observed while the first one started to grow along the layer interface and heated up the region around. The wrinkling continues and with time several autoignition spots are established and growing along the layer interfaces. Over time the autoignition spots start to grow together and form larger reactive areas. Figure 4.15 shows the corresponding instantaneous mixture fraction contour plots. In the early stage the gas-fuel vapor layer is at ξ_S showing that no evaporation is taking place in this region.

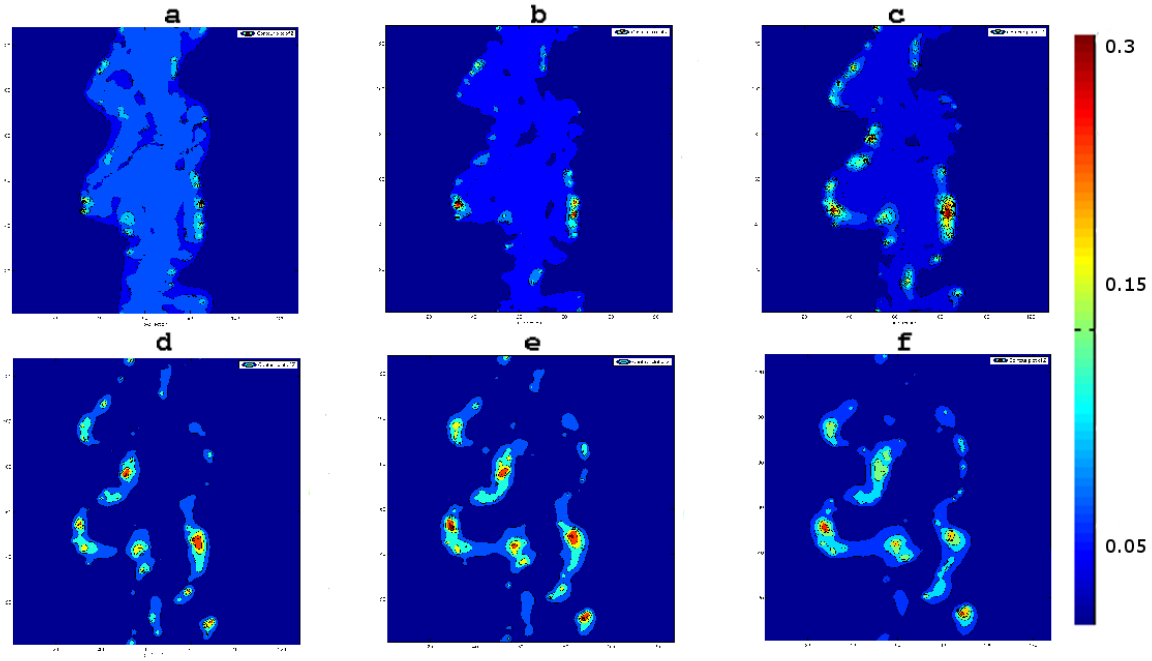

Figure 4.15: Mixture fraction distribution of $SL1$ at six different time steps. ((a) $\tau/\tau_{ref} = 1.92$, (b) $\tau/\tau_{ref} = 2.24$, (c) $\tau/\tau_{ref} = 2.56$, (d) $\tau/\tau_{ref} = 2.88$, (e) $\tau/\tau_{ref} = 3.20$, (f) $\tau/\tau_{ref} = 3.52$).

This is so in the core area of this layer in later stages while evaporation starts to take place in the two interface regions to the hot gas phase where droplets are placed into areas where the surrounding gas temperature is higher than the droplet temperature. The evaporation can be seen in higher levels of instantaneous mixture fraction in these regions. In regions where ξ gets near to ξ_{MR}, the most reactive mixture fraction, autoignition starts to take place as observed in Chapter 4.3. The highest level of mixture fraction are found in regions where autoignition spots emerged and the gas phase shows higher temperatures.

Figure 4.16 shows the instantaneous reaction rate at the same time steps as for the instantaneous temperature and mixture fraction contour plots. It confirms that reaction starts to take place in regions where the mixture fraction is increased to around ξ_{MR} due to the droplet evaporation. In later stages the highest reaction rates are then found around the initial autoignition kernels in the flame front where the mixture fraction is

increased due to evaporation. In the initial kernel the reaction rate drops back down again since most of the oxidizer is consumed. At the stage when autoignition kernels grow together to build larger regions, long thin layer of high reaction rates are formed in the two interface regions.

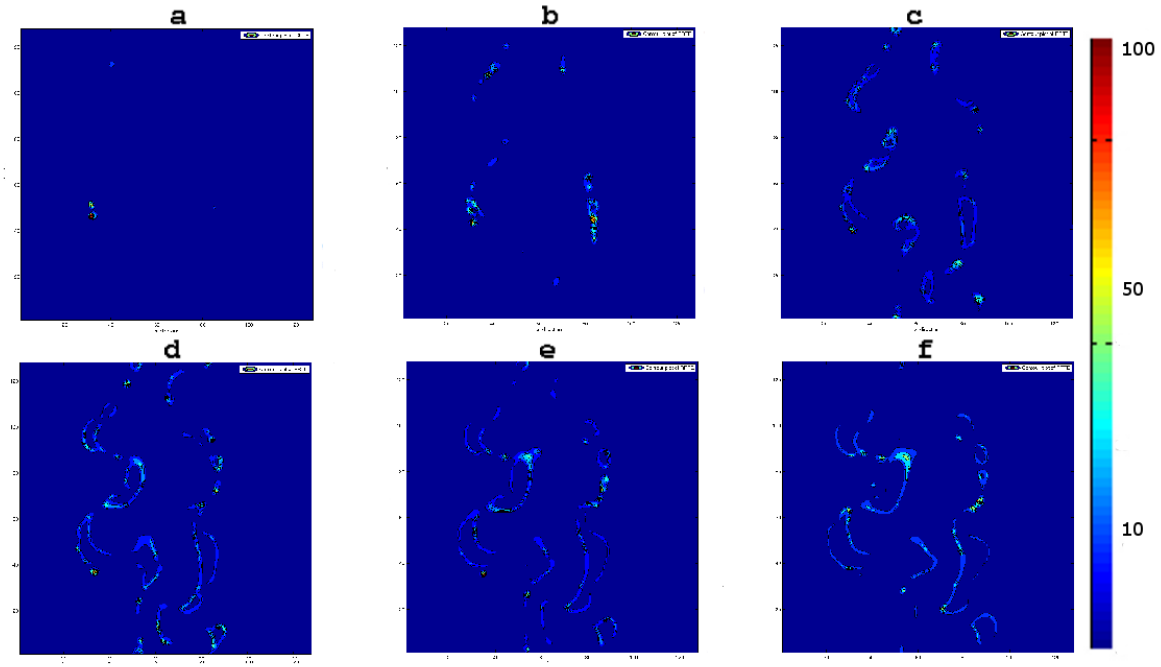

Figure 4.16: Reaction rates distribution of $SL1$ at six different time steps. ((a) $\tau/\tau_{ref} = 1.92$, (b) $\tau/\tau_{ref} = 2.24$, (c) $\tau/\tau_{ref} = 2.56$, (d) $\tau/\tau_{ref} = 2.88$, (e) $\tau/\tau_{ref} = 3.20$, (f) $\tau/\tau_{ref} = 3.52$).

Figure 4.17 shows the mean evaporation rate and mixture fraction at several times from $\tau/\tau_{ref} = 0.64$ to $\tau/\tau_{ref} = 3.20$. Mean values are taken over $y - z$ planes. At $\tau/\tau_{ref} = 0.64$ two small peaks in the mean evaporation rate can be seen on each side of the interface region. At later stages these peaks are weakened and a more even distribution of evaporation rate over the two interface regions and droplet slab layer is found. This is due to the turbulence which wrinkles the droplet slab layer and the two interface regions around each other. At $\tau/\tau_{ref} = 0.64$ the mean mixture fraction plot shows the initial value $\xi = 0.02$ of the droplet slab layer and the error function

distribution over the interface regions. At later time steps the mean mixture fraction is increased by the evaporation which takes place in the interface regions.

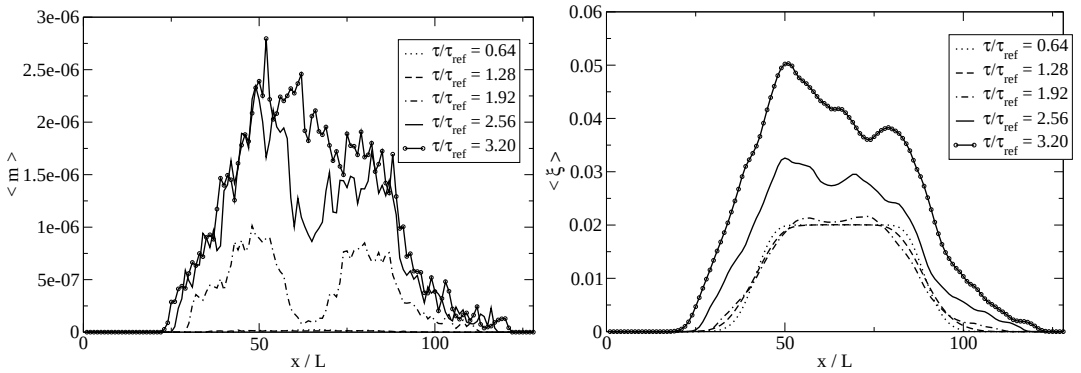

Figure 4.17: Mean evaporation rate (left) and mixture fraction (right) at several τ/τ_{ref}.

Figure 4.18 shows the mean reaction rate and scalar dissipation rate at several times from $\tau/\tau_{ref} = 0.64$ to $\tau/\tau_{ref} = 3.20$ with mean values taken over $y - z$planes. At $\tau/\tau_{ref} = 0.64$ and $\tau/\tau_{ref} = 1.28$ almost no reaction is observed in the two interface regions while at later time steps the reaction rate increases rapidly. Simultaneously for the scalar dissipation, at $\tau/\tau_{ref} = 0.64$ and $\tau/\tau_{ref} = 1.28$ only mild scalar dissipation is produced by the droplet evaporation in the interface regions, while at later stages with higher evaporation rates also the scalar dissipation rate increases.

Figure 4.19 shows the instantaneous non-dimensional temperature contour plots at four different times from $\tau/\tau_{ref} = 3.68$ to $\tau/\tau_{ref} = 4.64$. At these later stages the turbulence managed to wrinkle the inner droplet laden layer so that islands of the hot reacting interface region are found within the cool droplet laden region. Two long thin flame layers are established on either side along the interface between the droplet layer and the hot gas phases.

Figure 4.20 shows the instantaneous mixture fraction contour plots at the same time steps as in Figure 4.19. The contour plots show high levels of ξ in regions with high

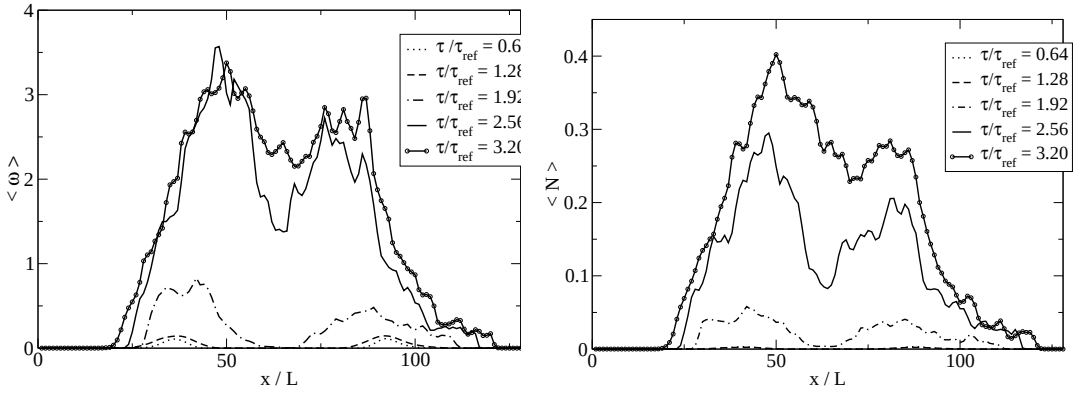

Figure 4.18: Mean reaction rate (left) and scalar dissipation rate (right) at several τ/τ_{ref}.

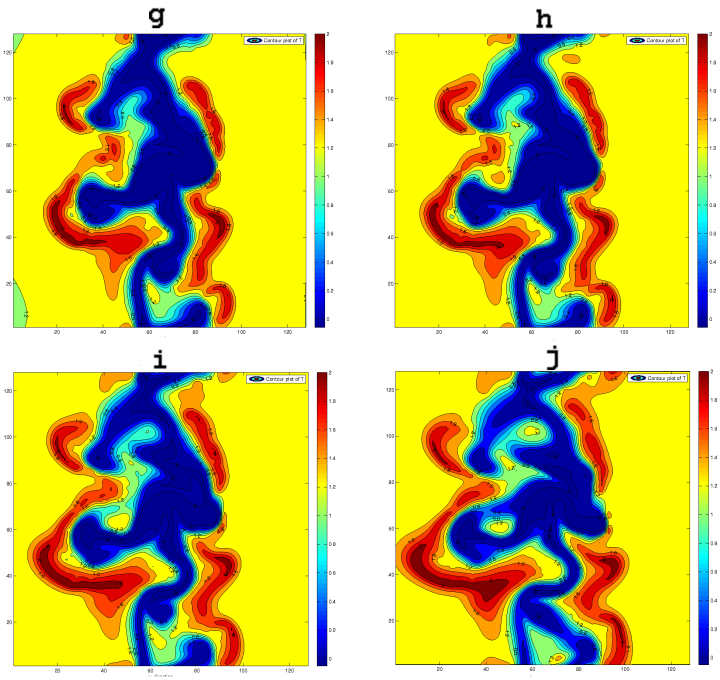

Figure 4.19: Temperature distribution of $SL1$ at four different time steps after 4.14. ((g) $\tau/\tau_{ref} = 3.68$, (h) $\tau/\tau_{ref} = 3.84$, (i) $\tau/\tau_{ref} = 4.16$ and (j) $\tau/\tau_{ref} = 4.64$.)

temperature, predominately in the interface regions (4.19). In the very hot regions the mixture fraction can be found near to $\xi = 0.9$ due to the extensive droplet evaporation.

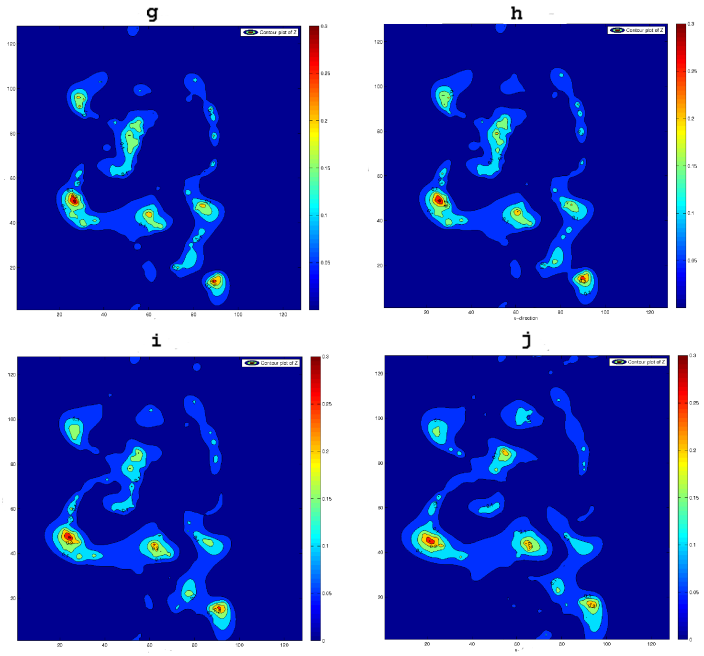

Figure 4.20: Mixture fraction of $SL1$ at four different time steps after 4.14. ((g) $\tau/\tau_{ref} = 3.68$, (h) $\tau/\tau_{ref} = 3.84$, (i) $\tau/\tau_{ref} = 4.16$ and (j) $\tau/\tau_{ref} = 4.64$.)

Figure 4.21 shows he instantaneous reaction rate contour plots at the same time steps as in Figure 4.19 and Figure 4.20. In $\tau/\tau_{ref} = 3.68$ (g) high reaction rates are found around the initial autoignition kernel and grow towards the hot gaseous phase regions and towards the droplet laden layer. At later stages in $\tau/\tau_{ref} = 3.84$ and $\tau/\tau_{ref} = 4.16$ the thin reaction layers are growing together, forming two long thin layer lines of high reaction along the interface regions, one to the hot gaseous region and one to the droplet laden region. In $\tau/\tau_{ref} = 4.68$ high reaction rates are found in islands of heated interface regions which is surrounded by the droplet laden layer.

4.4.3 Scatter plot of temperature and reaction rate

Figure 4.22 shows scatter plots of non-dimensional temperature conditional on mixture fraction at different time steps from $\tau/\tau_{ref} = 0.64$ to $\tau/\tau_{ref} = 4.64$.

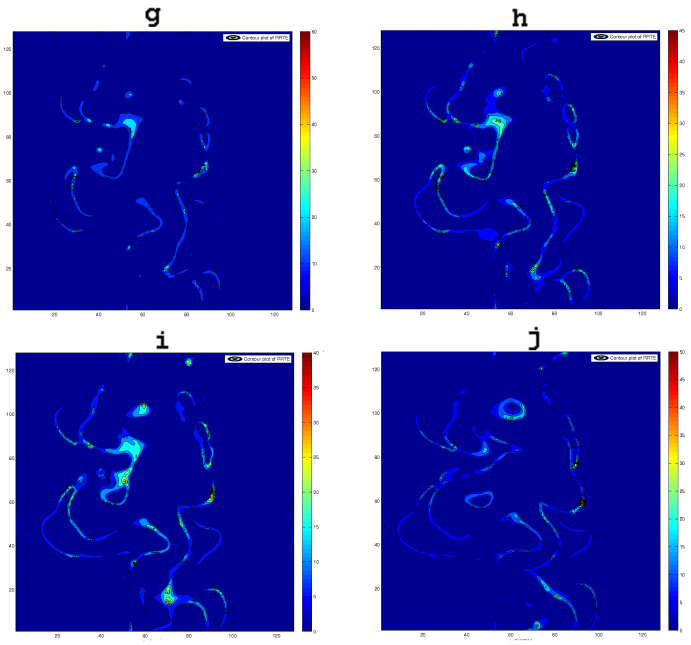

Figure 4.21: Reaction rate of $SL1$ at four different time steps after 4.14. ((g) $\tau/\tau_{ref} = 3.68$, (h) $\tau/\tau_{ref} = 3.84$, (i) $\tau/\tau_{ref} = 4.16$ and (j) $\tau/\tau_{ref} = 4.64$.)

Initially all cells within the droplet laden layer are at $T = -0.07$ and $\xi = 0.02$ while cells within the hot gas layers on the outer sides are at $T = 0.8$ and $\xi = 0.0$. The cells in the two interface regions are having a temperature and mixture fraction distribution following an error function. At $\tau/\tau_{ref} = 0.64$ several autoignition spots are established in the interface region which can be seen in the temperature scatter plot by cells with $T > 0.8$ around ξ_{MR}. At later steps more and more cells are under influence of evaporating droplets and have higher level of ξ while also more cells are part of flame kernels. The maximum non-dimensional temperature observed is around $T = 2.0$ in between $\xi = 0.05$ and $\xi = 0.09$. Figure 4.23 shows scatter plots of reaction rate over mixture fraction. Reaction starts to take place in the early stages along the two interface regions visualized by the two peaks in $\dot{\omega}$ at $\tau/\tau_{ref} = 0.64$. Later reaction rates increase with their maximum around ξ_{MR}.

For a better insight into the temperature and reaction rate scatter plots, Figure 4.24 shows the mean conditional temperature and reaction rate for case $SL1$ and $SL2$ at

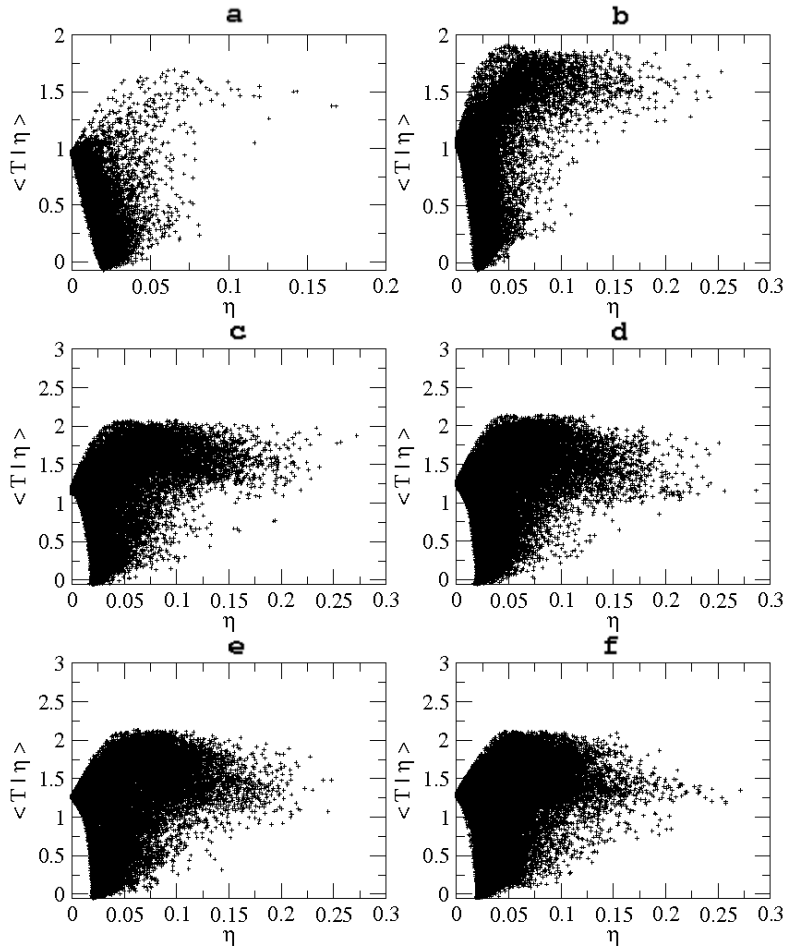

Figure 4.22: Scatter plots of temperature against mixture fraction for case $SL1$ at several τ/τ_{ref}. ((a) $\tau/\tau_{ref} = 0.64$, (b) $\tau/\tau_{ref} = 1.28$, (c) $\tau/\tau_{ref} = 1.92$, (d) $\tau/\tau_{ref} = 2.56$, (e) $\tau/\tau_{ref} = 3.20$, (f) $\tau/\tau_{ref} = 4.64$.)

two different τ/τ_{ref}. It can be seen that the mean conditional temperature and reaction rate is almost zero around $\xi = 0.02$ for both τ/τ_{ref}, which is the value of mixture fraction present in the saturated droplet layer. On both to the lean and rich side the mean conditional temperature and reaction rise in time with the maximum mean conditional temperature around ξ_{MR} as observed in Figure 4.7. The 'V'-shaped gap in both temperature and reaction rate is getting more narrow over time, which is in agreement with the temperature contour plots (Figure 4.14) showing that the initial saturated droplet

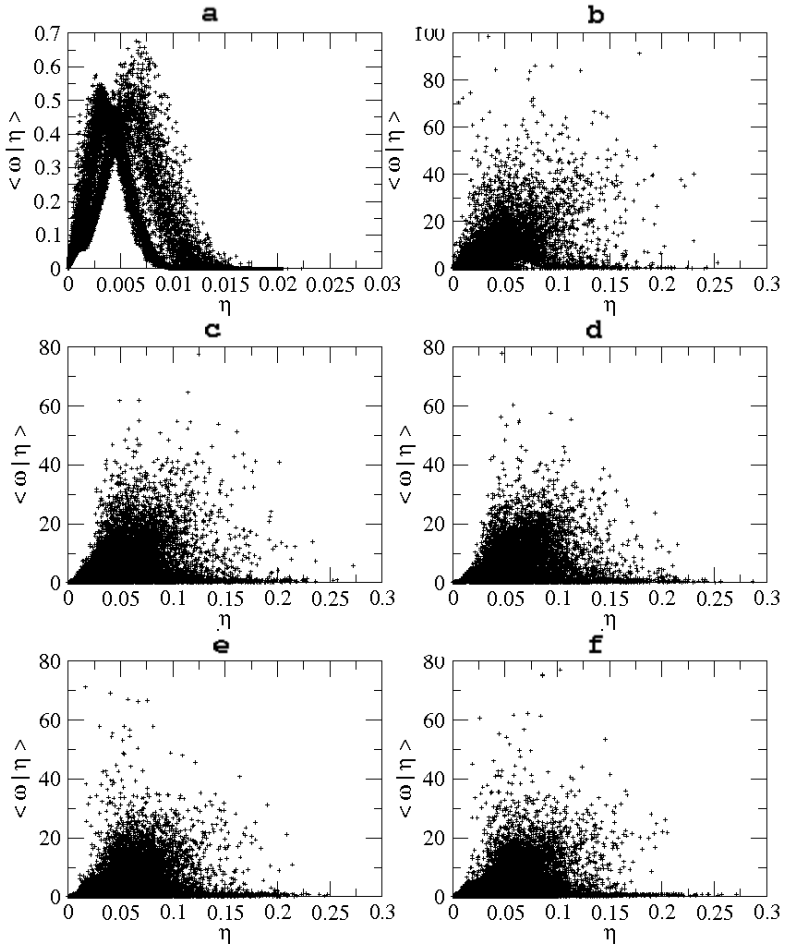

Figure 4.23: Scatter plots of reaction rate against mixture fraction for case $SL1$ at several τ/τ_{ref}. ((a) $\tau/\tau_{ref} = 0.64$, (b) $\tau/\tau_{ref} = 1.28$, (c) $\tau/\tau_{ref} = 1.92$, (d) $\tau/\tau_{ref} = 2.56$, (e) $\tau/\tau_{ref} = 3.20$, (f) $\tau/\tau_{ref} = 4.64$.)

layer is decreasing in size over time. For both mean conditional temperature and reaction rate, case $SL2$ shows higher levels for both τ/τ_{ref} suggesting that for this flow setup cases with larger initial droplet size autoignite earlier.

Figure 4.25 is showing the reaction rate over mixture fraction and scalar dissipation at $\tau/\tau_{ref} = 1.28$ and $\tau/\tau_{ref} = 1.92$. It can be seen in $\tau/\tau_{ref} = 1.92$ as stated before (Section 4.3) that reaction starts to take place near the most reactive mixture fraction

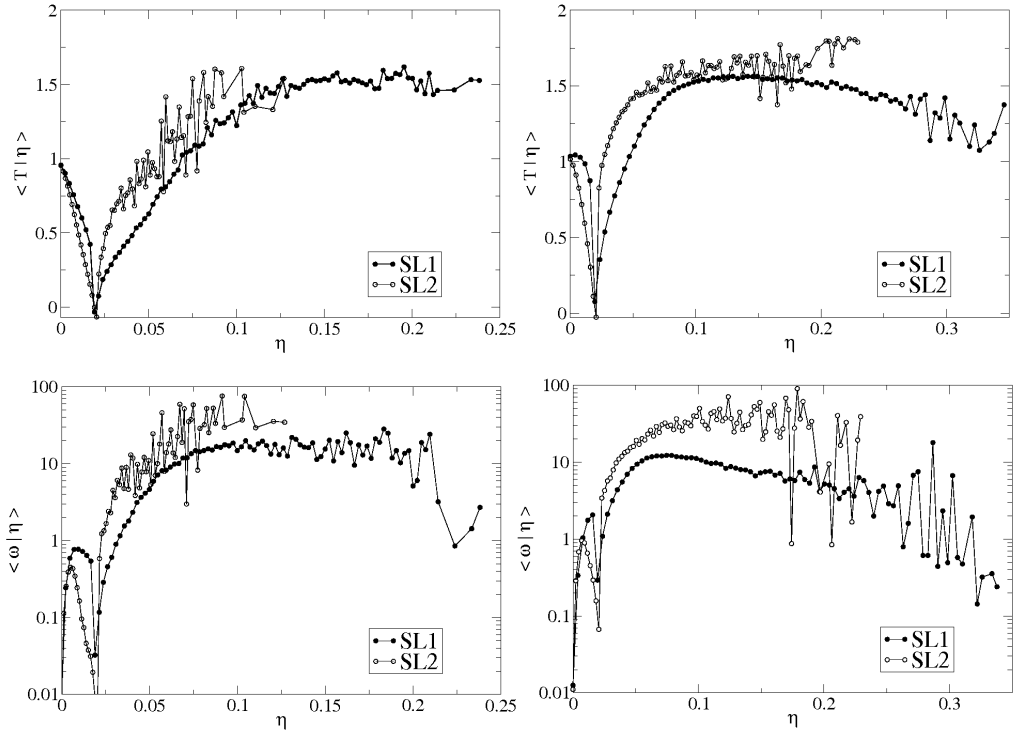

Figure 4.24: Mean conditional temperature (above) and conditional reaction rate (below) for case $SL1$ and $SL2$ at (a) $\tau/\tau_{ref} = 1.92$ and (b) $\tau/\tau_{ref} = 2.56$)

ξ_{MR}. Since ξ_{MR} has been established in regions of droplet evaporation, there is also a high level of scalar dissipation present.

4.4.4 Conclusion

The present simulations demonstrate the impact of droplet evaporation on autoignition of n-heptane fuel droplets in cold saturated fuel-gas vapour in hot surrounding incorporating three-dimensional isotropic decaying turbulence. As seen in Section 4.3 the highest reaction rates originate at locations where the mixture fraction is around the most reactive mixture fraction. In addition autoignition locations are also associated with low scalar dissipation rate.

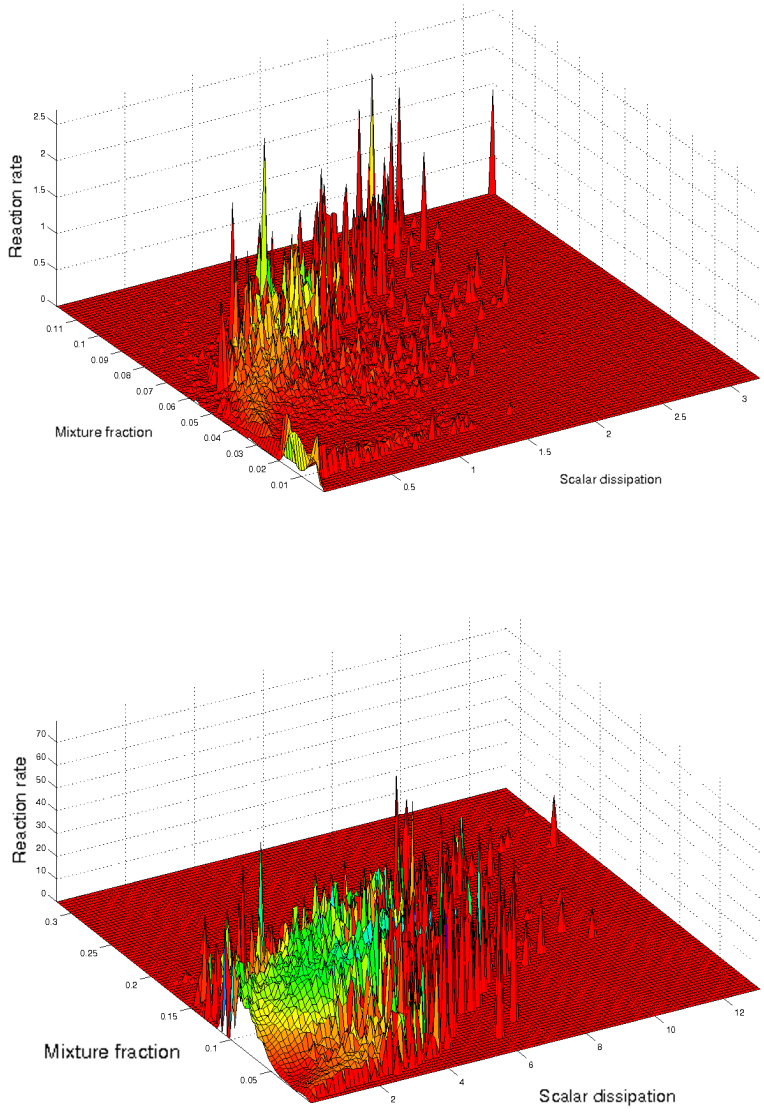

Figure 4.25: Reaction rate over mixture fraction and scalar dissipation at $\tau/\tau_{ref} = 1.28$ (above) and $\tau/\tau_{ref} = 1.92$ (below). The color code of the graphs does not have a specific meaning but is intended to help visualization.

Chapter 5

Validation of CMC for spray autoignition

5.1 Objectives

To validate the established CMC equations extended to two-phase flows, as presented in Chapter 3, zero dimensional CMC simulations are carried out based on DNS case $C01$ and $C02$ (Table 6.1) from Chapter 4. The advantage of using zero dimensional CMC for validation is that it simplifies both the conditional mass fraction and temperature equation while still keeping all source terms due to droplet evaporation. This makes the zero dimensional version of CMC a perfect starting point for validating the extended CMC model for two-phase flows.

5.2 Numerical approach

For zero dimensional problems with constant c_p, Eq. 3.42 and Eq. 3.49 can be simplified to

$$\frac{\partial Q}{\partial t} = \langle N|\eta\rangle \frac{\partial^2 Q}{\partial \eta^2} + \langle W|\eta\rangle + \langle S|\eta\rangle \left(1 - Q - (1-\eta)\frac{\partial Q}{\partial \eta}\right) \tag{5.1}$$

and

$$\frac{\partial Q_T}{\partial t} = \langle N|\eta\rangle \frac{\partial^2 Q_T}{\partial \eta^2} - \frac{1}{c_p}\sum_{\alpha=1}^{n} h_\alpha \langle W_\alpha|\eta\rangle$$
$$-\frac{h_{fg}}{c_p}\langle S|\eta\rangle - Q_T\langle S|\eta\rangle - \langle S|\eta\rangle(1-\eta)\frac{\partial Q_T}{\partial \eta} \tag{5.2}$$

where

$$\langle S|\eta\rangle = \langle S|\xi_S\rangle\delta(\eta-\xi_S) = \frac{\tilde{S}}{P(\xi_S)} \tag{5.3}$$

respectively. This set of equations is denoted as 0D-CMC. For both equations all source terms due to droplet evaporation are still present. The conditional scalar dissipation $\langle N|\eta\rangle$ in Eq. (5.2) and Eq. (5.1) is provided by the DNS data which is described in Chapter 4 and augmented by a scalar dissipation model which is presented in the next section. Furthermore the evaporation rate S, the PDF of mixture fraction $P(\xi)$ and saturation mixture fraction $P(\xi_S)$ are extracted from DNS and supplied to the 0D-CMC. $P(\xi_S)$ provides the lower and upper boundary in mixture fraction space in between where evaporation takes place while $P(\xi)$ is needed to establish unconditional data. Figure 5.1 shows the setup of the 0D-CMC simulations. The 0D-CMC code uses the same 1-step reaction mechanism with the stoichiometry of heptane as in the DNS.

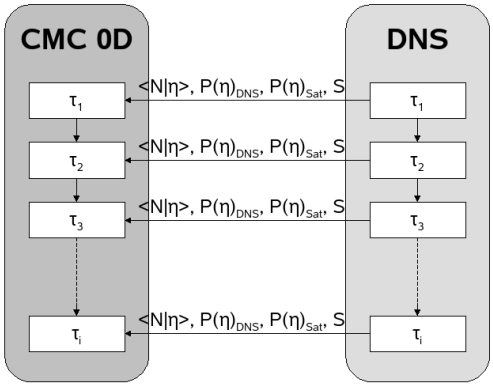

Figure 5.1: Setup for 0D-CMC code using DNS data at certain time steps

5.3 Scalar dissipation model

In 0D-CMC simulations the liquid-gas interface in mixture fraction space is at the saturation mixture fraction of the droplet ξ_S. Since $\langle N|\eta\rangle$ is provided by DNS data the range of N in mixture fraction space is limited to grid cell values of ξ of the DNS cells. Since most existing DNS of two-phase flows [3; 17; 30; 75] does not resolve the flow structure in the droplet surrounding, no data for $\langle N|\eta\rangle$ is available between ξ_S and ξ of the cell. A better resolution of the inter droplet space, as done by [65], is limiting the amount of droplets which can be put into the flow due to the high calculation demand so therefore here a subrgid model is preferred for $\langle N|\eta\rangle$, which establishes a physical treatment of the heat and mixture fraction diffusion in between the surrounding area of the droplet and the cell grid points. In [78] an estimate is given for the mean magnitude of gradient of ξ at the droplet surface based on the diffusive balance at the droplet surface. The model presented here tries to model the gradient of ξ not only on at the droplet surface but throughout the whole droplet inter space to the nearest CFD cell point where the droplet is located. At the droplet surface the model is identical to [78]. Figure 5.2 shows schematically an evaporating droplet within its cell. On the droplet surface we know the surface temperature T_S, saturation mixture fraction ξ_S and the saturation fuel mass fraction Y_S and hence the surface scalar dissipation rate N_S by using

$$N_S = \left(\frac{\nu}{Sc}\right) \frac{\partial \xi}{\partial r} \frac{\partial \xi}{\partial r} \tag{5.4}$$

where

$$\frac{\partial \xi}{\partial r} = \frac{Y_S - 1}{r_s} \ln\left(1 + B_m\right) \tag{5.5}$$

where B_m is the Spalding number given by $B_m = (Y_S - Y_\infty)/(1 - Y_S)$ and r_s the droplet radius. The model presented here shows a way to describe this curve. The idea is to subdivide each grid cell in mixture fraction space and to assume that each droplet creates a mixture fraction in the surrounding of a non-convective single droplet evaporation process. We use the following equations given in [2]:

$$\frac{\partial Y_f}{\partial r} = -\frac{(1 - Y_f)\dot{m}_f}{4\pi r^2 \rho D} \tag{5.6}$$

for the radial distribution of Y_f, where D, ρ and $\dot{m}_f$ are the diffusion coefficient, mixture density and evaporation rate respectively. Integrating Eq. (5.6) with $Y_f = Y_{Sat}$ at $r = r_s$ and $Y_f = Y_{Cell}$ at $r = r_{cell}$ leads to

$$\dot{m}_f = 4\pi \frac{1}{\left(\frac{1}{r_s} - \frac{1}{r_{Cell}}\right)} \rho D \ln\left(1 + B_m\right) \tag{5.7}$$

where r_{Cell} is the radial distance from the droplet center point to the cell node, assuming that droplets are located in the center of its occupying cell (Fig. 5.2).

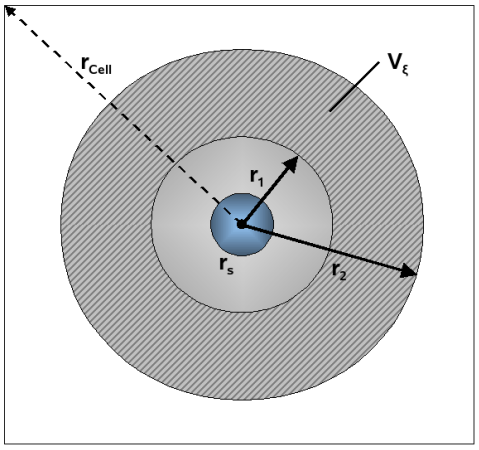

Figure 5.2: ξ_i-shell for ξ_i determined by r_1 and r_2.

Since we investigate here autoignition effects this model will be only valid prior to combustion and hence we assume

$$\frac{\partial Y_f}{\partial r} \approx \frac{\partial \xi}{\partial r}, \;\; Y_f \approx \xi \tag{5.8}$$

The scalar dissipation rate can be described by

$$N = D \left(\frac{\partial \xi}{\partial r}\right)^2 \tag{5.9}$$

and by using Eq. (5.6) in Eq. (5.9) using the assumption in 5.8 leads to

$$N = D\left(\frac{(1-\xi)\dot{m}_f}{4\pi r^2 \rho D}\right)^2 \tag{5.10}$$

With Eq. (5.6) the radial distance from the droplet r can be related to ξ by

$$r(\xi) = \frac{1}{\frac{1}{r_s} - \left(\frac{1}{r_s} - \frac{1}{r_{Cell}}\right)\frac{\ln(1-\xi)-\ln(1-Y_{Sat})}{\ln(1-\xi_{Cell})-\ln(1-Y_{Sat})}} \tag{5.11}$$

and with Eq. (5.11) in Eq. (5.10) leads to

$$N(\xi) = \left(\frac{1}{r_s} - \left(\frac{1}{r_s} - \frac{1}{r_{Cell}}\right)\frac{\ln(1-\xi)-\ln(1-Y_{Sat})}{\ln(1-\xi_{Cell})-\ln(1-Y_{Sat})}\right)^4 r_s^4 N_{Sat} \tag{5.12}$$

using

$$D = \left(\frac{1}{r_s} - \frac{1}{r_{Cell}}\right)^2 \frac{r_s^4 N_{Sat}}{\left(\ln(1-\xi_{Cell}) - \ln(1-Y_{Sat})\right)^2} \tag{5.13}$$

Figure 5.3 shows on the left N and Y_f over the radial distance from the droplet r/r_{Cell} with the droplet surface located at $r/r_{Cell} = 0.05$. Both N and Y_f are normalized by N_{Sat} and Y_{Sat}, respectively, for visual purpose. Both gradients have a steep decrease close to the droplet surrounding and fade out to their values set by the grid node (Y_{Cell},N_{Cell}) at $r/r_{Cell} = 1$. The lower graph shows r and N over mixture fraction ξ where the droplet surface is located at $\xi_S = 0.3$ and the cell node at $\xi_{Cell} = 0.005$. $\langle N|\eta\rangle$ is decreasing when moving away from the droplet surface while $\langle r|\eta\rangle$ is increasing as expected.

Using this model now on all droplets in the DNS solutions gives Figure 5.4 which shows the scatter plot of the scalar dissipation rate over mixture fraction. In black are the points of the subgrid model and in red of the DNS cells. On the r.h.s. of the graph N is plotted over the logarithmic scale to visualize N of the DNS cells better.

Simply taking the conditional average $\langle N|\eta\rangle$ of the DNS cells and the subgrid cells would overweight the subgrid solution compared to the DNS solution since the volume of the subgrid cells is much smaller compared to the DNS cells. Therefore the PDF

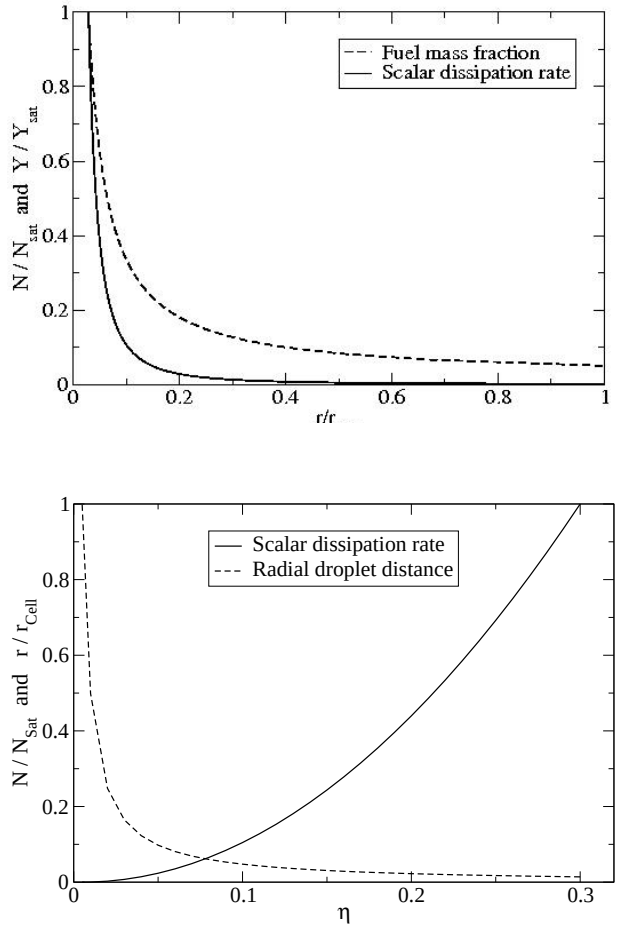

Figure 5.3: Top: Scalar dissipation rate N and fuel mass fraction Y_f vs radial distance to droplet r ($r_s/r_{Cell} = 0.05$). Below: Radial distance from droplet r and scalar dissipation rate N vs mixture fraction ξ. $\xi_S = 0.3$ and $\xi_{Cell} = 0.005$.

of the subgrid mixture fraction $P(\xi)_{Subrgid}$ is needed. This is established by assuming that the fuel vapor diffuses spherically away from the droplet as heat in the opposite direction. By discretising the subgrid mixture fraction field we can allocate with Eq. (5.11) a specific minimum and maximum radial distance, $r_1 = (r(\xi_i) + r(\xi_{i-1}))/2$ and $r_2 = (r(\xi_i) + r(\xi_{i+1}))/2$, for each 'mixture fraction bin' ξ_i. Figure 5.2 shows a volume shell of a mixture fraction bin defined by r_1 and r_2. Using

$$V(\xi_i) = \frac{4}{3}\pi \left(r_1^3 - r_2^3\right) \tag{5.14}$$

we get the volume $V(\xi_i)$ for each mixture fraction bin ξ_i around the droplet. Normalizing with the cell volume V_{Cell} we get a weighting factor

$$F(\xi_i) = V(\xi_i)/V_{Cell} \tag{5.15}$$

so that we can get $\langle N|\eta\rangle$ for all DNS cells and scalar dissipation model points in Figure 5.4.

A comparison of $\langle N|\eta\rangle_{DNS}$ and $\langle N|\eta\rangle_{DNS+Subrgid}$ for case C01 can be seen in Figure 5.5. Figure **??** shows the time evolution of $\langle N|\eta\rangle$ for case $C01$. With increasing time the average N_{Sat} of all droplets is moving to higher η due to the higher temperatures leading to a higher saturation mixture fraction ξ_S on the droplet surface. Hence at later time steps $\langle N|\eta\rangle$ has lower values in the mixture fraction space where the DNS grid cells are located.

5.4 Results

To validate the CMC equations extended to two-phase flows, as discussed in Chapter 3, 0D-CMC simulations are carried out based on the DNS cases $C01$ and $C02$ (See Table 6.1). Figure 5.6 and 5.7 show the reaction rate $\dot{\omega}_{MR}$ and $\dot{\omega}_{ST}$ conditional on $\eta_{MR} = 0.1$ and $\eta_{ST} = 0.062$ respectively, comparing the DNS results with the 0D-CMC results vs. time of case $C01$ and $C02$.

A relatively good agreement can be seen for the autoigniton time for both cases around η_{MR}. Without the subgrid model for N, the 0DCMC underpredicts N and hence give earlier ignition times. The reaction process prior to autoignition is in very good agreement while for $\tau/\tau_{ref} > 2.0$ the 0D-CMC simulations underpredict the reaction rate. At the peak of $\dot{\omega}_{MR}$ for the DNS case, $\dot{\omega}_{MR}$ of the 0D-CMC is lower by a factor of 1.4 for Case $C02$. Conditional on η_{ST} the 0D CMC solution gives less good agreement for case $C01$ when autoignition starts for. The difference between CMC

and DNS can be linked to the scalar dissipation model used. The assumption in Eq. (5.8) used for the model is only valid prior to reaction taking place. Using Eq. (5.8) while high reactions can lead to a overpredicted conditional scalar dissipation $\langle N|\eta\rangle$. Figure 5.8 takes various points in time during the autoignition process of case $C02$ and shows the reaction rate ω in mixture fraction space. Until $\tau/\tau_{ref} = 2.0$ the 0D-CMC and the DNS solution are in very good agreement. At early stages of the process the 0D CMC simulation slightly overpredicts ω at low values of η which can be also seen in Figure 5.9 in resulting to a lower level of Y_{O2}. At later time steps the 0D CMC solutions cannot follow the high reaction rates of the DNS simulation. This could be caused by the lower amount of oxygen available in the 0D CMC solution when autoignition starts to take place.

Figure 5.10 the conditional temperature for case $C02$ at the same time points. In the beginning the cooling effect of the droplet evaporation can be seen, introduced around ξ_S (evident in the figure at around $\eta = 0.1$). At later time steps the 0D CMC simulation underpredicts the temperature rise for $\xi > \xi_{MR}$ possibly due to the overprediction of $\langle N|\eta\rangle$ in the scalar dissipation subgrid model.

5.5 Conclusions

The predictions of 0D CMC simulations for autoignition times compared to DNS are in good agreement. Very good agreement can be seen prior to the occurrence of high reaction rate while the difference between 0D CMC and DNS later on can be due to the scalar dissipation model which overpredicts $< N|\eta >$ when reaction takes place. Since the cooling effect of the droplets in the gas temperature field can be seen in the beginning where the scalar dissipation model is valid, the good agreement between 0D CMC and DNS shows that the CMC equations and closure assumptions presented in Chapter 3 are representing the physics of droplet evaporation reasonably well.

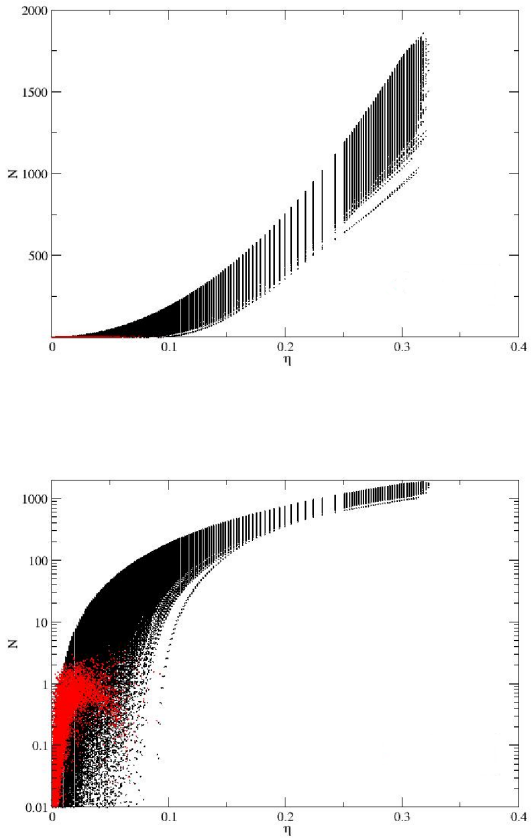

Figure 5.4: Top: Scatter plots of scalar dissipation rate in mixture fraction space taken at $\tau/\tau_{ref} = 0.64$. Red points denote DNS grid cells and black points are established from the scalar dissipation model for each droplet. Below: Same data on a logarithmic y-scale.

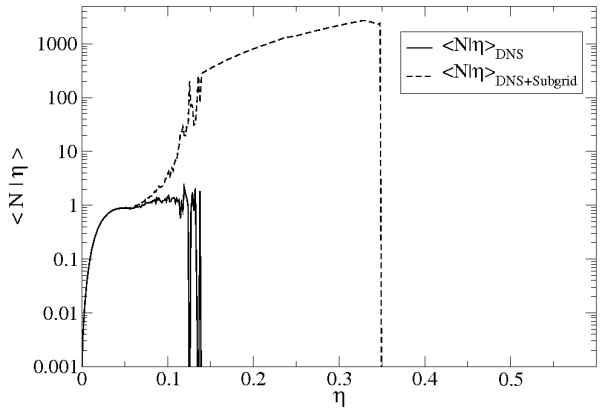

Figure 5.5: $\langle N|\eta\rangle$ for DNS grid cells (solid line) and for combination of DNS grids cells and subgrid model cells (dashed line), weighted by factor F of Eq. (5.15) at $\tau/\tau_{ref} = 0.64$.

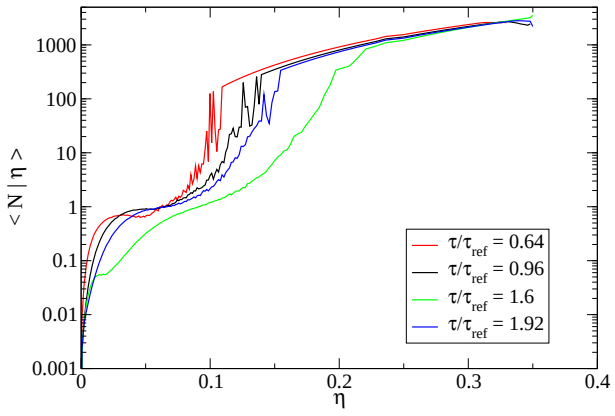

Figure 5.6: $\langle N|\eta\rangle$ for different time steps of case $C01$.

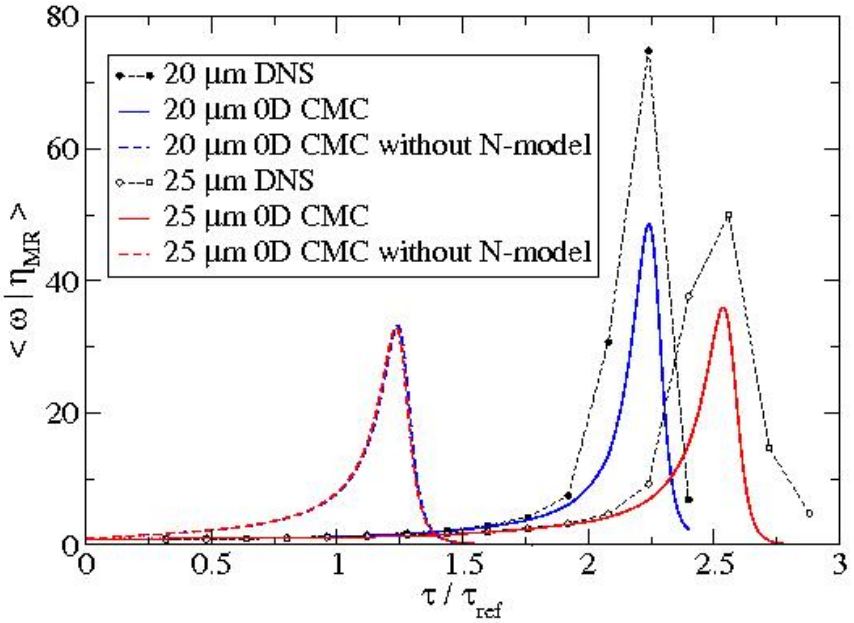

Figure 5.7: $\langle\omega|\eta_{MR}\rangle$ vs. time for case $C01$ and $C02$.

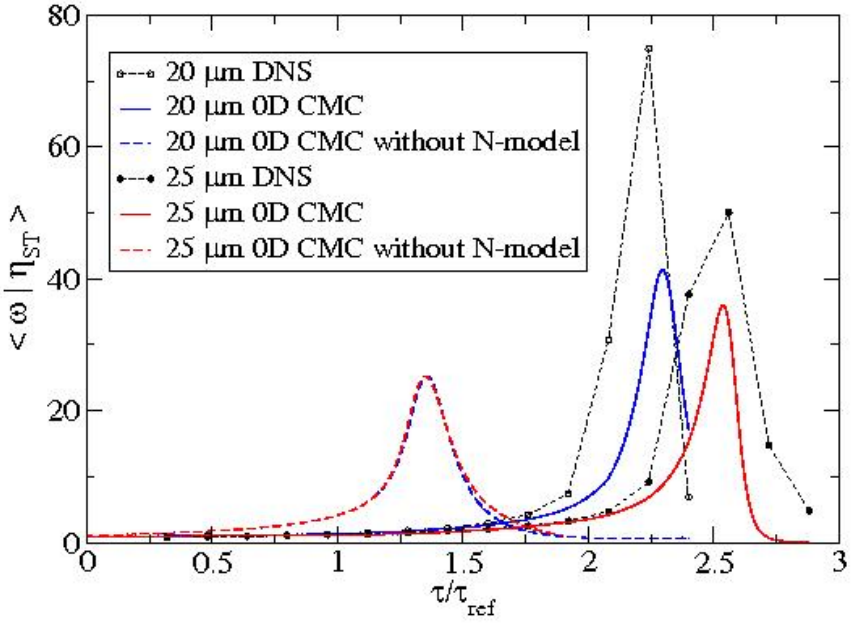

Figure 5.8: $\langle\omega|\eta_{ST}\rangle$ vs. time for case $C01$ and $C02$.

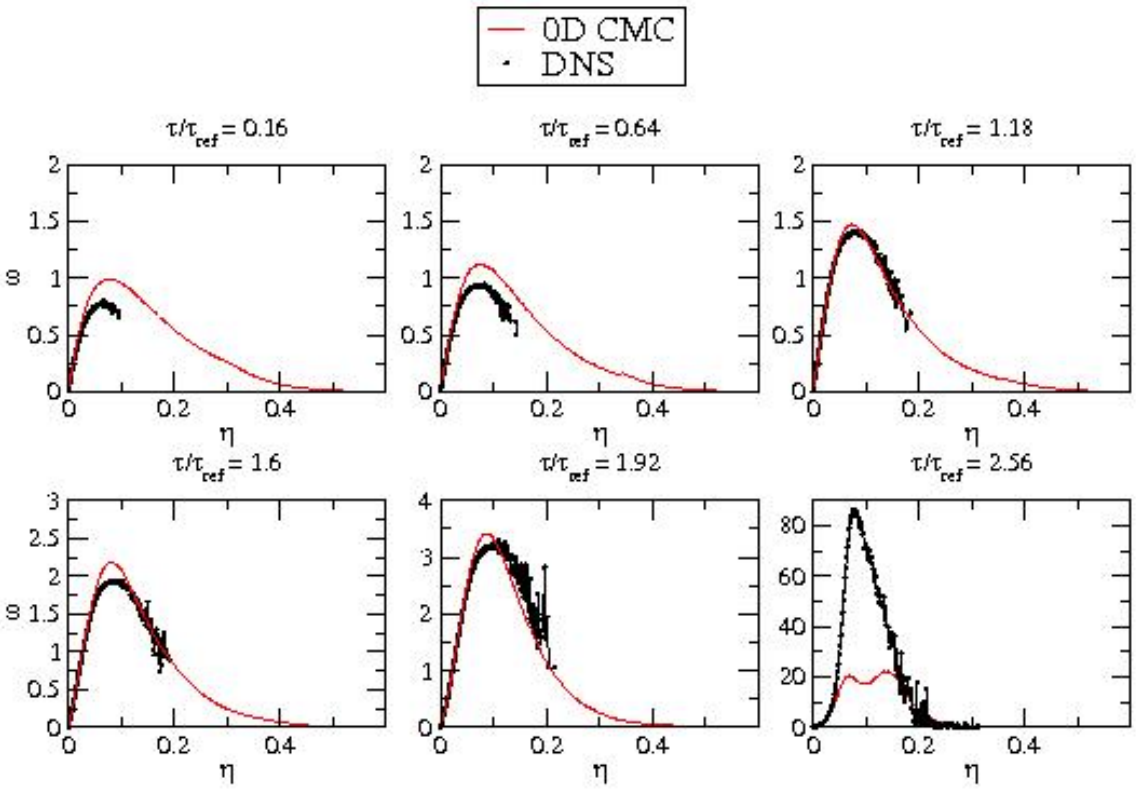

Figure 5.9: Comparison of reaction rate conditional on mixture fraction $\langle \omega | \eta \rangle$ vs τ / τ_{ref} for case $C02$. Red line denotes the zero dimensional CMC model extended to two-phase flow. Black dotted line denotes the DNS solution.

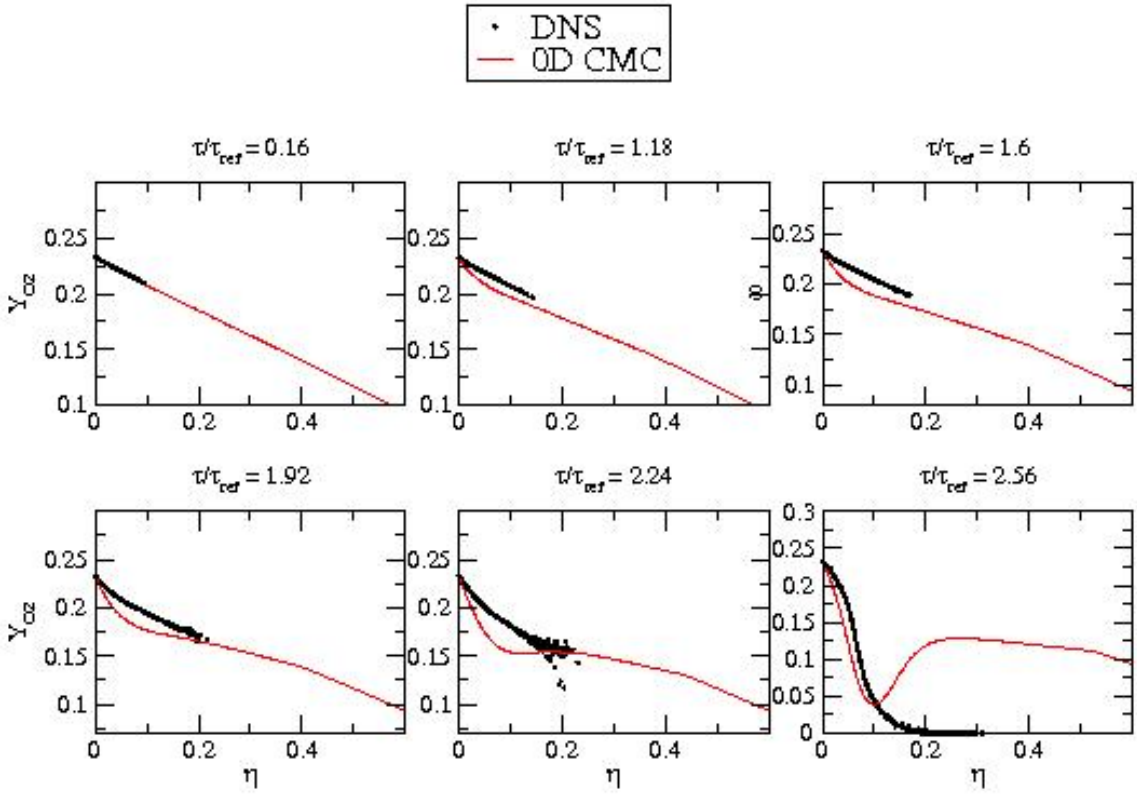

Figure 5.10: Comparison of oxidizer mass fraction conditional on mixture fraction $\langle Y_{O2}|\eta\rangle$ vs τ/τ_{ref} for case $C02$. Red line denotes the zero dimensional CMC model extended to two-phase flow. Black dotted line denotes the DNS solution.

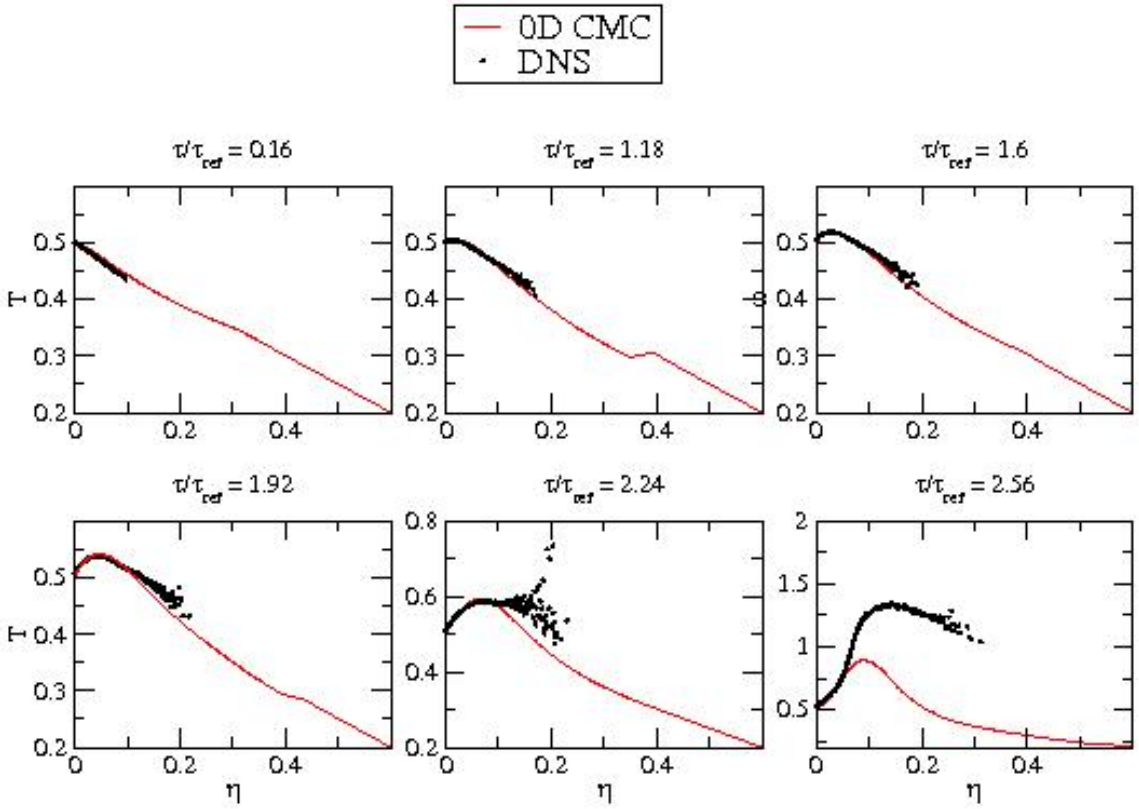

Figure 5.11: Comparison of temperature conditional on mixture fraction $\langle T|\eta\rangle$ vs τ/τ_{ref} for case $C02$. Red line denotes the zero dimensional CMC model extended to two-phase flow. Black dotted line denotes the DNS solution.

Chapter 6

Simulations of spark ignition of a swirling spray flame with 2D-CMC

In this chapter the CMC model extended to two-phase flow is applied to ignition of a swirling bluff body stabilized n-heptane spray fuelled flame. The predictions of the cold spray flow solution and of the spray flame are compared to experimental data [4]. Comparison of simulations of the CMC model, with and without extension to two-phase flow, for the flame establishment after spark ignition is carried out to examine the differences between the conventional model and the new one.

6.1 Background

The numerical simulation configuration presented here is based on the experimental study of spark ignition of a turbulent swirling n-heptane spray flame by Marchione et al. [4]. The burner configuration, using a bluff body to create a recirculation zone for stabilization of the flame, is widely used in engineering applications. This simple burner geometry creates a similar flow and combustion set up as those found in more complex industrial burner applications. On the other side its simple geometry makes it very attractive for experimental and numerical studies. The flow is axi-symmetric, creating an axial swirl after the bluff body, similar to flow patterns in aviation gas turbine combustors. Figure 6.1 illustrates the setup and its main features, including the combustor wall, the conical bluff body and the swirler device upstream of the bluff

body.

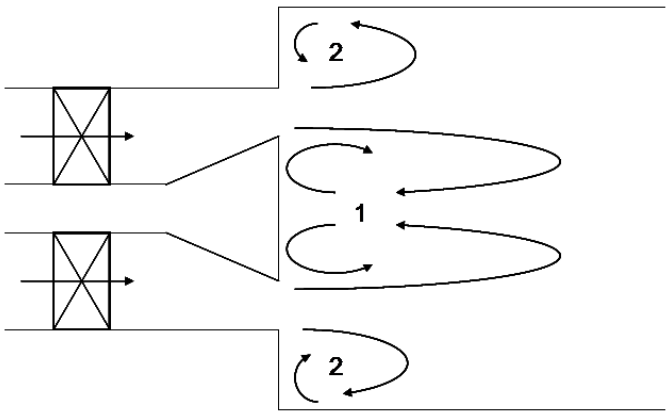

Figure 6.1: Schematic of bluff body burner configuration, including the inner (1) and outer (2) recirculation zones marked by arrows.

The resulting mean flow field of this configuration is expected to consist of several recirculating structures, a central recirculation zone (1) and an outer recirculating zone (2). For non-premixed use of the burner the fuel can be supplied through an internal pipe in the bluff body, in liquid or gaseous form, and introduced co-axial or orthogonal to the air flow. An axial fuel stream introduced into the air flow on the surface center of the bluff body is weakening the inner recirculation zone since they are opposed to each other [82], while radial injection of the fuel stream on the side of the bluff body will change velocity profile past the bluff body. The flame is generally initiated by a spark plug which is located downstream of the bluff body in the flow field where a flammable mixture is presented. A large amount of research has been performed to identify a suitable location for the spark kernel in the flow field for successful ignition [82; 86; 87].

6.2 CMC simulation setup

6.2.1 Flow configuration

The first order CMC model extended to two-phase flows is used to simulate the flame establishment after spark ignition of a turbulent swirling n-heptane spray flame us-

ing a single spark. Equations (3.75) and (3.76) govern the CMC model. The scalar dissipation model presented in Chapter 5 is not used here because it is based on the assumption of $Y_F \approx \xi$ which is valid only for autoignition problems. The complete burner geometry and geometry of the bluff body can be found in [4; 87]. A schematic of the burner is shown in Figure 6.2 and is taken from [4].

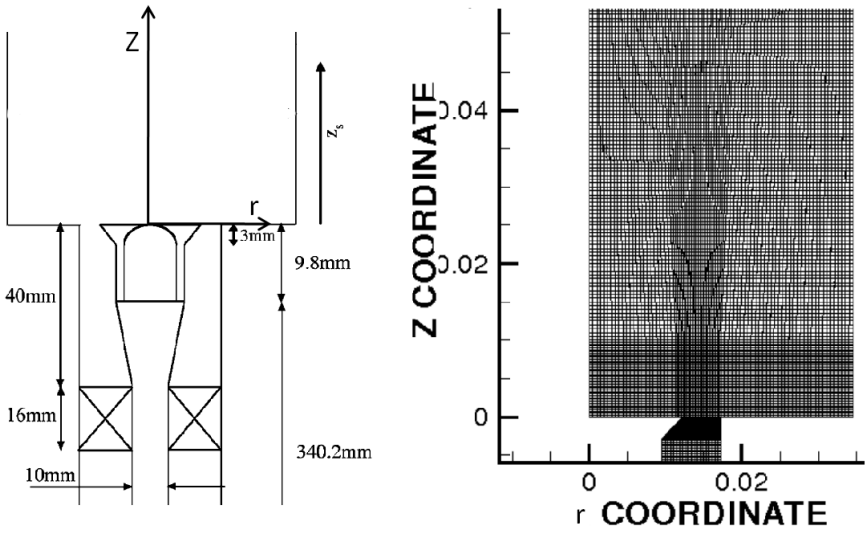

Figure 6.2: Schematic of burner from [4] (left) and block structured axi-symmetric grid (right).

Inside the inlet circular duct of 35mm diameter a conical bluff body of diameter $D_b = 25$mm, giving a blockage ratio of 50% is placed. Fuel is supplied by a fuel injection system positioned centrally in the bluff body, consisting of a pressure swirl hollow-cone atomizer creating a 60 degree spray angle. The air enters through the annular open area between the bluff body and the outer duct wall after passing a swirler. The air mass flow rate $\dot{m}_{air}$ and fuel mass flow rate $\dot{m}_{fuel}$ are 0.42kg/min and 0.025kg/min, respectively, resulting to a global equivalence ratio of 0.9. The fuel spray initial droplet size distribution $p(d)$ follows a Rossin Ramler distribution

$$p(d) = 1 - \exp\left(d/D\right)^q \tag{6.1}$$

where $D = 30\mu$m and $q = 2.55$ and $p(d)$ is approximated by 10 droplet size classes. All droplet parcels have the same initial velocity magnitude of 34.5m/s, given by the

nozzle diameter (0.15mm) and the volume flow rate $\dot{m}_{fuel}$. However due to the size distribution the differing drag forces will quickly create a non-uniform velocity distribution. In the experiment tungsten spark electrodes with a 1mm electrode thickness is used to establish ignition. The spark gap is 3mm using 200mJ of energy for a duration of 400μs.

Table 6.1 lists the different simulation set ups investigated in this paper. For comparison purposes two different simulation set-ups are used to investigate the impact of the extra droplet source terms in the CMC equations. Both set-ups are used at two dif-

Table 6.1: Table of cases.

Case	Spark location	CMC evaporation source terms
A	r=0mm z=23mm	ON
B	r=0mm z=23mm	OFF
C	r=15mm z=31.5mm	ON
D	r=15mm z=31.5mm	OFF

ferent spark locations in the flow field. Case A and B are located on the center axis of the burner 23mm downstream of the bluff body in the inner recirculation zone. Case C and D are at a radial displacement of 15mm from the central axis and 31.5mm downstream of the bluff body. The energy deposition of the spark is modelled by placing a burnt gas solution in the spark kernel area. For simplicity this will be called 'spark ignition' throughout this work.

6.2.2 Numerical approach

The commercial CFD solver STAR-CD [88] has been coupled with a CMC solver. A schematic of the coupling between the CFD and the CMC solver can be seen in Figure 6.3. The flow is solved by STAR-CD using a block structured grid, using a RANS formulation and the $k-\epsilon$ model for low Reynolds numbers.

The transport equations for the mean and variance of mixture fraction (Eq. (3.77), Eq. (3.78)) are calculated in STAR-CD with the droplet source terms supplied by a user subroutine. The built-in Lagrangian-Eulerian formulation between liquid and gas

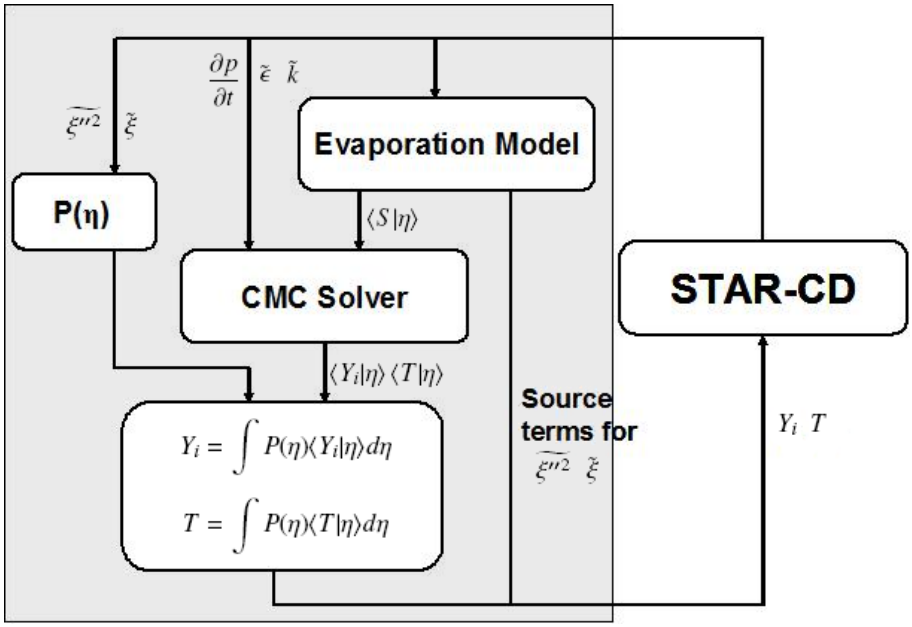

Figure 6.3: Schematic of the STAR-CD CMC coupling and the droplet evaporation subroutine. The grey underlaid area highlights the FORTRAN subroutines used in the coupling.

phase is used with the Reitz-Diwakar model [89] for droplet atomization. The thermophysical droplet properties are supplied by a user subroutine. The species mass fraction and temperature equations are not solved in STAR-CD, as they are computed by the CMC solver. The species mass fractions and temperature returned to STAR-CD are obtained in the CMC solver by integrating the conditional averages over $P(\eta)$. Therefore transport equations for $\tilde{\xi}$ and $\widetilde{\xi''^2}$ (Eq. (3.77), Eq. (3.78)) have to be solved by STAR-CD to establish a presumed PDF of mixture fraction. The droplet evaporation source terms in Eq. (3.75), Eq. (3.76), Eq. (3.77) and Eq. (3.78) are supplied by a user subroutine which loops for each time step over all droplet parcels and creates the droplet source terms, using the evaporation model as described above (2), and returns them to STAR-CD for the next iteration step. The conditional droplet source term $\langle S|\eta\rangle$ is established by this subroutine as well and is supplied to the CMC solver.

The CMC equations (Eq. (3.75), Eq. (3.76)) are discretized using finite differences with 81 nodes in conserved scalar space, clustered around the stoichiometric value to enhance local resolution. To reduce the number of simultaneously solved ODEs, op-

erator splitting (OS) was used, separating the chemical part of the system from the convection and diffusion part. The evaporation source terms are computed together with the reaction and diffusion in mixture fraction space, after the computational step of the physical space convection and diffusion. Integration of the ODEs is done with the VODPK solver [90; 91].

The 2D axisymmetric block-structured CFD grid is shown on the r.h.s. of Figure 6.2 and consists of 22820 cells. The overlaying CMC mesh consists of 40 cells in radial and 80 cells in axial direction, ensuring that at least one CFD cell is located in each CMC cell. For both CFD and CMC mesh, the grid size in the recirculation zone near the bluff body is refined. The axial minimum cell dimension is $\delta Z_{min} = 0.8mm$ and $\delta R_{min} = 0.75mm$ in radial direction. For all simulations the timestep is $\Delta t = 5\mu s$.

Reaction rates are calculated by a modified one-step chemistry for heptane [9], developed by the method of Tarrazo-Fernandez et al. [5] for partially premixed combustion. This method is based on a tuning of the heat release rate as a function of the local equivalence ratio in order to produce the correct adiabatic flame temperature, which results in a substantial improvement in the prediction of the laminar burning velocity of premixed flames at all flammable values of equivalence ratio. For non-premixed combustion, the methods results in flame temperatures and extinction strain rates that are comparable to those from the detailed mechanism. Figure 6.4 shows conditional temperature and mass fraction profiles for fuel and oxygen for different peak values of scalar dissipation.

6.3 Cold flow solution

Contour plots of the mean axial and swirl velocity of a steady state solution before spray injection are shown in Fig. 6.5. The contour plot of the axial velocity shows a recirculation zone above the bluff body as expected. The outer counter recirculating zone is also visible in the axial velocity contour plot. The contour plot of the mean swirl velocity shows the swirl produced by the swirler in the radial pipe section upstream of

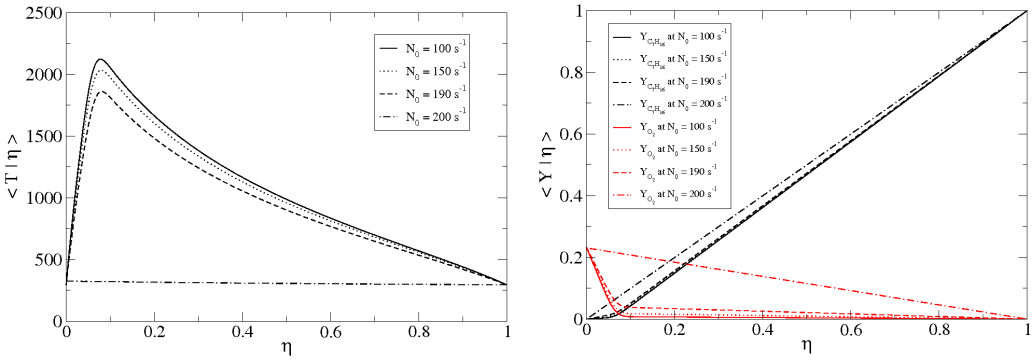

Figure 6.4: Conditional temperature (left) and mass fraction (right) profiles for different N_0 from use of the 1-step n-heptane mechanism [5].

the bluff body, forcing the bulk of the inflow to bend towards the burner wall.

Predicted and measured radial profiles of the mean of the axial and swirl velocity are shown in Fig. 6.6 at several axial positions. In general both the predicted axial and swirl velocities are in good agreement with the experiment. Radial profile predictions for both velocities are slightly more over predicted further upstream than in the proximity of the bluff body.

Figure 6.7 shows a comparison of the spray droplet distribution after the fuel atomizer is launched, between experiment and simulation. The bluff body, for both images, is located on the bottom. The spray is injected through the bluff body into the recirculation zone. Some of the droplets are trapped and stay in the recirculation zone while a certain amount break through and enter the axial air flow and impinge on the combustor wall and carried away downstream. There is a relatively good agreement of the spray cone angle (55-65 degrees) between experiment and simulation. The impact of the droplet momentum on the flow field can be seen Fig. 6.8. The introduction of the spray at the bluff body surface weakens the negative velocity in the recirculation zone, creating a positive axial air velocity. The liquid fuel spray will be able to penetrate deeper the gaseous flow field.

The evaporation of the fuel droplets will cool down the surrounding air where they are located. The cooling effect of the spray near the bluff body can be seen in Figure

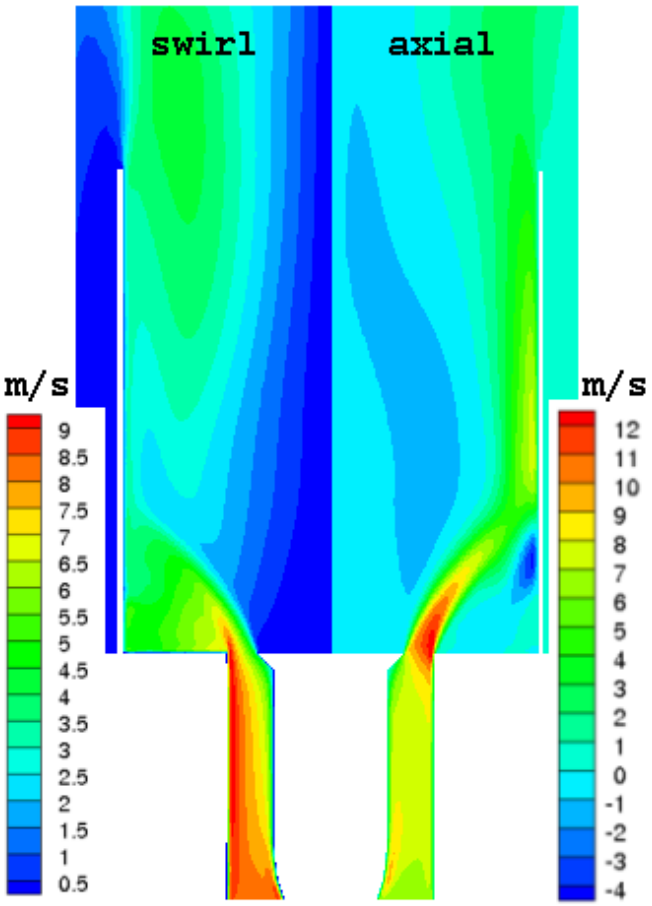

Figure 6.5: Contour plot of axial (right) and swirl (left) mean velocity of the cold flow in absence of spray.

6.9. At locations with high evaporation the local temperature is reduced by $3 - 4K$. Further downstream of the bluff body the effect of droplet evaporation is minimal and hence no drop in temperature is visible.

To get a better insight into the cooling effect of the droplets, Figure 6.10 shows temperature profiles conditional on mixture fraction. As explained in Chapter 3 evaporation is assumed to take place on the droplet surface, hence in mixture fraction space at the saturation mixture fraction ξ_S on the droplet surface. For ambient temperature of $T_a = 293$ this results in $\xi_S \approx 0.19$. The cooling at ξ_S can be seen in both graphs of Figure 6.10 for different axial and radial locations in the cold spray flow. Near the

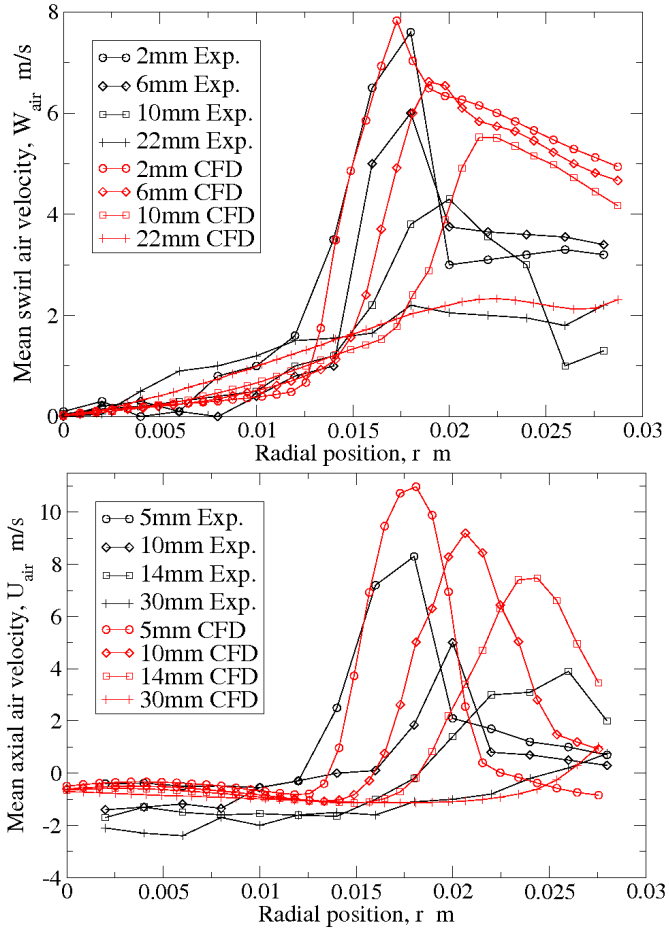

Figure 6.6: Predicted and measured radial profile of mean swirl (top) and axial (bottom) velocity for air flow in absence of spray at the indicated axial positions. Experimental data from Ref. [4].

centerline (left graph) a stronger cooling effect is seen near to the bluff body, while off the radial center line (right graph) more cooling is seen slightly downstream which is due to the conical spray. At locations further downstream of the bluff body the cooling effect in the conditional temperature profile is broadened due to the non-uniform droplet temperature depending on the droplet history in the flow.

Figure 6.11 shows the distribution of the Droplet Sauter Mean Diameter (SMD) at different axial distances downstream of the bluff body. A fairly good agreement between experiment and simulation nearer to the bluff body can be observed while more

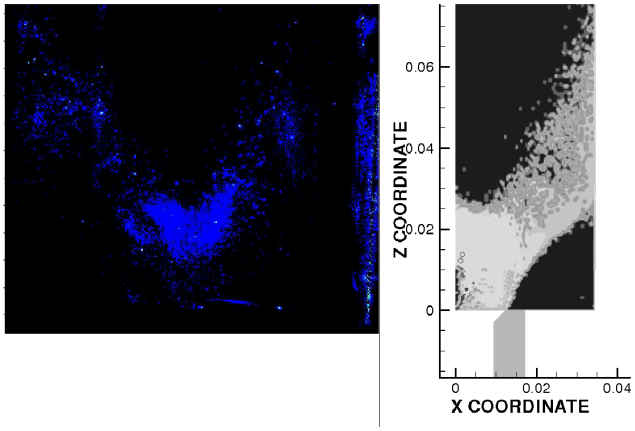

Figure 6.7: Comparison of the experimental (left) and simulation (right) droplet distribution within the cold spray flow.

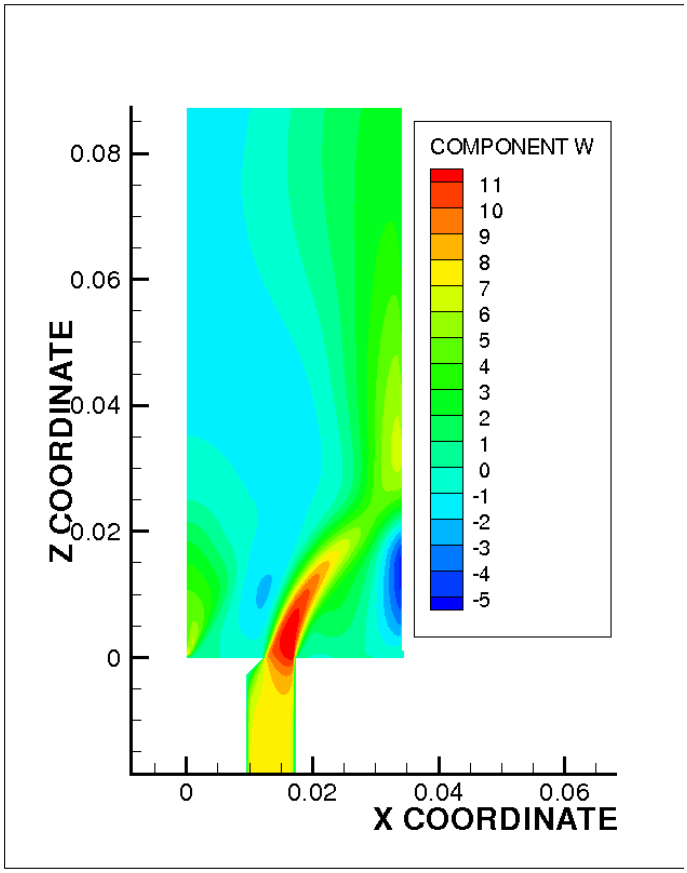

Figure 6.8: Contour plot of axial mean velocity of the cold spray flow.

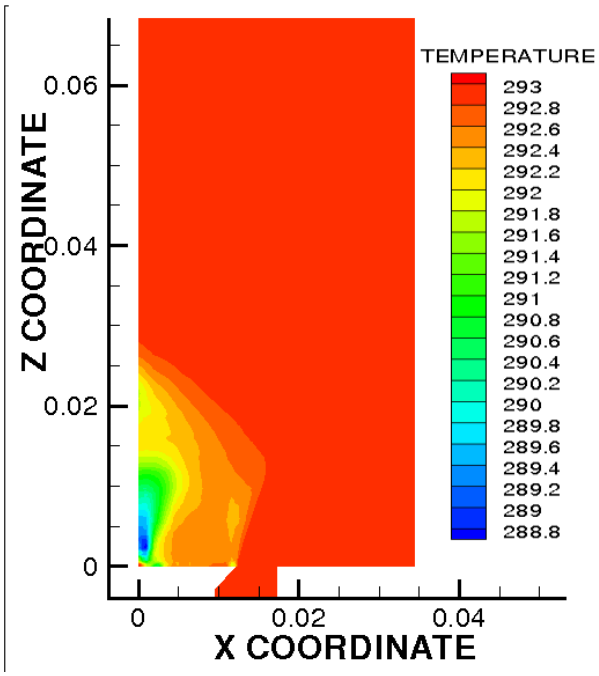

Figure 6.9: Contour plot of mean temperature for cold spray flow before spark ignition.

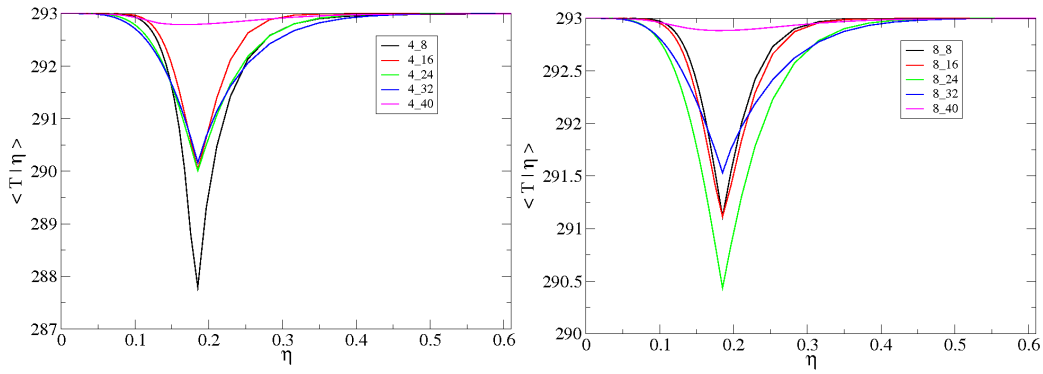

Figure 6.10: Temperature profiles conditional on mixture fraction for different axial and radial locations of the cold spray flow.

downstream the simulated SMD is over predicted. The high scattering of the SMD in the simulation is due to the low number of droplet parcels.

The evaporating droplets create an air-fuel mixture which is visualized by the mean

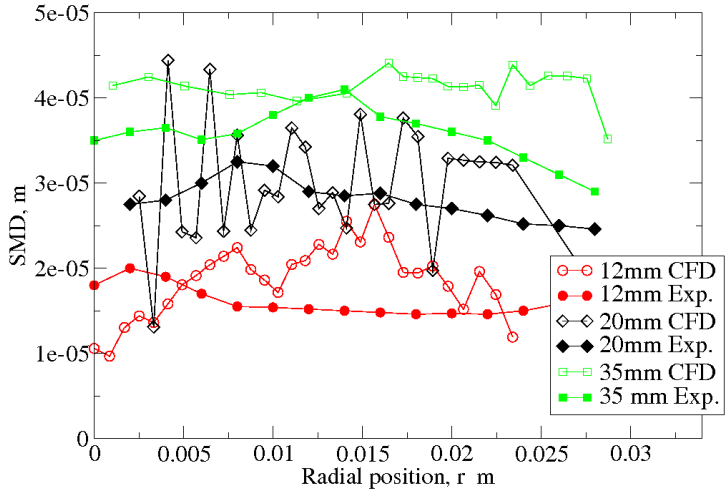

Figure 6.11: Distribution of the Droplet Sauter Mean Diameter (SMD) at different axial distances downstream of the bluff body.

and variance of mixture fraction in Figure 6.12. The mean mixture fraction reaches $\overline{\xi} \approx 0.18$ in the recirculation zone near to the spray nozzle. This region is also relatively well mixed, since the variance of mixture fraction is very low for this region. Surrounding the recirculation zone is a turbulent mixing layer, visible by the high values of the variance of mixture fraction. The white line in the mean mixture fraction contour plot denotes the stoichiometric line for heptane.

6.4 Spark ignition

Figure 6.13 shows a comparison of Favre averaged temperature contours of case A with high-speed images from Ref. [4] at four different time steps after spark ignition. The bluff body is at the bottom of these images in the center. A good qualitative agreement in the time evolution of the flame can be observed between simulation and experiment.

The development of the flame after spark ignition can be seen in Figure 6.14, where contour plots of temperature for case A are shown at six different time steps after spark ignition from (a) at $t = 0.3$ms to (f) at $t = 16.5$ms. The location of the spark is at $r = 0mm$ and $z = 23mm$ into an area of the flow with relatively high mean mixture

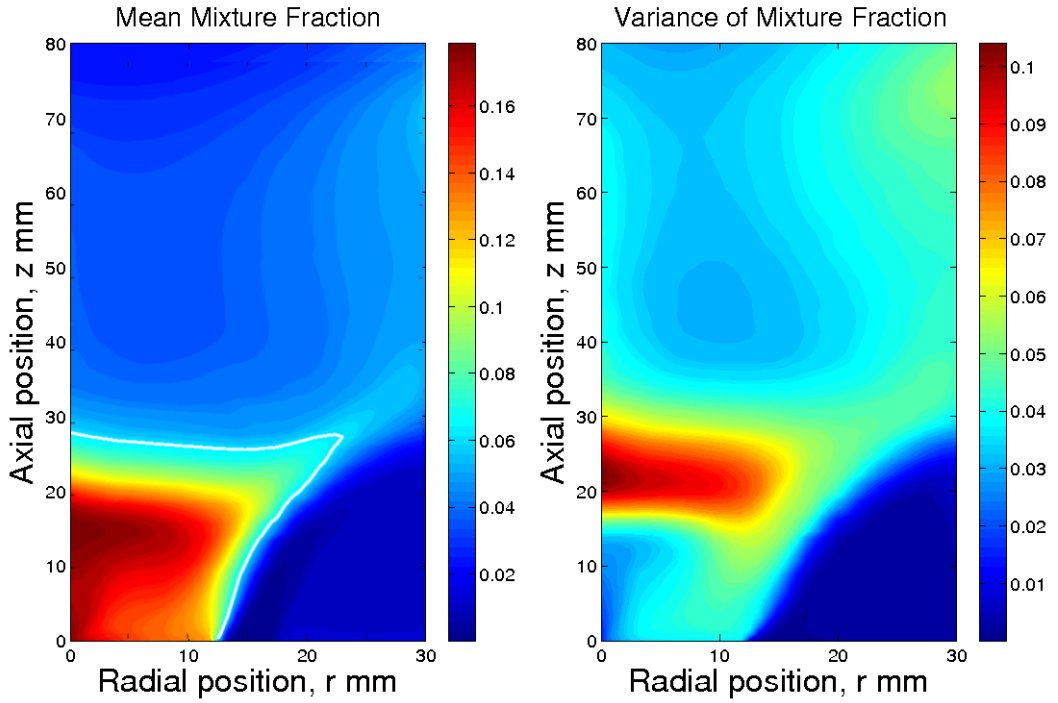

Figure 6.12: Contour plot of mean mixture fraction (left) and variance of mixture fraction (right) of cold spray flow. The white line in the mean mixture fraction contour plot denotes the stoichiometric line for heptane.

fraction level. In the first three contour plots shortly after spark ignition ((a), (b) and (c)) show the high temperature at the initial spark area. Due to the high temperature rise in this area the cooling effect near to the nozzle by spray can be observed in these contour plot but is still presented as in Figure 6.9. At $t = 7.1$ms (d) the flame kernel grows into the surrounding flow and subsequently during $t = 13.5$ms to $t = 16.5$ms the flame is established.

Figure 6.15 shows contour plots of the mean axial velocity at the same time steps as in Figure 6.14. The main air stream of air delivered from the swirler pipe can be seen clearly throughout all contour plots as well as the outer counter recirculating zone. In the inner recirculation zone, the air flow is strongly affected by the spray flow injected at the bluff body surface and initially by the spark ignition kernel. Since the spray flow is directed in downstream direction the inner recirculation zone gets weakend near the bluff body zone. At time steps $t = 13.5$ms to $t-16.5$ms in the region of the combustion

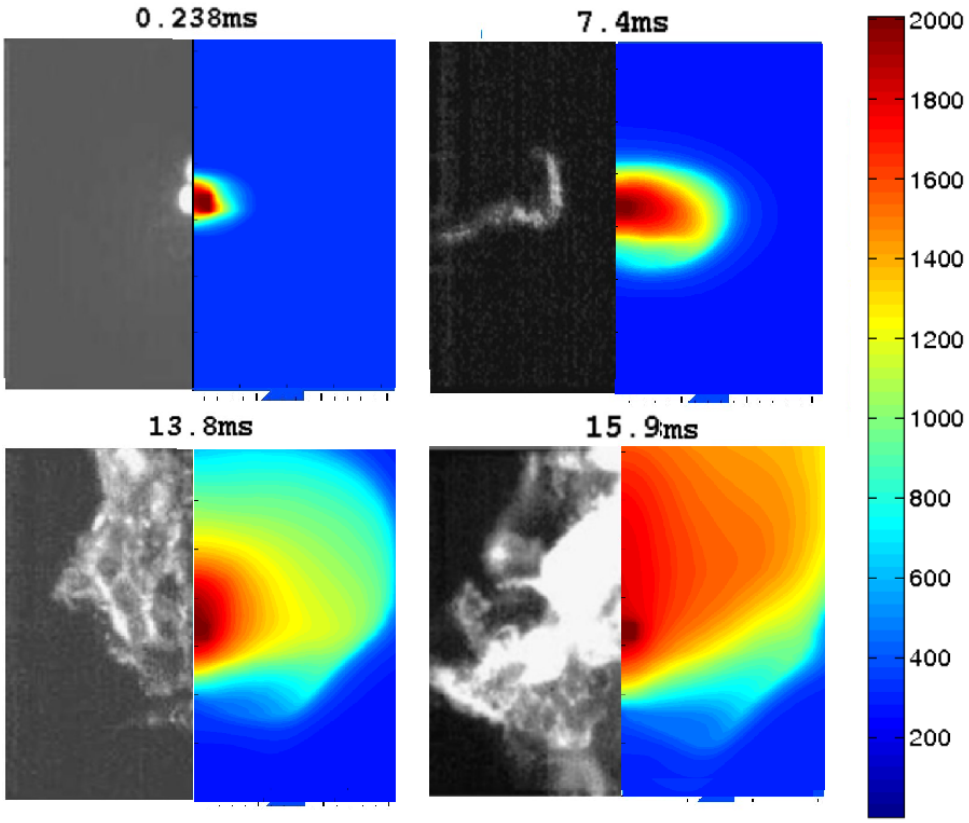

Figure 6.13: Comparison between contour plots of temperature for case A and high-speed images [4] at different time steps. Initial spark kernel location at $r = 0mm$ and $z = 23mm$ and image domain $70x50$mm.

chamber where the flame is established the flow field is accelerated.

For case A Figure 6.16 shows contour plots of the mean mixture fraction at the same time steps as in Figure 6.14 and 6.15. In all plots the white line denotes the stoichiometric mixture fraction ξ_{St}. As seen in Figure 6.12, a non-zero mixture fraction is established near the bluff body due to the droplet evaporation within the fuel spray flow initially before spark ignition. Initially, shortly after spark ignition a rise in $\widetilde{\xi}$ can be seen in the area of the initial spark kernel which is due to the higher rate of evaporation of the droplets in this region since the higher temperature increases the saturation mixture fraction ξ_S. The maximum of the mixture fraction rises up to levels of $\xi = 0.8$ to $\xi = 0.9$ during the establishment of the flame. The higher levels of ξ

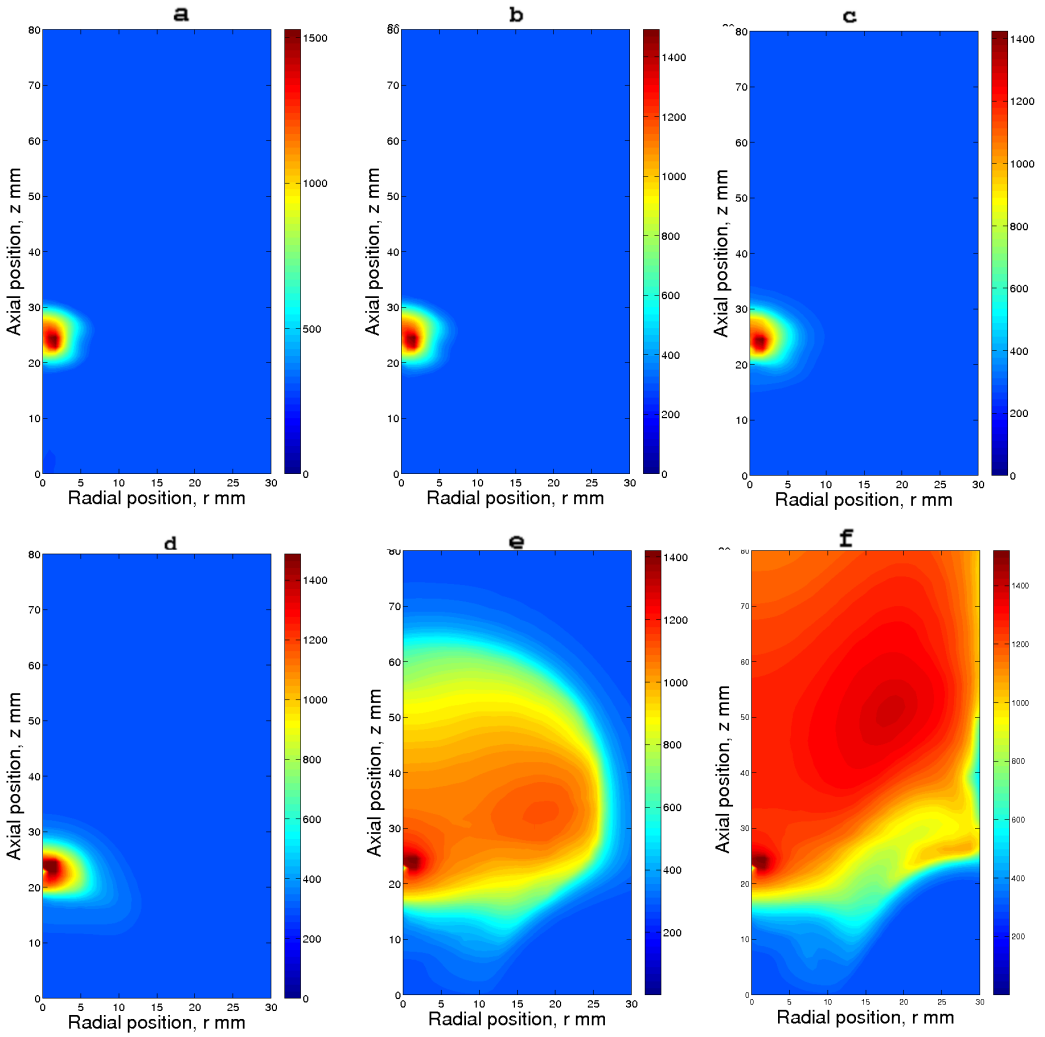

Figure 6.14: Contour plots of temperature for case A after spark ignition. Initial spark kernel location at $r = 0mm$ and $z = 23mm$ and image domain $70x50$mm. (a) at $t = 0.3$ms, (b) at $t = 0.7$ms, (c) at $t = 1.9$ms, (d) at $t = 7.1$ms, (e) at $t = 13.5$ms and (f) at $t = 16.5$ms.

can be seen in later time steps ($t = 13.5$ms, 16.5ms) in regions of the spray where the flame raised the temperature. The region with the highest levels of $\widetilde{\xi}$ can be found at a certain distance to the bluff body. Nearer to the bluff body the flame is not so well established and also more droplets are available for evaporation so that the resulting mean evaporation rate in this area is lower than more downstream. But it should be mentioned that the total amount of evaporation could be still higher in this area than in

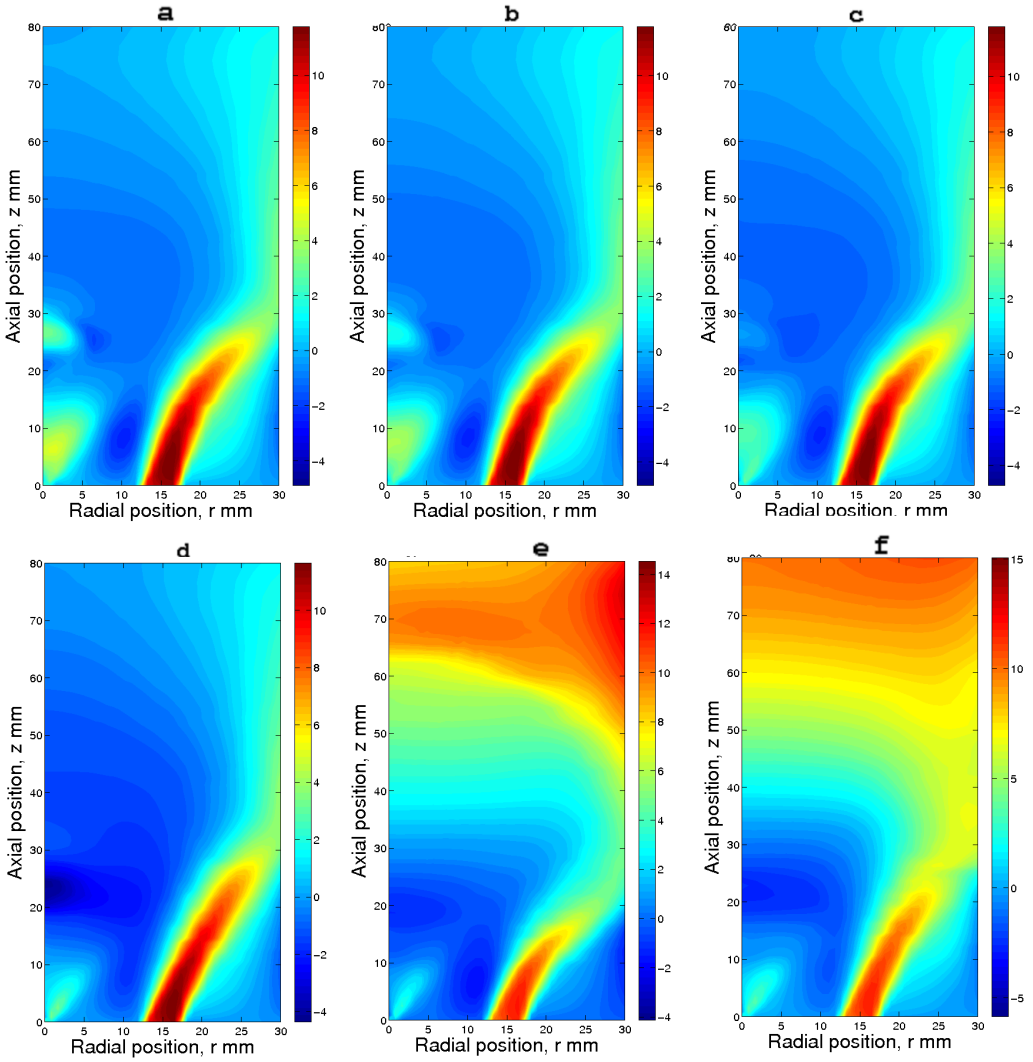

Figure 6.15: Contour plots of mean axial velocity for case A after spark ignition. Initial spark kernel location at $r = 0mm$ and $z = 23mm$ and image domain $70x50$mm. (a) at $t = 0.3$ms, (b) at $t = 0.7$ms, (c) at $t = 1.9$ms, (d) at $t = 7.1$ms, (e) at $t = 13.5$ms and (f) at $t = 16.5$ms.

the region with the highest level of mean mixture fraction.

For case A Figure 6.17 shows contour plots of variance of mixture fraction at the same time steps as in Figure 6.14, 6.15 and 6.16. Initially short after spark ignition a rise in the variance of mixture fraction can be seen upstream and downstream around

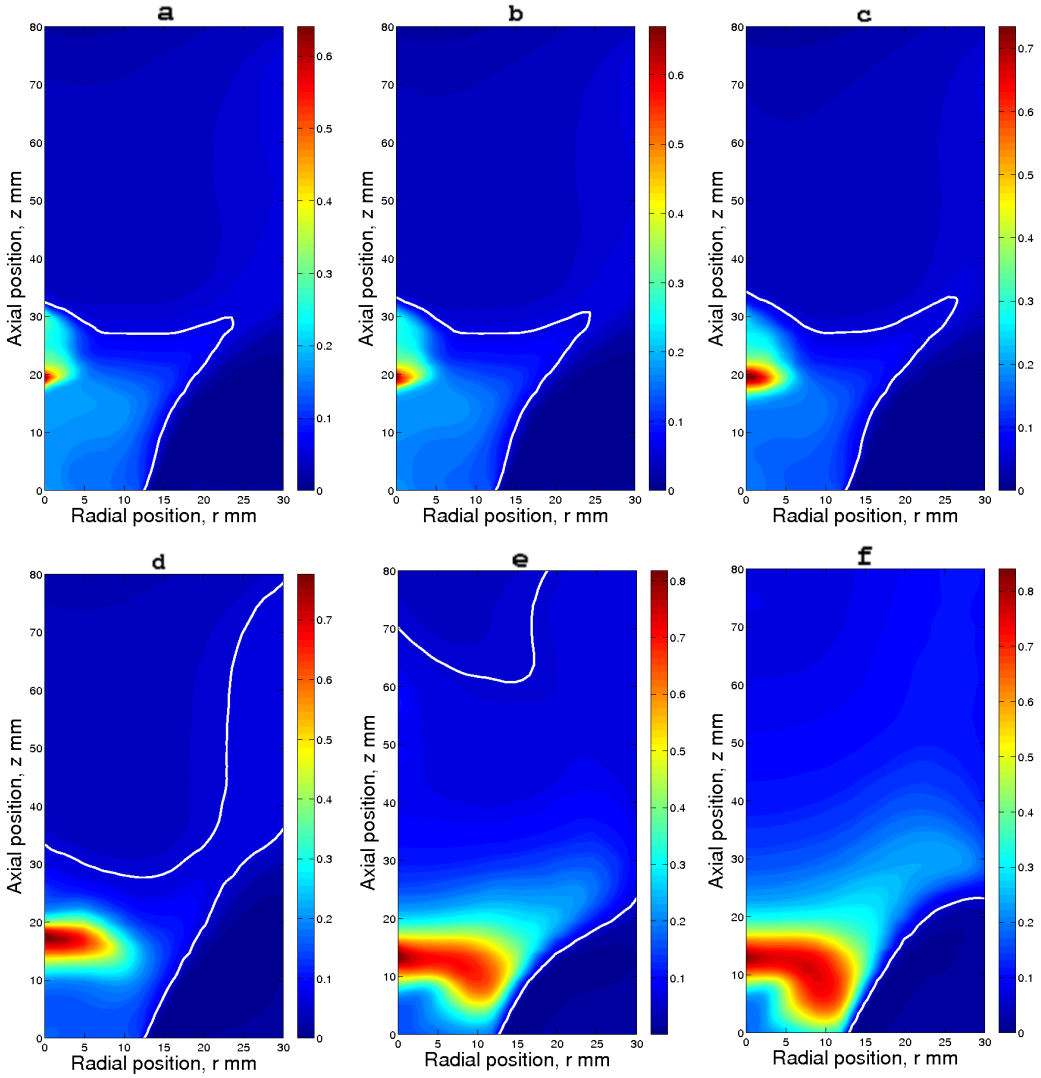

Figure 6.16: Contour plots of mean mixture fraction for case A after spark ignition. Initial spark kernel location at $r = 0mm$ and $z = 23mm$ and image domain $70x50$mm. White lines denote the stoichiometric mixture fraction ξ_{St}. (a) at $t = 0.3$ms, (b) at $t = 0.7$ms, (c) at $t = 1.9$ms, (d) at $t = 7.1$ms, (e) at $t = 13.5$ms and (f) at $t = 16.5$ms.

the spark kernel while the region of the spark kernel shows no increase. At later stages of the flame expansion higher levels of the variance of mixture fraction can be seen in the same areas as before for the mean mixture fraction (6.16).

To get a better insight of the droplet evaporation effect in the conditional temper-

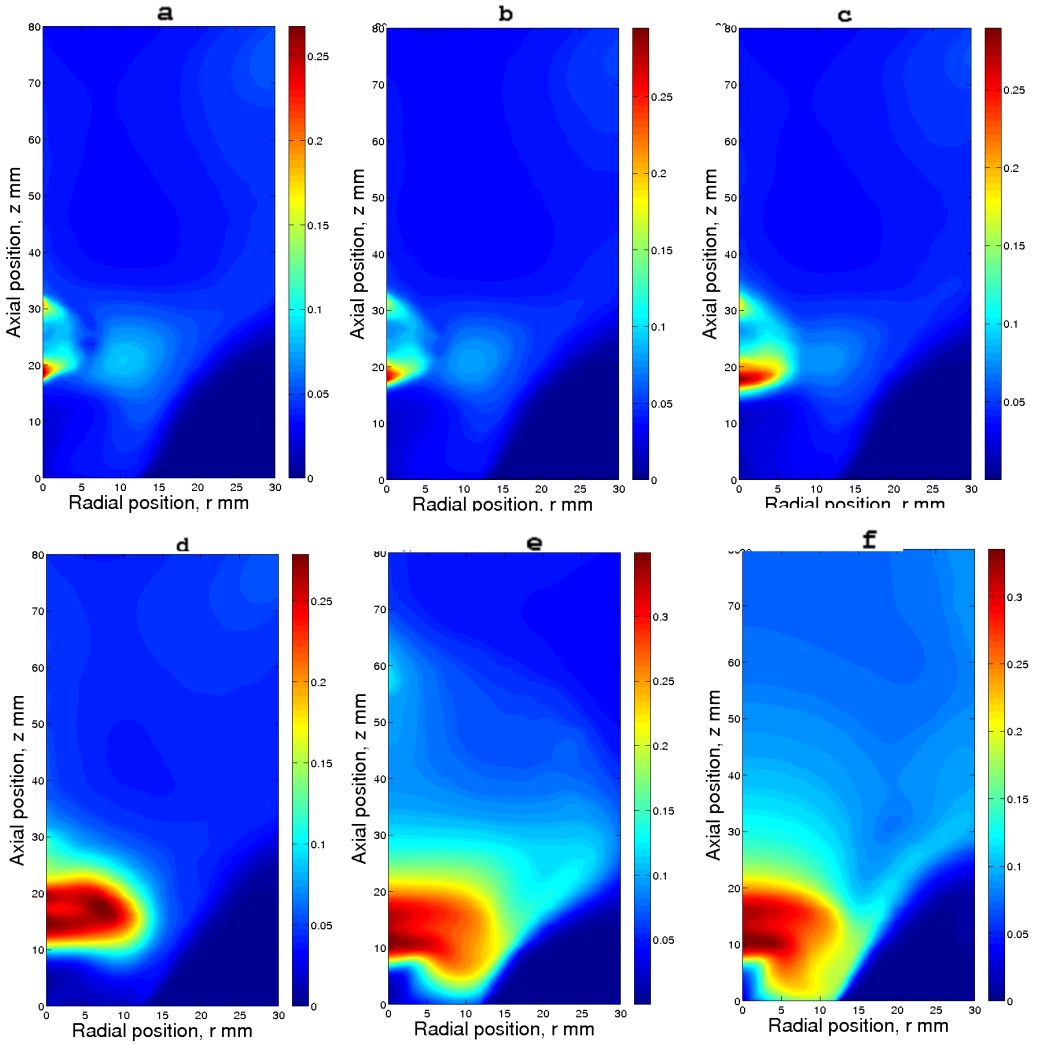

Figure 6.17: Contour plots of variance of mixture fraction for case A after spark ignition. Initial spark kernel location at $r = 0mm$ and $z = 23mm$ and image domain $70x50$mm. (a) at $t = 0.3$ms, (b) at $t = 0.7$ms, (c) at $t = 1.9$ms, (d) at $t = 7.1$ms, (e) at $t = 13.5$ms and (f) at $t = 16.5$ms.

ature and mass fraction equation between case A and B, Figures 6.18 and 6.19 shows contour plots of the temperature difference ΔT be together with $\Delta\widetilde{\xi}$, the difference of the mean mixture fraction between both cases. Near the bluff body, where the spray is introduced, the cooling effect of the extra droplet source terms in case A can be seen. In the initial location of the spark, case A shows slightly higher temperatures in

the beginning of the flame establishment while upstream of the initial spark location a region is visible with a strong cooling effect in case A since here a high amount of droplets is located.

In the development of the flame it can be seen that in downstream direction of the initial spark kernel the flame front of case A is growing faster than case B, visualized by the higher temperature of case A. The comparison of $\widetilde{\xi}$ between case A and B shows that near the bluff body at the spray injection ξ is lower in case A due to the cooling effect which lowers the evaporation rate. In the initial spark location and downstream case A shows higher level of ξ since here less droplets are available and so the cooling effect is weaker than the effect of the additional mass fraction source term in mass fraction CMC equation. To get a better insight, Figures 6.21, 6.22 and 6.23 show for several locations in the flow field the conditional temperature profile $\langle T|\eta\rangle$ of case A and B for three different times. The chosen locations are marked in the temperature contour plots of case A in Figure 6.20. In radial direction contour plots are taken at three locations, at $r = 2.2$mm, $r = 5.8$mm and $r = 9.0$mm. At these radial positions contour plots are taken at the following axial distances from the bluff body: $z = 12.00$mm, $z = 18.00$mm, $z = 26.00$mm and $z = 33.00$mm.

In Fig. 6.21 (0.238ms) the cooling effect around ξ_S in case A (red dotted line) can be seen in all locations while in locations nearer to the bluff body the effect is larger since more droplets are present. In locations near to the downstream side of the initial spark kernel case B shows higher $\langle T|\eta\rangle$ compared to case A while on the upstream side this effect is reversed.

At a later time step, shown in Figure 6.22, the rise of the conditional temperature profiles for case B is further advanced than in case A, where in case A the cooling effect of the droplet evaporation at ξ_S is still present. At locations near to the bluff body the conditional temperature profiles of case A are higher than in case B.

Figure 6.23 shows $\langle T|\eta\rangle$ at $t = 13.8$ms where the flame has expanded further. At locations around the initial spark ignitions the conditional temperature profiles for both cases have reached their fully burned solution with a peak peak in $\langle T|\eta\rangle$ around

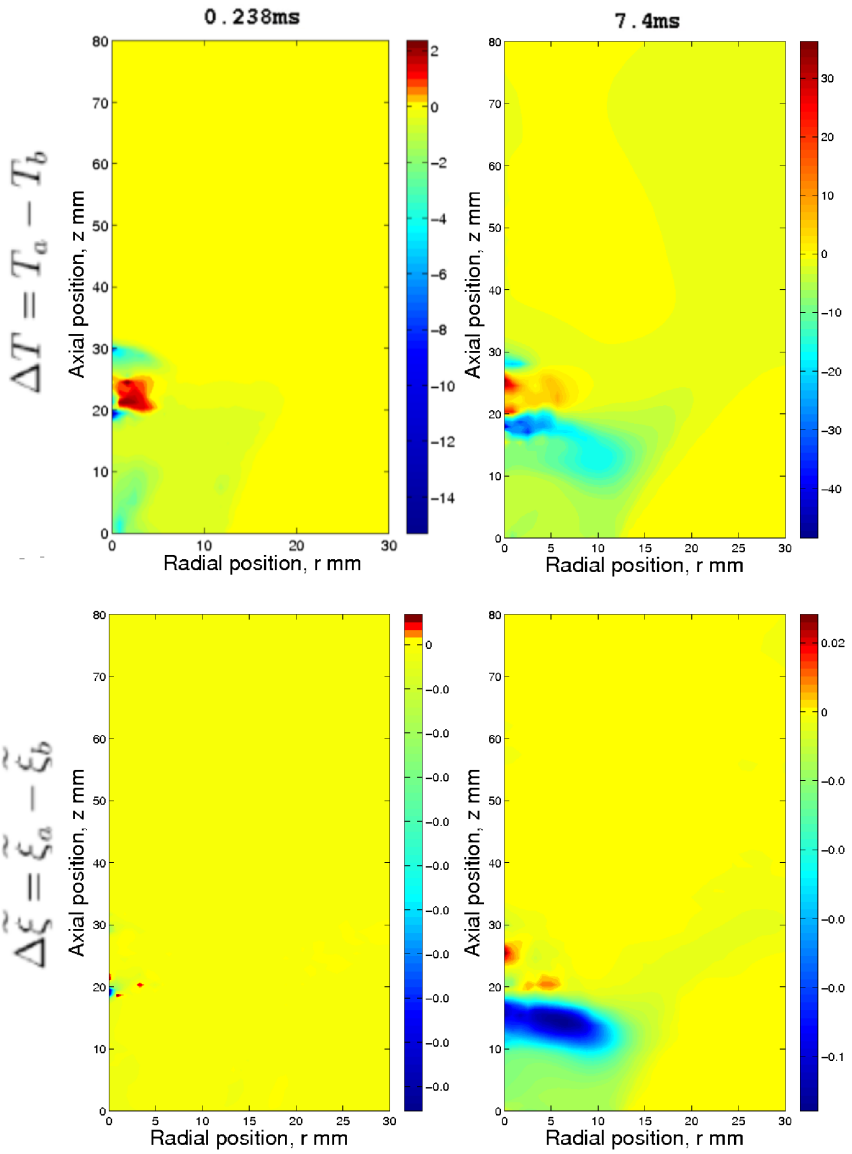

Figure 6.18: Upper: Contour plots of temperature difference $\Delta\widetilde{T}$ between case A ($\widetilde{T}_a$) with and case B ($\widetilde{T}_b$) without extra droplet source terms in the CMC equations. Lower: Contour plots of mean mixture fraction difference $\Delta\widetilde{\xi}$ between case A ($\widetilde{\xi}_a$) with and case B ($\widetilde{\xi}_b$) without extra droplet source terms in the CMC equations. For both $\Delta\widetilde{T}$ and $\Delta\widetilde{\xi}$ contour plots are shown at $t = 0.238$ms and $t = 7.4$ms.

the stoichiometric value of heptane. Here due to the lower number of droplets in this location, almost no droplets are available for evaporation and hence there is just a

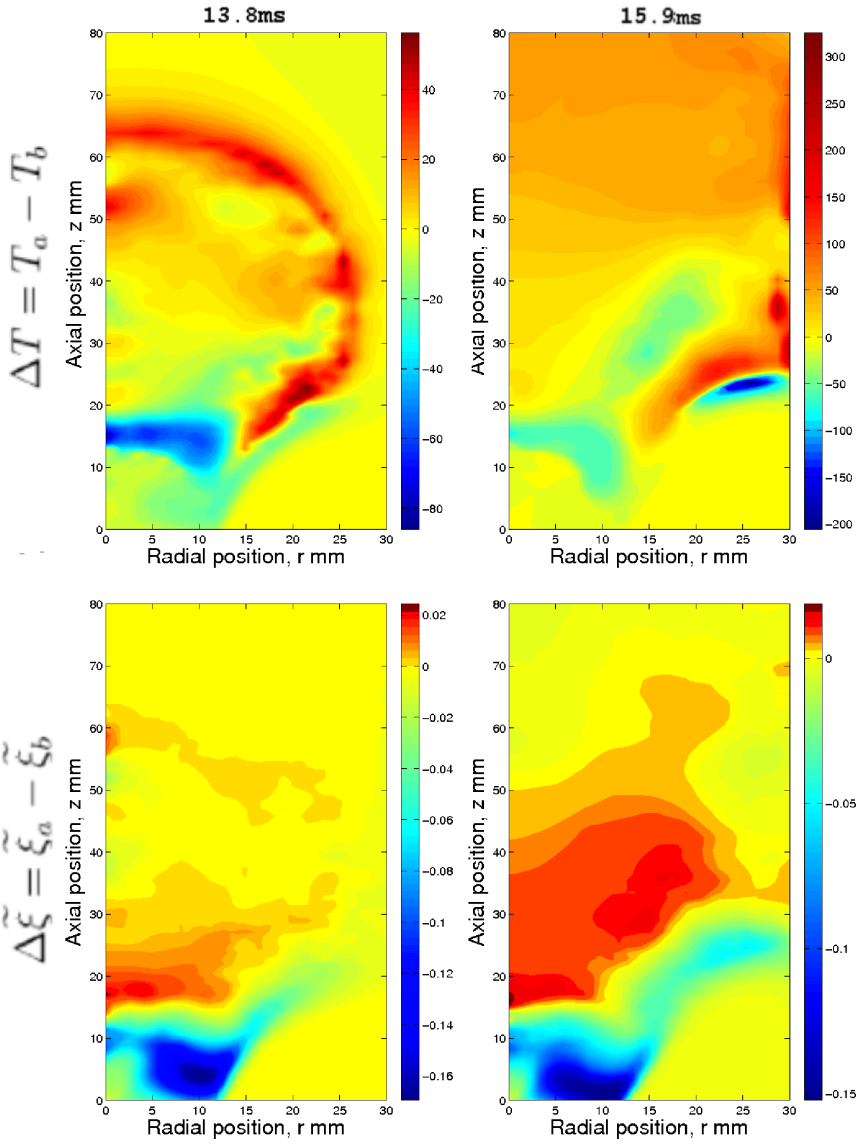

Figure 6.19: Upper: Contour plots of temperature difference $\Delta\widetilde{T}$ between case A ($\widetilde{T}_a$) with and case B ($\widetilde{T}_b$) without extra droplet source terms in the CMC equations. Lower: Contour plots of mean mixture fraction difference $\Delta\widetilde{\xi}$ between case A ($\widetilde{\xi}_a$) with and case B ($\widetilde{\xi}_b$) without extra droplet source terms in the CMC equations. For both $\Delta\widetilde{T}$ and $\Delta\widetilde{\xi}$ contour plots are shown at $t = 13.8$ms and $t = 15.9$ms.

minimal cooling effect visible in case A. $\langle T|\eta\rangle$ for case A is lower than case B on the rich side of ξ_S. Near to the bluff body, case A shows higher values $\langle T|\eta\rangle$ while for

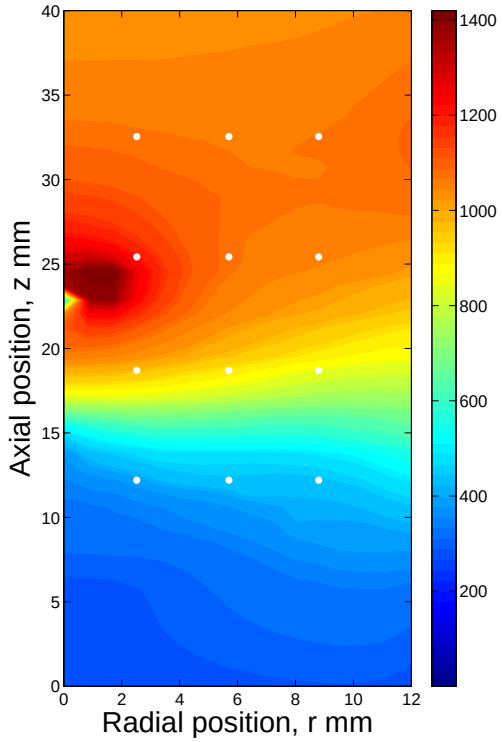

Figure 6.20: Mean temperature contour plot of case A, at t=13.5ms. Marked positions are used to show conditional averages in Figs. 6.21, 6.22 and 6.23.

case B there is a lower increase in temperature.

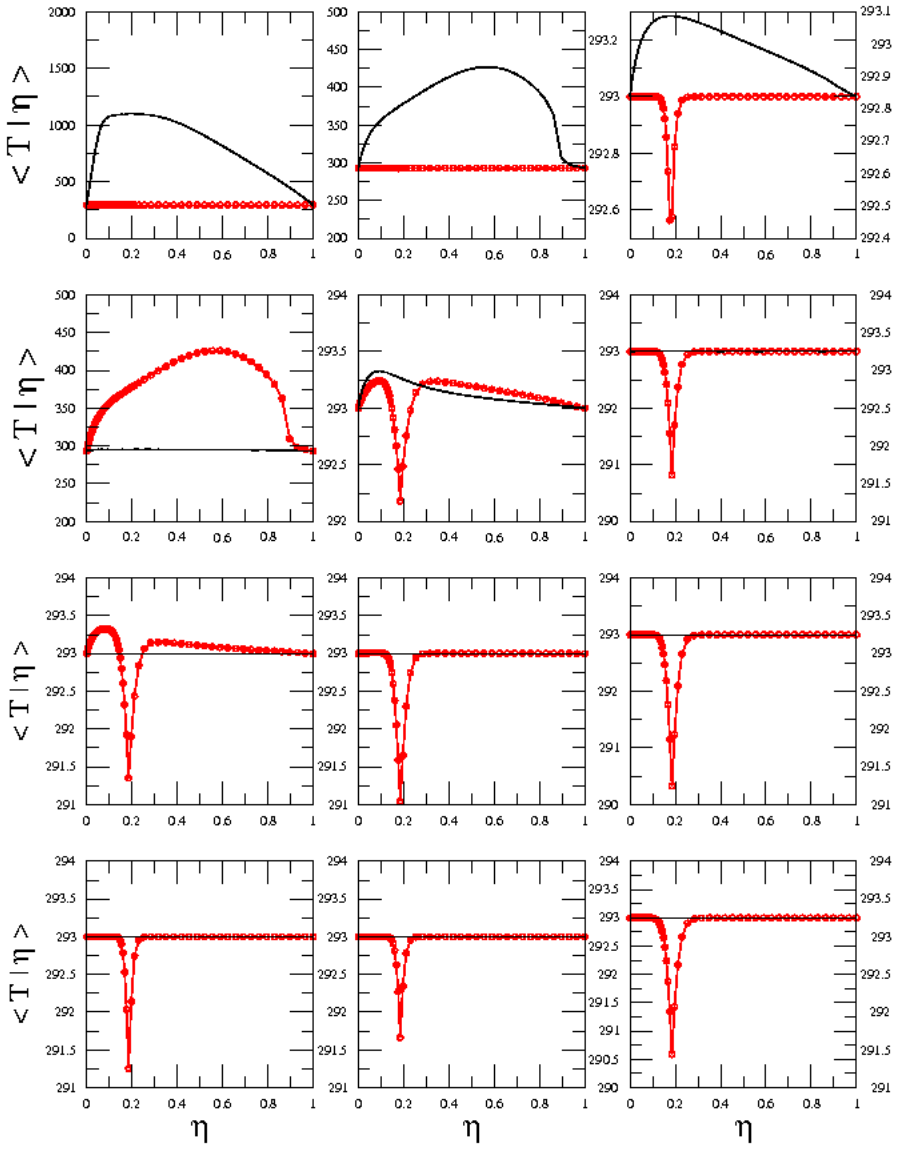

Figure 6.21: $\langle T|\eta\rangle$ for case A (red dotted) and B (black) at different locations for $t = 0.238ms$.

Figure 6.24 and 6.25 show the conditional oxygen mass fraction $\langle Y_{O_2}|\eta\rangle$ at the same locations in the burner as shown in Figure 6.20.

In Figure 6.24, a higher consumption of oxygen around the stoichiometric value of heptane can be seen for case B near the location of the initial spark kernel ($r = 0$mm,

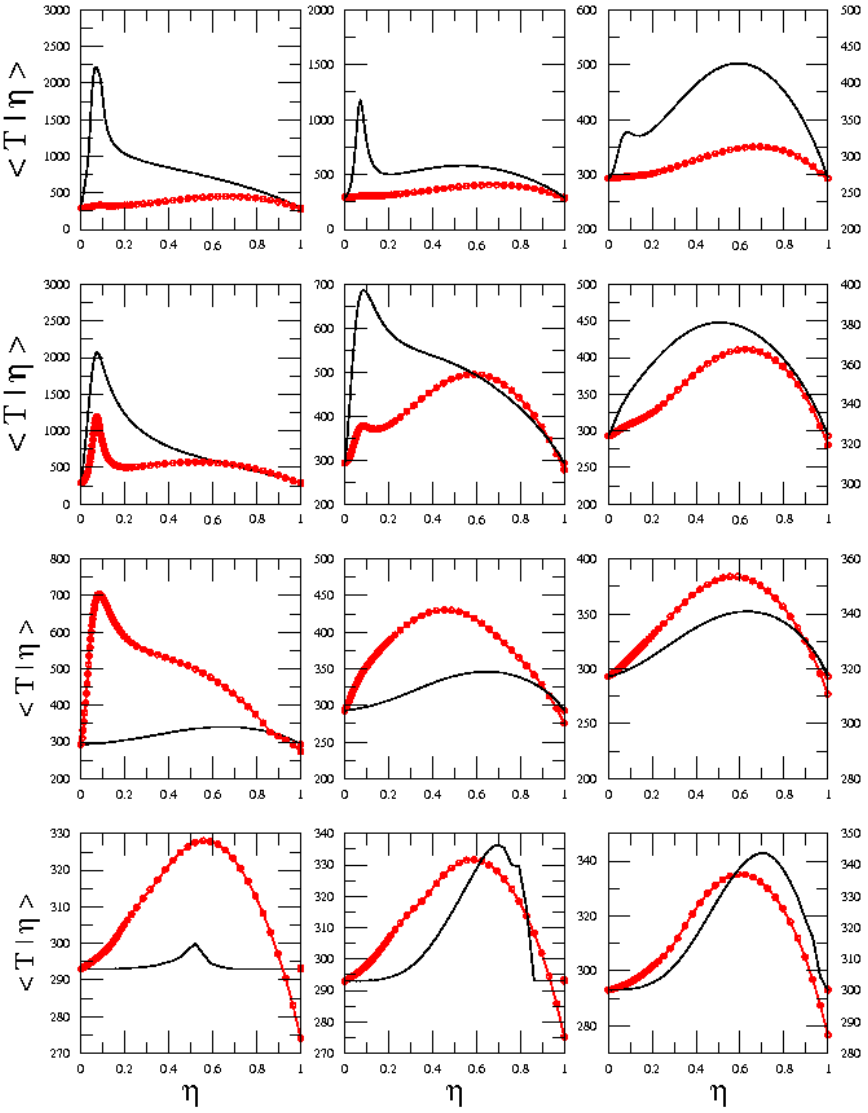

Figure 6.22: $\langle T|\eta\rangle$ for case A (red dotted) and B (black) at different locations for $t = 7.4ms$.

$z = 23$mm), indicating higher reaction rates compared to case A. Near to the bluff body slightly more oxygen is consumed in case A. At $t = 13.8$ms in the locations near to the initial spark kernel the profile of $\langle Y_{O_2}|\eta\rangle$ for case A gets similar to case B. Near to the bluff body there is still no significant reaction taking place for case B, keeping the level of oxygen available high over mixture fraction space.

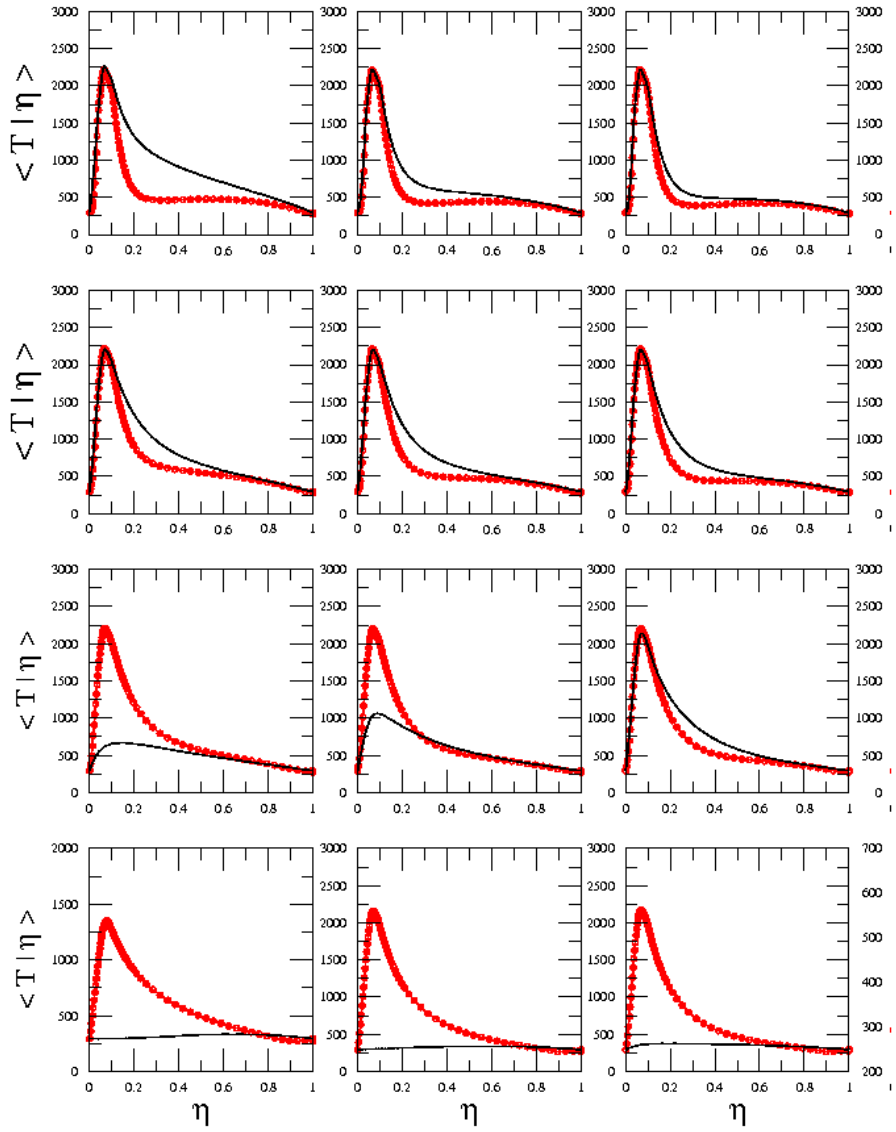

Figure 6.23: $\langle T|\eta\rangle$ for case A (red dotted) and B (black) at different locations for $t = 13.8ms$.

In case C and D the initial spark ignition kernel is placed at $r = 15$mm and 31.5mm, placed on the border of the inner recirculation zone in a region of gas phase mixture fraction values near the stoichiometry for heptane. Contour plots of Favre averaged temperature at different time steps after spark ignition for case C are shown in Figure 6.26. The white line denotes stoichiometric line of heptane.

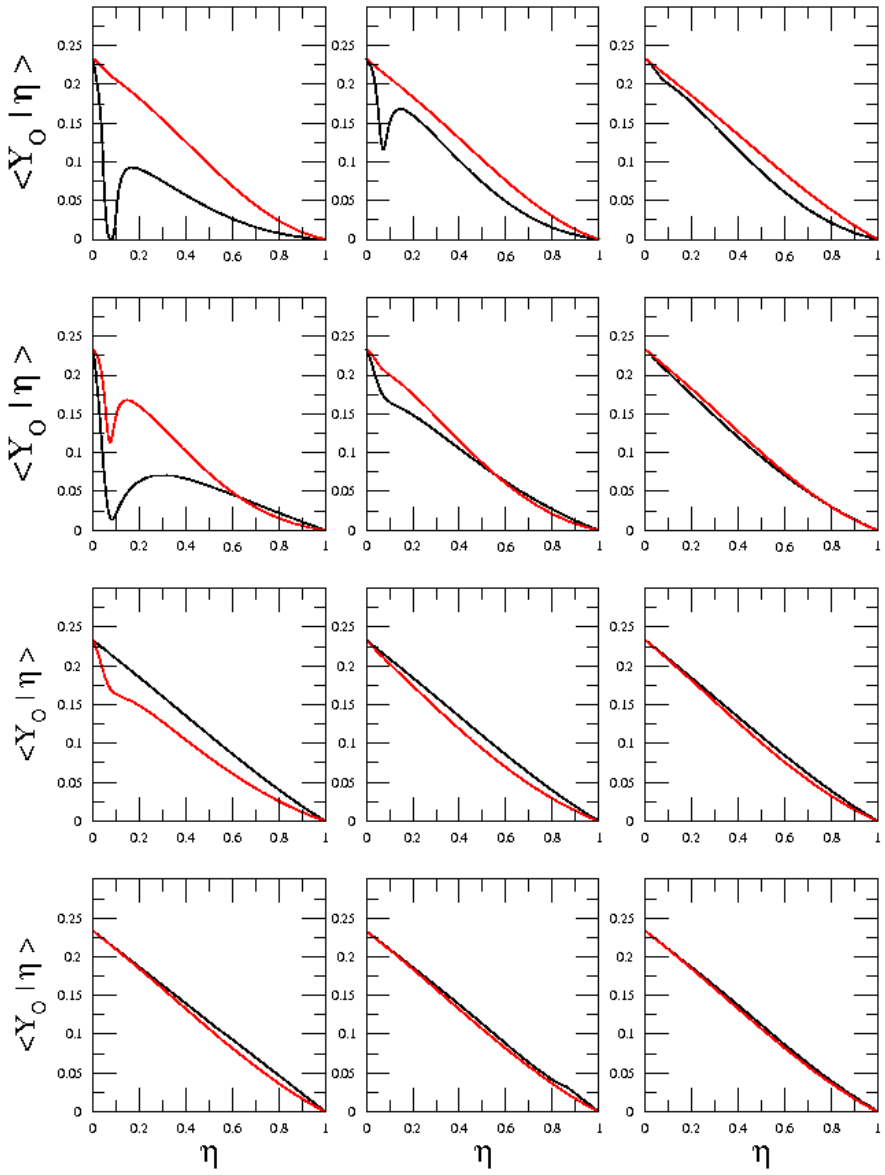

Figure 6.24: $\langle Y_{O_2}|\eta\rangle$ for case A (red dotted) and B (black) at different locations for $t = 7.4ms$.

The flame begins to expand along the isoline for ξ_{st} in the radial direction and then expands (after $t \approx 2ms$) fast into the overall lean downstream region. The flame expansion upstream into the fuel rich region is much slower and the flame stabilizes on

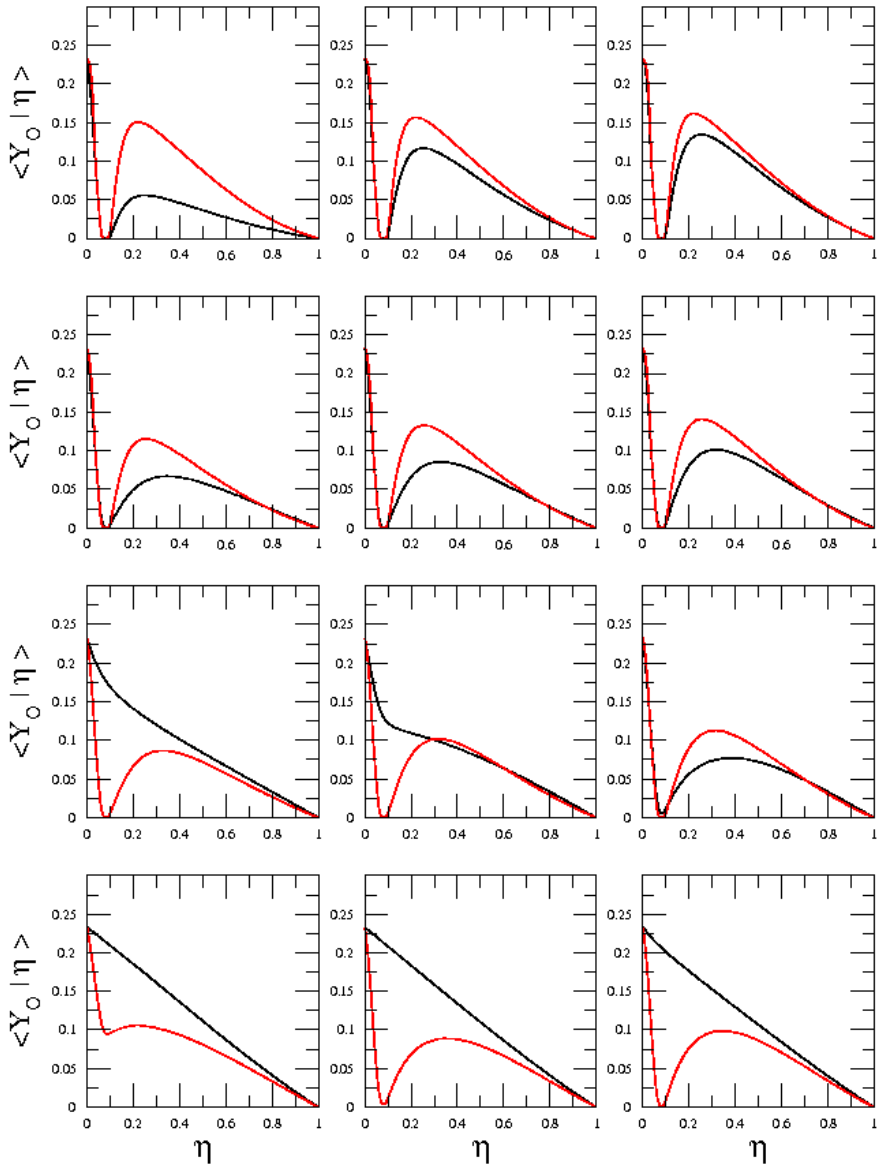

Figure 6.25: $\langle Y_{O_2}|\eta\rangle$ for case A (red dotted) and B (black) at different locations for $t = 13.8ms$.

the bluff body ($z = 0$mm) after approx. $t = 20$ms. The same contour plots for case D are not shown here since the resulting difference between case C and B is not clearly visible in the Favre averaged temperature contour plots.

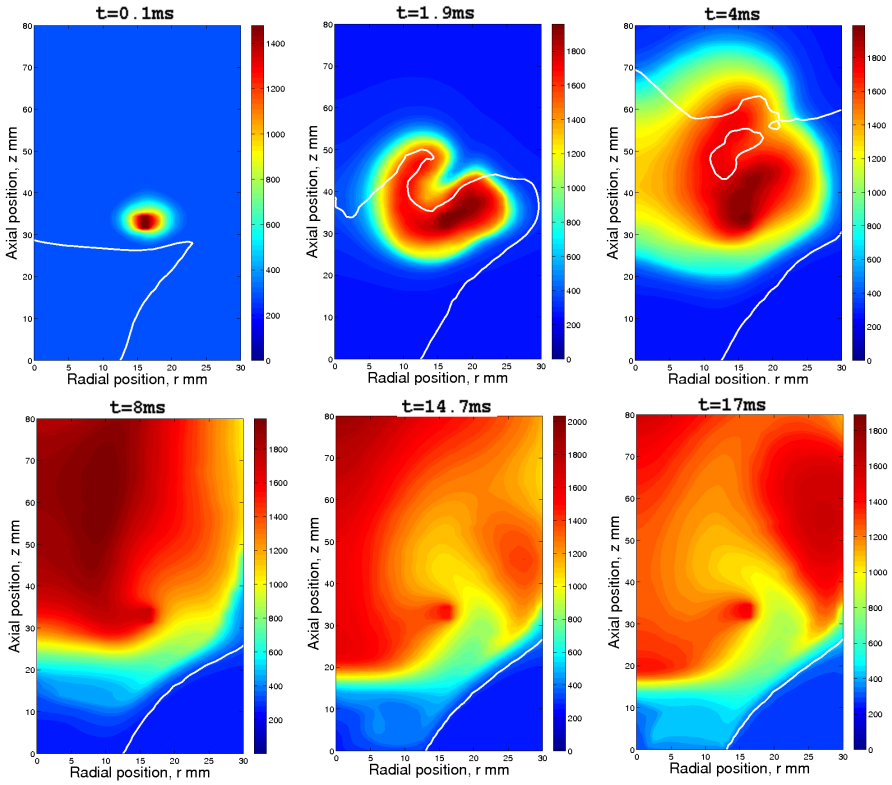

Figure 6.26: Contour plots of temperature for case C. The white line in the mean mixture fraction contour plot denotes the stoichiometric line for heptane.

To visualize the difference in temperature and mixture fraction distribution, Figure 6.27 shows contour plots of the temperature difference ΔT be together with $\Delta\widetilde{\xi}$, the difference of the mean mixture fraction between case C and D. Contour plots are taken at five different time steps after spark ignition. For the ΔT contour plots the cooling impact of the spray can be clearly seen near the bluff body to the axial center resulting in $5 - 10$K lower solution for case D. This causes a lower evaporation rate and hence results in a lower value of mixture fraction for case D near the core spray. In the proximity of the spark kernel the region towards higher mixture fraction shows a temperature increase of case D compared to case C while on the downstream side of the spark kernel regions of lower temperature for case D can be seen. During the concentric expansion of the flame kernel case D shows a lower temperature field in the flame front showing the cooling effect of the extra droplet source terms in the conditional temperature equation. This leads to a slight retardation of the flame growth of

case D compared to case C. The difference in the mean mixture fraction field between both cases seems to be of a random nature at later time steps after ignition in the spark kernel region.

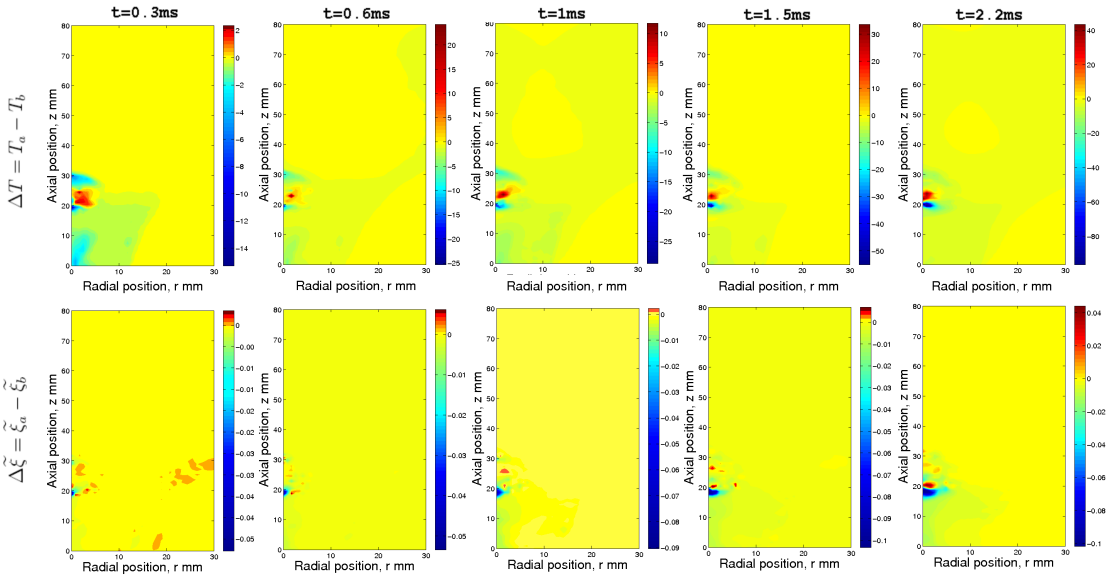

Figure 6.27: Above: Contour plots of temperature difference ΔT between case C (T_a) with and case D (T_b) without extra droplet source terms in the CMC equations. Below: Contour plots of mean mixture fraction difference $\Delta\widetilde{\xi}$ between case C ($\widetilde{\xi}_a$) with and case D ($\widetilde{\xi}_b$) without extra droplet source terms in the CMC equations.

To get a better insight into the effect of the additional droplet source terms in case D, Figure 6.28 shows the conditional temperature $\langle T|\eta\rangle$ for case C and D at different times at two locations near the fuel spray. At both locations at the early stages the impact of the spray in case D can be clearly seen. There is a cooling effect in $\langle T|\eta\rangle$ profile around $\xi = 0.19$, which is the saturation mixture fraction ξ_S for this location at this moment. At later time steps both case C and D have the same $\langle T|\eta\rangle$ profiles. Figure 6.29 shows two other locations downstream of the initial flame kernel where far less droplets are available compared to the locations in Fig. 6.28. Since for the location on the left hand side of Figure 6.29 all droplets are evaporated after a short time the $\langle T|\eta\rangle$ profiles for both cases approximate each other fast.

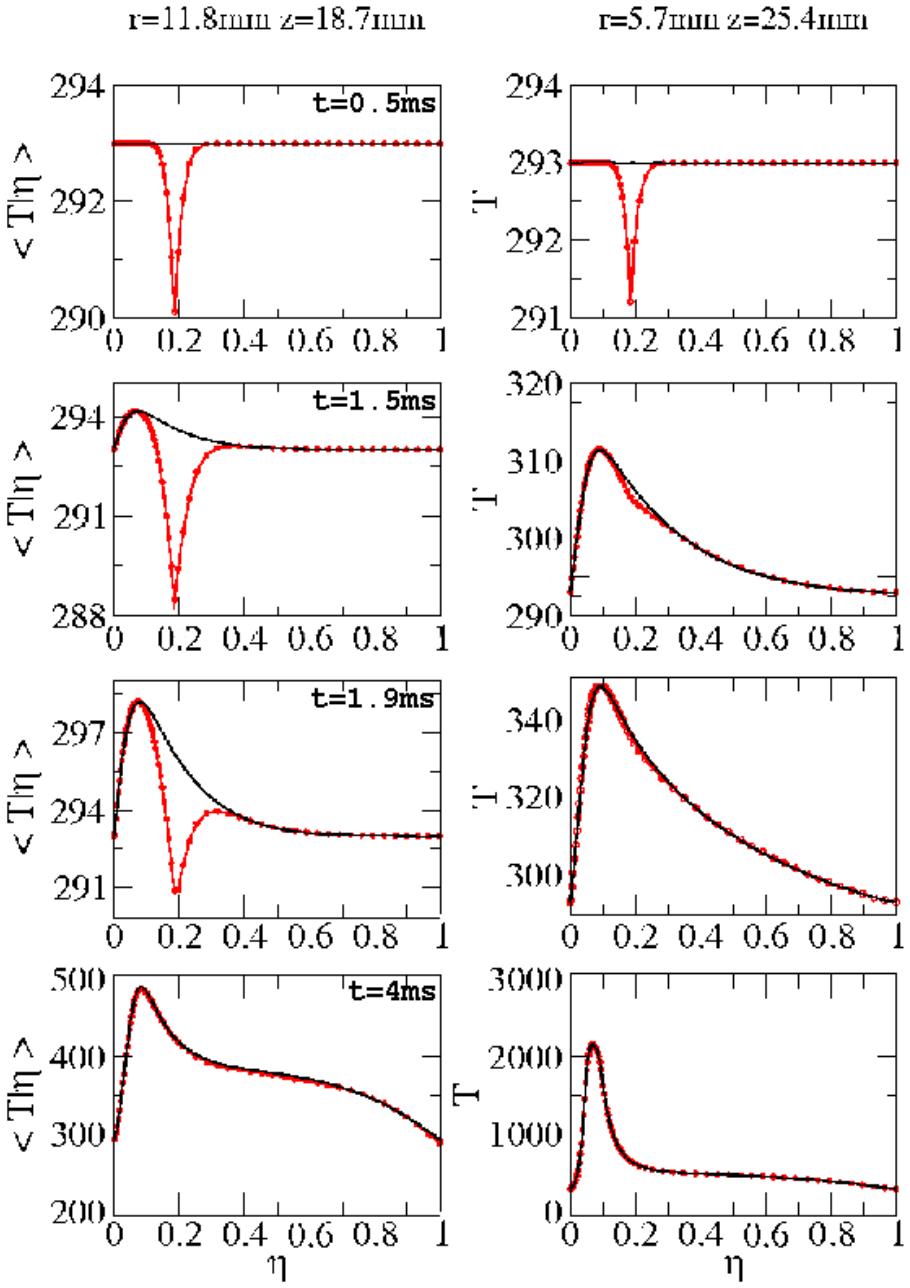

Figure 6.28: $\langle T|\eta\rangle$ for case C(red dotted) and D (black) at two different locations near the core spray for four different times after spark ignition. Location 1 is at $r = 11.8mm$ and $z = 18.7m$, location 2 at $r = 5.7mm$ and $z = 25.4mm$.

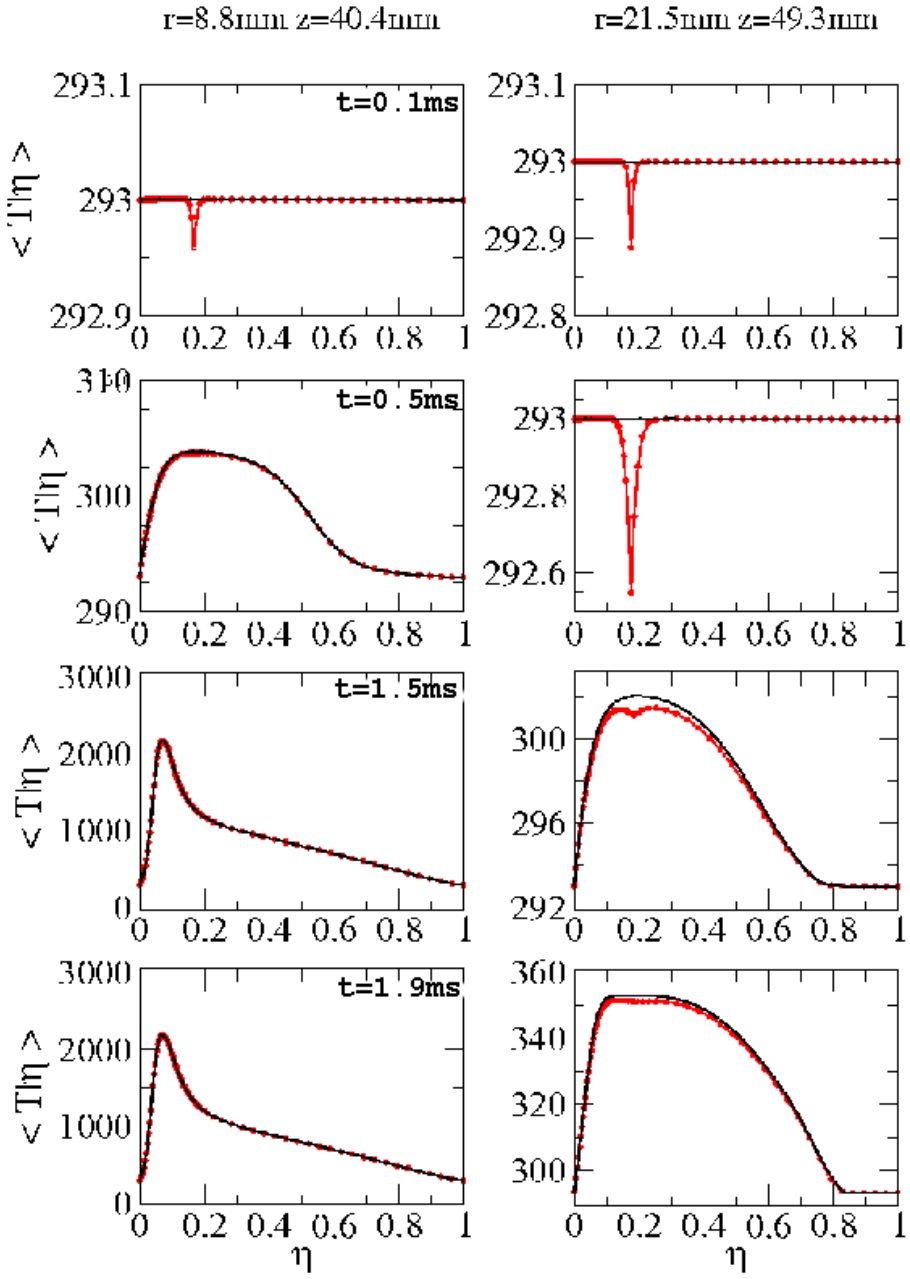

Figure 6.29: $\langle T|\eta\rangle$ for case C(red dotted) and D (black) at two different locations near the core spray for four different times after spark ignition. Location 3 is at $r = 8.8mm$ and $z = 40.4m$, location 4 at $r = 21.5mm$ and $z = 49.3mm$.

6.5 Conclusions

Two-dimensional Conditional Moment Closure has been applied to study a turbulent swirling n-heptane spray flame. The flow field has been solved using the commercial code STAR-CD. Conditional Moment Closure with and without equation extension to account for droplet evaporation has been compared and analyzed. Two different locations of the spark ignition in the flow field were chosen for the simulations. Comparison of mean axial and radial flow velocity, Sauter Mean Diameter distribution and a qualitative comparison of flame expansion after spark ignition between simulation and experiment showed that the CMC model works well for this problem. Comparison of contour plots, during the flame expansion after spark ignition, of mean temperature and mean mixture fraction for both CMC setups at both spark ignition locations showed minimal differences. A very small time retardation of the flame expansion for both cases with the extended CMC model can be seen. The comparison of $\langle T|\eta\rangle$ profiles shows the cooling effect of the droplet evaporation around ξ_S, in the extended CMC model, as expected.

Chapter 7

Conclusions

In this thesis a Conditional Moment Closure (CMC) model has been established which is extended to two-phase flow problems. Therefore three-dimensional DNS of autoignition in turbulent two-phase flows has been carried out to investigate in detail the interactions between droplet evaporation, mixing and autoignition. This DNS data was used for validation purposes of the proposed CMC model extended to two phase flows. To concentrate better on the validation of the extra droplet source terms, a spatially homogeneous CMC problem was taken which reduced the complexity of the governing CMC equations. The extended CMC model has then been interfaced with a commercial RANS two-phase flow solver to study the ignition process of an n-heptane spray flame in a flow typical of a liquid-fueled burner. The aim was to investigate the influence of the additional source terms due to the droplet evaporation process in the conditional species and energy equation. Results concerning each topic are presented below.

7.1 Direct Numerical Simulations of Autoignition in Turbulent Two-phase Flows

The simulations carried out in Chapter 4 demonstrate in the first part the impact of droplet evaporation on autoignition of n-heptane fuel droplets in hot ambient air incorporating three-dimensional isotropic decaying turbulence. In the second part the impact of droplet evaporation of n-heptane fuel droplets in a slab layer of saturated

fuel-gas vapor surrounded by hot ambient air is demonstrated.

It was found that autoignition is delayed when increasing the initial droplet size, possibly related to the higher conditional scalar dissipation rates in areas with droplet evaporation when the droplets are large and to the slower generation of fuel vapour. In addition it was found that the highest reaction rates originate at locations where the mixture fraction is around the most reactive mixture fraction, whose value was independent from the droplet size and which can be determined independently from a series of homogeneous calculations. Autoignition locations are also associated with low scalar dissipation rate. However, the correlation between scalar dissipation rates and reaction rates around the most reactive mixture fraction is weaker than for purely gaseous autoignition.

Finally it should be mentioned that extra care is needed when discussing the mixture fraction PDF and the conditional evaporation rate due to the fact that the steep gradients in the proximity of the droplet surface are not resolved and hence the resolved (i.e. cell) mixture fraction is not related to the value at which evaporation occurs.

7.2 Autoignition of spray flow using 0D-CMC

The predictions of 0D CMC simulations for autoignition times compared to DNS are in good agreement. Very good agreement can be seen prior to the occurrence of high reactions while the difference between 0D CMC and DNS later on can be due to the scalar dissipation model which overpredicts $\langle N|\eta\rangle$ when reaction takes place. Since the cooling effect of the droplets in the gas temperature field can be seen in the beginning where the scalar dissipation model is valid, the good agreement between 0D CMC and DNS shows that the CMC equations and closure assumptions presented in 3 are representing the physics of droplet evaporation well.

7.3 Simulations of spark ignition of a swirling spray flame with CMC

Conditional Moment Closure (CMC) extended to two-phase flows and interfaced with a commercial RANS two-phase flow solver has been used to study the ignition process of an n-heptane spray flame in a flow typical of a liquid-fueled burner. The aim was to investigate the influence of the additional source terms due to the droplet evaporation process in the conditional species and energy equation. The droplet source terms in the mean and variance of the mixture fraction equation are also modelled. For comparison, simulations without droplet source terms in the CMC equations were also carried out.

The CMC model works well for the flame expansion following spark ignition in a turbulent swirling recirculating n-heptane spray flame, suggesting that the model is capable of handling ignition events in realistic gas turbine combustors. The extra droplet source terms in the conditional mass fraction and temperature equations cause some differences in the simulations.

The air velocity field and droplet size are compared with experimental data and good agreement is found. The flame expansion process following ignition is compared qualitatively with fast-camera images from the experiment and the overall flame shape and speed are captured satisfactorily. The comparison between the normal and the extended CMC model shows only minimal differences in the temperature and mixture fraction contour plots. The cooling effect of evaporation terms in the extended CMC model are visible around ξ_S in the $\langle T|\eta\rangle$ profiles.

7.4 Future work

For simulations of Diesel engines an enhanced droplet evaporation model is needed in the current CMC model for spray combustion. Since the model presented here is based on the Clausius-Clayperon model for evaporation it is unsuitable for high pressures normally observed in simulations of Diesel engines. As well it would be of interest

to investigate the use of different droplet evaporation models in the CMC model, like models which relax the point source assumptions for droplets as made in the droplet evaporation model used in this thesis.

The CMC model for spray combustion, presented in this thesis, gives an useful tool to deal with challenges occuring in spray combustion and can be used as a starting point for future work. As well the effect of using different turbulence models should be investigated, like the Reynolds Stress model (RSM). To evaluate and increase confidence in using the here described CMC model for spray combustion more experimental is needed to have sufficient data for validation. An interesting area of future research for this CMC model is the full coupling with a LES solver. For purely gaseous flows, the CMC model has been incorporated with LES recently and shown promising results [39; 40].

Bibliography

[1] H. H. Chiu, H. Y. Kim, E. J. Croke, *Proc. Combust. Inst.* 19 (1982) 971–980. x, 16, 17, 18

[2] S. R. Turns, *An introduction to combustion: Concepts and applications*, McGraw-Hill, 2000. x, 6, 7, 8, 19, 26, 82

[3] P. Schroll, A. P. Wandel, R. S. Cant, E. Mastorakos, *Proc. Combust. Inst.* 32 (2009) 2275–2282. x, xi, 58, 59, 60, 62, 63, 64, 82

[4] T. Marchione, S. F. Ahmed, E. Mastorakos, *Combust. Flame* 156 (2009) 166 – 180. xiii, xiv, 4, 94, 96, 102, 105, 107

[5] E. Fernandez-Tarrazo, A. Sanchez, A. Linan, F. A. Williams, *Combust. Flame* 147 (2006) 32 – 38. xiii, 99, 100

[6] N. Peters, *Turbulent Combustion*, Cambridge University Press, 2000. 1, 8, 13, 34

[7] R. W. Bilger, S. B. Pope, K. N. C. Bray, J. F. Driscoll, *Proc. Combust. Inst.* 30 (2005) 21–42. 2

[8] J. Warnatz, U. Maas, R. W. Dibble, *Combustion*, Springer-Verlag Berlin Heidelberg, 2001. 2

[9] E. S. Richardson, *Ignition Modelling for Turbulent Non-Premixed Flows*, Phd thesis, University of Cambridge (2007). 2, 37, 39, 99

[10] R. Bilger, *Physics of Fluids* 5 (1993) 436–444. 3, 10, 15, 33, 39, 41

[11] F. X. Demoulin, R. Borghi, *Combust. Sci. Technol.* 158 (2000) 249–271. 3, 33, 39, 46, 48, 53, 67

[12] E. Mastorakos, T. A. Baritaud, T. J. Poinsot, *Combust. Flame* 109 (1997) 198–223. 4, 51, 52, 55, 58, 59, 61, 64

[13] D. Veynante, L. Vervisch, *Prog. Energy Combust. Sci.* 28 (2002) 193–266. 6

[14] T. Poinsot, D. Veynante, *Theoretical and Numerical Combustion*, Edwards, 2001. 6, 11, 12

[15] S. B. Pope, *Turbulent flows*, Cambridge University Press, 2000. 6, 13, 15, 34

[16] K. K. Kuo, *Principles of Combustion*, John Wiley and Sons, 1986. 9, 30

[17] S. Sreedhara, K. Y. Huh, *Proc. Combust. Inst.* 31 (2007) 2335–2342. 9, 11, 39, 52, 53, 61, 64, 66, 82

[18] R. Hilbert, D. Thevenin, *Combust. Flame* 128 (2002) 22–37. 11, 52

[19] T. Echekki, J. H. Chen, *Combust. Flame* 134 (2003) 169–191. 11, 52

[20] R. Hilbert, D. Thevenin, *Combust. Flame* 138 (2004) 175–187. 11

[21] J. H. Chen, E. R. Hawkes, R. Samkaran, S. D. Mason, H. G. Im, *Combust. Flame* 145 (2006) 128–144. 11

[22] S. Sreedhara, K. Lakshmisha, *Proc. Combust. Inst.* 28 (2000) 25–33. 11

[23] S. Sreedhara, K. Lakshmisha, *Proc. Combust. Inst.* 29 (2002) 2051–2059. 11, 52, 58

[24] P. Domingo, L. Vervisch, *Combust. Flame* 140 (2005) 172–195. 11, 30, 31

[25] N. Charkraborty, E. Mastorakos, R. S. Cant, *Combust. Sci. Tech.* 179 (2007) 293–317. 11, 53

[26] P. Domingo, L. Vervisch, *Proc. Combust. Inst.* 31 (2007) 1657–1664. 11

[27] S. Cao, T. Echekki, *Combust. and Flame* 151 (2007) 120–141. 11

[28] F. Mashayek, *Int. J. Heat Mass Trans.* 41 (1998) 2601–2617. 11

[29] R. S. Miller, J. Bellan, *J. Fluid Mech* 384 (1999) 293–338. 11, 32

[30] J. Réveillon, L. Vervisch, *Combust. Flame* 121 (2000) 75–90. 11, 39, 46, 52, 53, 66, 82

[31] O. Colin, A. Benkenida, *Combust. Flame* 134 (2003) 207–227. 11

[32] L. Selle, J. Bellan, *Proc. Combust. Inst.* 31 (2007) 2273–2281. 11

[33] F. Mashayek, *Int. J. Heat Mass Trans.* 44 (2001) 1517–1526. 11

[34] F. Mashayek, *Int. J. Heat Mass Trans.* 44 (2001) 1527–1541. 11

[35] Y. Wang, C. J. Rutland, *Proc. Combust. Inst.* 30 (2005) 893–900. 11, 52, 53

[36] Y. Wang, C. J. Rutland, *Combust. Flame* 149 (2007) 353–365. 11, 52, 53

[37] J. Smagorinsky, *Monthly Weather Review* 9 (1963) 99–164. 13

[38] S. Navarro-Martinez, A. Kronenburg, *Proc. Combust. Inst.* 31 (2007) 1721–1728. 13

[39] S. Navarro-Martinez, A. Kronenburg, *Proc. Combust. Inst.* 32 (2009) 1509–1516. 13, 129

[40] A. Triantafyllidis, E. Mastorakos, R. Eggels, *Combust. Flame* 156 (2009) 2328–2345. 13, 129

[41] S. P. Burke, T. E. W. Schumann, *Industrial and Engineering Chemistry* 20 (1928) 998–1003. 14

[42] W. R. Hawthorne, D. S. Weddell, H. C. Hottel, *Proc. Combust. Inst.* 3 (1948) 266–288. 14

[43] B. F. Magnussen, B. H. Hjertager, *Proc. Combust. Inst.* 16 (1977) 719–727. 14

[44] R. S. Cant, E. Mastorakos, *An introduction to turbulent reacting flows*, Imperial College Press, 2008. 14

[45] N. Peters, *Combust. Sci. Tech.* 30 (1983) 1–17. 14

[46] S. K. Lieu, K. N. C. Bray, J. B. Moss, *Combust. Sci. Tech.* 27 (1981) 69–83. 14

[47] V. Favier, L. Vervisch, *Combust. Flame* 125 (2001) 788–803. 14

[48] E. Mastorakos, *Prog. Energ. Combust. Sci.* 35 (2009) 5797. 14, 52

[49] V. A. Frost, *Fluid Mechanics, Soviet Research* 4 (1975) 124–133. 15

[50] P. A. Libby, F. A. Williams, *Turbulent Reacting Flows*, Academic Press New York, 1994. 15

[51] *Sandia National Laboratories, TNF Workshop website. Available from http://www.ca.sandia.gov/TNF* (1994). 15

[52] R. W. Bilger, L. V. Krishnamoorthy, L. R. Saetran, *J. Fluid Mech* (1991) 211–244. 15

[53] A. Y. Klimenko, *Fluid Dynamics* 25 (1990) 327–334. 15

[54] A. Y. Klimenko, R. W. Bilger, *Prog. Energ. Combust. Sci.* 25 (1999) 595–687. 15, 33, 34, 37, 38, 39, 42, 45

[55] S. H. Kim, K. Y. Huh, L. Tao, *Combust. Flame* 120 (2000) 75–90. 15

[56] S. H. Kim, K. Y. Huh, *Proc. Combust. Inst.* 29 (2002) 273–279. 15, 39

[57] A. Kronenburg, R. W. Bilger, J. H. Kent, *Proc. Combust. Inst.* 27 (1998) 1097–1104. 15

[58] I. S. Kim, E. Mastorakos, *Proc. Combust. Inst.* 30 (2005) 911 – 918. 15

[59] M. R. Roomina, R. W. Bilger, *Combust. Flame* 125 (2001) 1176 – 1195. 15

[60] D. B. Spalding, *4th Symp. (Intl.) on Combustion* (1953) 847–864. 16

[61] A. Williams, *Combust. Flame* 21 (1973) 1–31. 16

[62] G. M. Faeth, *Prog. Energy Combust. Sci.* 3 (1977) 191–224. 16, 25, 29

[63] C. K. Law, *Prog. Energy Combust. Sci.* 8 (1982) 171–201. 16, 18, 29

[64] B. Abramzon, W. A. Sirigano, *Int. J. Heat Mass Trans.* 32 (9) (1989) 1605–1618. 19

[65] W. A. Sirigano, *Fluid dynamics and transport of droplets and spray*, Cambridge University Press, Cambridge UK, 1999. 29, 30, 82

[66] C. T. Crowe, M. Sommerfeld, Y. Tsuji, *Multiphase flows with droplets and particles*, CRC Press, Boca Raton FL, 1998. 30

[67] S. K. Aggarawal, A. Y. Tong, W. A. Sirignano, *AIAA Journal* 22 (1984) 1448–1457. 32

[68] R. Miller, K. Harstad, J. Bellan, *Int. J. Multiphase Flow* 24 (1998) 293–338. 32

[69] M. Nakamura, F. Akamatsu, R. Kurose, M. Katsuki, *Phys. Fluids* 17 (2005) 1–14. 32

[70] A. Y. Klimenko, R. W. Bilger, *Prog. Energ. Combust. Sci.* 25 (1999) 595–687. 36, 37

[71] E. Mastorakos, R. W. Bilger, *Physics of Fluids* 10 (1998) 1246–1248. 38

[72] A. Kronenburg, *Physics of Fluids* 16 (2004) 2640. 38

[73] E. E. Brien, T. L. Jiang, *Physics of Fluids* 3 (1991) 3121–3123. 38

[74] Y. M. Wright, G. de Paola, K. Boulouchos, E. Mastorakos, *Combust. Flame* 143 (2005) 402–419. 39, 53

[75] N. S. A. Smith, C. M. Cha, H. Pitsch, J. C. Oefelein, in: *Proc. Summer Prog.*, 2000, pp. 207–218. 39, 66, 82

[76] J. W. Rogerson, J. H. Kent, R. W. Bilger, *Proc. Combust. Inst.* 31 (2007) 2805–2811. 39, 40, 41, 46

[77] C. Hollmann, E. Gutheil, *Proc. Combust. Inst.* 26 (1996) 1731–1738. 39, 53

[78] M. Mortensen, R. W. Bilger, *Combust. Flame* 156 (2009) 62–72. 41, 42, 48, 53, 66, 82

[79] G. de Paola, *Conditional moment closure for autoignition in turbulent flow*, Ph.D. thesis, University of Cambridge, UK (2007). 45, 53, 64

[80] T. Lundgren, *Physics of Fluids* 10 (1967) 969–975. 46

[81] F. X. Demoulin, R. Borghi, *Combust. Flame* 129 (2002) 281–293. 46, 48, 65

[82] A. H. Lefebvre, *Gas Turbine Combustion*, Taylor and Francis, 1998. 52, 95

[83] L. C. Selle, J. Bellan, *Proc. Combust. Inst.* 31 (2007) 2273–2281. 52, 64

[84] K. W. Jenkins, R. S. Cant, in: *Proc. of the 2nd AFOSR Conf. on DNS and LES*, Kluwer Academic Publishers, 1999. 53

[85] J. Réveillon, F. X. Demoulin, *Proc. Combust. Inst.* 31 (2007) 2319–2326. 61

[86] D. B. Spalding, *Combustion and Mass Transfer*, Pergamon Press, 1979. 95

[87] S. F. Ahmed, R. Balachandran, T. Marchione, E. Mastorakos, *Combust. Flame* 151 (2007) 366–385. 95, 96

[88] C. adapco Group, *STAR-CD v3.26* (2004). 97

[89] R. D. Reitz, R. Diwakar, *SAE950283*. 98

[90] P. N. Brown, G. D. Byrne, A. C. Hindmarsh, *SIAM J. Sci. Statist. Comput.* 10 (1989) 1038 – 1051. 99

[91] P. N. Brown, A. C. Hindmarsh, *J. Appl. Math. Comput.* 31 (1989) 49 – 91. 99